Forschungszentrum Jülich
in der Helmholtz-Gemeinschaft

Institut für Energieforschung (IEF)
Plasmaphysik (IEF-4)

Modeling of Plasma Response to Magnetic Field Perturbations from the Dynamic Ergodic Divertor (DED) and Comparison with Experiment

Xavier Loozen

Jül-4251

Modeling of Plasma Response to Magnetic Field Perturbations from the Dynamic Ergodic Divertor (DED) and Comparison with Experiment

Xavier Loozen

Berichte des Forschungszentrums Jülich ; 4251
ISSN 0944-2952
Institut für Energieforschung (IEF)
Plasmaphysik (IEF-4) Jül-4251
(Brüssel, Univ. Mons-Hainaut, Diss., 2006)

Vollständig frei verfügbar im Internet auf dem Jülicher Open Access Server (JUWEL)
unter http://www.fz-juelich.de/zb/juwel

Zu beziehen durch: Forschungszentrum Jülich GmbH · Zentralbibliothek, Verlag
D-52425 Jülich · Bundesrepublik Deutschland
☎ 02461/61-5220 · Telefax: 02461/61-6103 · e-mail: zb-publikation@fz-juelich.de

Kurzfassung

Seit Jahrzehnten wird versucht, eine kontrollierte Fusion von Deuterium- und Tritiumkernen im Labor zu erreichen, mit dem Ziel, eine fast unerschöpfliche Energiequelle nutzbar zu machen. Die vorliegende Arbeit befasst sich mit dem sogenannten Tokamak, einer torusförmigen Anlage in der das Fusionsplasma durch ein Magnetfeld eingeschlossen wird, welches durch geeignet angeordnete Spulen und im Plasma induzierte Ströme erzeugt wird. Dieses Magnetfeld beschränkt die Bewegung der geladenen Teilchen auf die Superposition einer Bewegung entlang der Magnetfeldlinien, und einer Rotation senkrecht zu diesen. Der Gyrationssradius der Teilchen ist üblicherweise sehr klein im Vergleich zur den Abmessungen des Tokamakgefäßes.

Durch verschiedene Prozesse wird die ideale Gyrationsbewegung der Teilchen gestört und die ins Plasma deponierten Teilchen und die Wärmeenergie gehen durch Transport zu den Wänden des Tokamaks verloren. Es gibt eine breite Palette von Mechanismen, die den Transport zu den Wänden verursachen. Am besten verstanden ist die neoklassische Diffusion, die durch Stöße zwischen geladenen Teilchen zustande kommt. Experimentelle Beobachtungen zeigen jedoch, dass der Transport weitaus grösser ist als von der Theorie der neoklassischen Diffusion vorhergesagt. Es wird allgemein angenommen, dass weitere Transportprozesse existieren, die durch verschiedene Plasmainstabilitäten hervorgerufen werden und den sogenannten anomalen Transport verursachen. Eine Kontrolle der Teilchen- und Wärmeflüsse, die infolge dieses anomalen Transportes auftreten, ist von größter Bedeutung für zukünftige Fusionsreaktoren, damit die für die Kernfusion notwendigen hohen Dichten und Temperaturen gewährleistet werden können. Mit dieser Absicht hat man die Ergodischen Divertoren (ED) als ein Mittel für die Kontrolle des Transports in der Plasmarandschicht vorgeschlagen. Durch zusätzliche Spulen bringen solche Vorrichtungen eine schwache Störung in das Magnetfeld des Tokamaks ein. Dadurch werden Feldlinien in radiale Richtung, senkrecht zu den ungestörten magnetischen Oberflächen, abgelenkt und der radiale Transport durch Transport entlang solcher Feldlinien geändert. Die Bezeichnung ergodisch rührt daher, dass solche Störungen zu chaotischem oder stochastis-

chem Verhalten der Feldlinien führen.

In dieser Arbeit wird ein Modell [60] für den Transport im stochastischen Magnetfeld weiter entwickelt und zur Modellierung der Plasmadynamik in den Tokamaks Tore Supra (Cadarache, Frankreich) und TEXTOR (Jülich, Deutschland) mit Ergodischen Divertoren angewandt. Dieses Modell basiert auf der Annahme, dass der Transport des Plasmas hauptsächlich entlang optimalen Pfaden stattfindet, welche aus einer Folge von Segmenten parallel und senkrecht zu den Feldlinien bestehen. Als Ergebnis werden die effektiven radialen Transportkoeffizienten als Funktionen der Charakteristiken des stochastischen Feldes und des Transports parallel und senkrecht zu den Feldlinien berechnet. Das Modell für den senkrechten Transport wird dabei unter Bercksichtigung verschiedener relevanter Instabilitäten in der Plasmarandschicht ausgearbeitet. Diese Transportmodelle werden im Vergleich mit Temperatur- und Dichteprofilmessungen in Tore Supra validiert und in den 1.5-dimensionalen Transportcode RITM eingefgt, um radiale Profile von verschiedenen Plasmaparametern selbstkonsistent zu berechnen. Mit diesem so erweiterten Code werden Simulationsrechnungen für verschiedene experimentelle Bedingungen im Tokamak TEXTOR mit Dynamischem Ergodischen Divertor (DED) durchgeführt. Die RITM-Ergebnisse werden mit den Messungen der thermischen Energie mittels der diamagnetischen Spule verglichen. Schließlich werden die Profile der Plasmadichte und Temperatur, die für die Bedingungen ohne und mit DED im statischen Betrieb berechnet wurden, mit den Messungen verschiedener Plasmadiagnostiken verglichen.

Abstract

For several decades, physicists try to get under laboratory conditions fusion of deuterium and tritium nuclei, with the aim to provide a practically inexhaustible source of energy. The present work is focused onto tokamaks only, which are torus-shaped devices with the magnetic field produced by external coils and electric current in the plasma. This magnetic field restrains the particle motion to a translation along the field lines, and a gyration in a plane perpendicular to them, with a gyro-radius small compared to the size of the machine.

The control of particle and heat transport is a critical issue to obtain the high temperatures and densities required for fusion in future reactors. Collisions between particles lead to transport of both heat and charged particles towards the walls of the tokamak. This transport mechanism is well understood. However, the experimentally observed transport level is much higher than the expected one due to collisions and it is commonly believed that there are additional transport mechanisms. These mechanisms are referred to as anomalous transport and result from microscopic plasma instabilities of different types. Ergodic Divertors (ED) have been introduced in order to provide means to control the transport at the plasma edge. Such devices superpose a small magnetic perturbation from additional coils onto the main magnetic field. Without such perturbations, the magnetic field lines lie on nested toroidal magnetic surfaces. When a perturbation is applied, field lines exhibit small deviations in the direction perpendicular to the unperturbed magnetic surfaces. A sufficiently strong perturbation results in a chaotic behaviour of magnetic field lines, or magnetic field stochastization, allowing transport towards the walls along field lines.

In the present work, a model for transport in a stochastic magnetic field [61] is further developed and applied for modelling of plasma behaviour with EDs. This model implies that the transport towards the walls takes place predominantly along the so called 'optimal' paths. Such paths consist of a succession of segments aligned with the field lines, and segments perpendicular to them. This model provides effective transport coefficients in the

form of a function of the characteristics of the stochastic field and transport perpendicular and parallel to the field lines. A second part of the work consists in the development of a model for anomalous perpendicular transport coefficients, taking into account the most important edge instabilities. These two models, for anomalous transport and for its modification in a stochastic field, are then compared with experimental temperature and density profiles from the tokamak Tore Supra in Cadarache, France, operated with an ED. In the third part of the work both models are included into the 1.5-D transport code RITM ('.5' stems for the inclusion of the toroidal geometry), for self-consistent calculation of profiles for various plasma parameters. Simulations have been performed for the conditions of experiments on the tokamak TEXTOR in Jülich, Germany, where a Dynamic ED (DED) is presently in operation. In order to validate the RITM calculations, measurements of the diamagnetic energy with a diamagnetic loop have been performed. The results of simulations, without DED and with DED in a static mode, are compared with these experimental data as well as with the radial profiles of plasma parameters measured by other diagnostics.

Acknowledgments

I would like to express my thanks to my supervisor Dr. M. Tokar for permitting me to accomplish this work, for his advice and guidance, and in particular for his encouragements and his great availability for answering my questions.

I wish to acknowledge Dr. R. Koch for his carefull reading of this thesis.

I am grateful to Prof. R. Weynants for his help to find a Ph.D. position and his advice concerning the present work.

I thank Drs. G. Bertschinger and O. Zimmermann for their help concerning the experimental part of this work. I am also grateful to H. Jaegers who provided me technical assistance whenever I needed it, and to Drs. Van Wassenhove, Dumortier and Messiaen for their advice concerning diamagnetic measurements.

I greatly appreciated discussions with Dr. D. Reiser who much helped me to understand the basics of plasma fluid mechanics.

I would like to acknowledge Drs. M. Jakubowski, O. Schmitz and Y. Xu for fruitful discussions I had with them and for the data they provided me.

I also would like to thank the Ph.D. students and "Diplomanden" of the IPP-Jülich for the different activities, the fun and the discussions we had together. In particular, I wish to acknowledge A. Gupta with whom I appreciated to share an office, and Dr. O. Marchuk who was never tired of organizing activities and always ready to provide me help or accomodation. I keep a great memory of that day where O. Marchuk, K. Löwenbrück and F. Irrek joined me in the crazy project to cover the distance Jülich-Brussels in one day by bike.

I am thankful to my parents and my sister Florence who provided my encouragement and support during my stay in Germany, especially during the writing of my thesis.

I would like to address a very particular thank my sweetheart Murielle for her patience, her help and her love during the three years we lived far from each other. I also acknowledge her for using her talents in the 3D drawing of an island chain.

I also wish to thank the Forschungszentrum Jülich for allowing me to undertake my thesis in Jülich.

Finally, I address a general thank to all people who provided me help and whose list is too long to be mentioned here.

Contents

Chapter 1

Introduction

The problem of ever diminishing fossil energy resources, increasing energy demand, and pollution, mainly through emission of greenhouse gasses is known for tens of years. Thermonuclear fusion, i.e. production of energy by processes similar to what happens in the sun, the source of all the forms of energy used on earth[1], is one of the technical solutions investigated to cope with this problem. It is not surprising to know that research on thermonuclear fusion is lead for more than 50 years when one is aware of the challenge: to operate a machine with temperatures of the order of 100 million K, i.e. about 10 times the central temperature of the sun, and density in the range of $10^{20}m^{-3}$-$10^{21}m^{-3}$ (for introduction to the subject, see for example [67]). The main reaction will be

$$D^2 + T^3 \rightarrow He^4\ (3.5MeV) + n^1\ (14.1MeV), \tag{1.1}$$

other reactions like D^2+D^2 and D^2+He^3 having a much smaller cross section at temperatures around 100 million K. Two types of machines have been set up to explore the possibility of getting continuous fusion: stellarators and tokamaks. Stellarators have a very complex magnetic structure and will not be considered here (an introduction to stellarators can be found in [58]). Tokamaks, which are of concern here, are torus-shaped machines. In these machines, a strong toroidal magnetic field is produced by external coils, in order to confine the plasma.

To achieve the aforementioned conditions, control of heat and particle transport is an important issue. On the one hand, a low transport is attractive in order to achieve a high plasma confinement. On the other hand, a high impurity transport is desirable for plasma decontamination: He and impurities coming from erosion of plasma facing components radiate proportionally to Z^2, with Z their charge state. If they accumulate in the plasma,

[1] except for geothermal and nuclear fission energies

confinement will strongly be degraded by radiation. Many transport codes aim at explaining observed temperature and density profiles, and predicting those under given conditions. RITM, which is used in the present study, is one of these codes and is able to compute radial profiles for temperatures and densities of electrons, main ions and impurities.

Due to the magnetic configuration of tokamaks, the structure limiting the plasma volume, which can be a limiter or a divertor, is exposed to very strong heat loads (see for example [63]). With the purpose of reducing the temperature of the plasma in contact with the plasma facing components, and hence their erosion, Ergodic Divertors (ED) have been introduced. They consist of coils disposed around the plasma, in which currents flow in order to perturb the main toroidal magnetic field. If these currents are high enough, the magnetic field is ergodized, and the field lines follow stochastic trajectories, though keeping the toroidal direction as the main one. Besides spreading energy on the divertor plate, the ergodization of the magnetic field has benefits on transport: it enhances edge transport, which allows a reduction of impurity concentration. An increase of edge transport was indeed observed [14, 16, 21] in tokamaks equipped with an ED. However, unexpectedly, a layer with decreased transport was seen in a deeper region in some tokamaks when operating with an ED [45, 48]. On TEXTOR, a Dynamic ED (DED) [16] has been installed with the purpose of influencing transport parameters at the plasma edge and studying the resulting effects on heat exhaust, edge cooling, impurity screening, plasma confinement and stability. The rotation of the magnetic perturbation, which is a specific feature of the TEXTOR ED, aims at increasing the plasma velocity shear, which could have beneficial effects on transport.

The object of the present work is the study of plasma profile variations under operation with the DED. Static perturbations are considered in the following, effects of plasma rotation being out of the scope of this work. The effects of magnetic field stochastization are investigated by developing a model for transport in a stochastic magnetic field, in the line of reference [61]. Without perturbation, the magnetic configuration of a tokamak is such that the transport towards the walls, which leads to confinement losses, is due to transport perpendicular to the magnetic field lines only. It is generally described by the so-called anomalous perpendicular transport coefficients. When a perturbation is applied to this magnetic configuration, transport towards the walls involves transport along the field lines as well. According to the model of reference [61], transport towards the walls consists of an alternation of transport both perpendicular and parallel to the field lines. This modification of the anomalous transport is taken into consideration by defining effective transport coefficients for transport in the direction of the walls. These effective transport coefficients are in the form of the product of the anomalous perpendicular transport coefficients with a function taking transport along perturbed magnetic field lines into account and determined on the basis of the plasma characteristics.

This thesis is structured as follows: in chapter 2, after a general introduction to the magnetic topology of a tokamak, the effects of the DED on this topology are presented, and the model of reference [61] is explained and developed further. Since anomalous perpendicular transport coefficients are necessary for this model, a model for anomalous perpendicular transport is developed in chapter 3. This model can describe separately drift resistive, drift resistive ballooning and drift-Alfvèn instabilities, which are generally invoked as the dominant sources of turbulent transport near the edge. In order to perform self-consistent calculations of different plasma parameters, these models have been implemented into the code RITM, described in chapter 4. For the validation of the plasma profiles, measurements of the plasma energy content have been performed, see chapter 5. Results of computation of plasma profiles with RITM, without and with DED, and comparison with experimental results are then presented in chapter 6. Finally, a summary and perspectives for the continuation of the present work are given in chapter 7.

Chapter 2

Model for effective transport coefficients in a stochastic magnetic field

2.1 Magnetic geometry of a tokamak

In order to reach the temperature and density required for a commercially acceptable fusion reactor, a strong magnetic field is used to confine the plasma within a tokamak. In this field, charged particles experience a Lorentz force $\boldsymbol{F}_L = Q\,(\boldsymbol{v} \times \boldsymbol{B})$, with Q and $\boldsymbol{v}$ being the charge and velocity of the particle, and $\boldsymbol{B}$ the magnetic field. Therefore, the particle perpendicular motion is bent into a circle, and the total trajectory of a particle is a helix curled round the magnetic field lines.

In the present study, all considered phenomena have characteristic times much larger than the gyration period of particles around field lines. For that reason, the time averaged motion of a particle is approximated by the motion of its gyration center. In the simplest case, the motion of the gyration center is parallel to the magnetic field lines. However, in presence of external forces or inhomogeneities, gyration centers drift in a direction perpendicular to the force or to the gradient of the inhomogeneity. In particular, in a tokamak, the centrifugal force due to the bending of the field lines, and the force due to the *grad-B* inhomogeneity[1], both directed towards the outside of the tokamak,

[1]The *grad-B* force is due to the $1/R$ dependence of B, with R the distance to the center of the tokamak. This dependence can be found from the condition $\boldsymbol{\nabla} \times \boldsymbol{B} = 0$ in the plasma chamber, with the assumption that the plasma current is negligible.

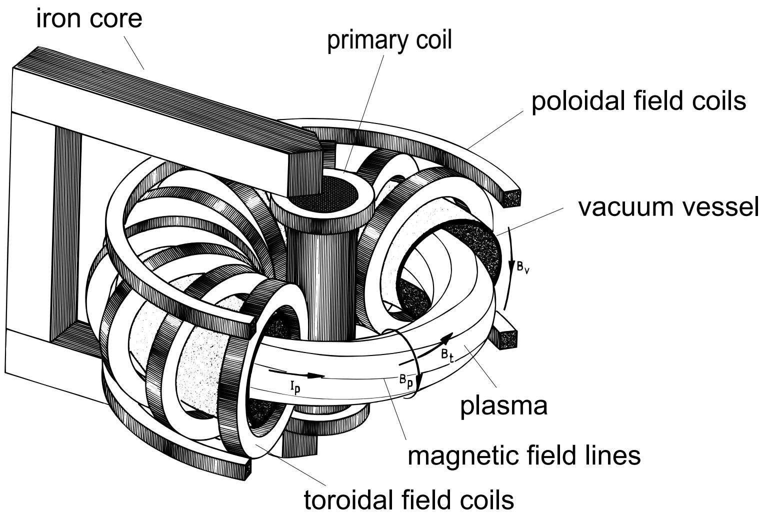

Figure 2.1: Overview of a tokamak. The plasma is confined in the vacuum vessel by the toroidal field B_t. With the help of the iron core, the current flowing in the primary coil induces a current I_p in the plasma. This current results in a poloidal magnetic field B_p. The vertical field B_v is generated by the poloidal field coils and is used to position the plasma horizontally.

give rise to a vertical drift with the velocity:

$$\boldsymbol{v}_{d,vert} = \frac{m}{Q}\frac{v_\parallel^2 + v_\perp^2/2}{RB^2} \tag{2.1}$$

with m, $v_\parallel$ and $\boldsymbol{v}_\perp$ being the mass, parallel and perpendicular velocities of the considered particles, and R the distance to the center of the tokamak. This drift is in opposite direction for ions and electrons, and leads to a charge accumulation at the top and the bottom of the tokamak. The vertical electric field created this way gives rise to a new horizontal drift, directed outwards the torus for both ions and electrons. In such conditions, it would be impossible to sustain any plasma in a tokamak.

The effect of this drift can be avoided by twisting the magnetic field lines. This is achieved by driving a current parallel to $\boldsymbol{B}$ in the plasma, which produces a poloidal magnetic field, typically one order of magnitude smaller than the toroidal one. This current is mostly driven by a transformer whose secondary is the plasma. Figure 2.1 gives an overview of the main magnetic field and coil components in a tokamak.

A magnetic field line followed a large number of turns around the torus covers a magnetic surface of minor radius r (see fig. 2.2). The safety factor q of this surface is defined as

$$q = \frac{rB_\varphi}{RB_\theta} \tag{2.2}$$

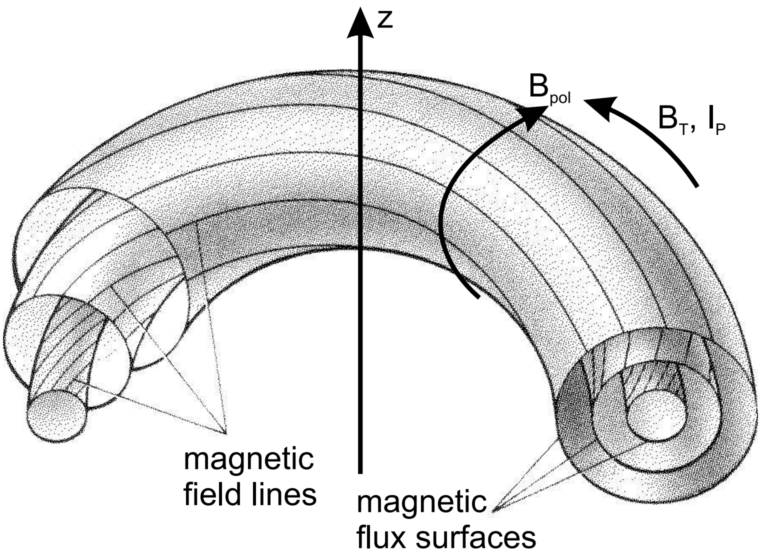

Figure 2.2: Magnetic flux surfaces and field lines in a tokamak. B_{pol} and B_T are the poloidal and toroidal components of the magnetic field, and I_P the plasma current.

where B_φ and B_θ are the toroidal and poloidal components of the magnetic field. It characterizes the mean pitch angle of the field lines on the magnetic surface. Since q depends on r, it gives rise to a twist of field lines between the different magnetic surfaces, characterized by the magnetic shear

$$\hat{s} = \frac{r}{q}\frac{dq}{dr}. \tag{2.3}$$

This shear has an important effect on plasma instabilities. There are particular magnetic surfaces for which $q = M/N$, where M and N are integer numbers. On such surfaces, field lines close upon themselves after N toroidal revolutions, corresponding exactly to M poloidal revolutions. The existence of such surfaces is of importance for turbulent transport, as will be discussed later.

The magnetic geometry of a tokamak consists thus of a series of nested toroidal magnetic surfaces, and a poloidal cut through these surfaces would give nested circles, in the case of a circular tokamak. The equilibrium requires the radial force on the plasma to be zero at all points, i.e. the radial pressure gradient has to be balanced by the Ampere force:

$$\boldsymbol{j} \times \boldsymbol{B} = \boldsymbol{\nabla} p, \tag{2.4}$$

with $\boldsymbol{j}$ being the electric current density, and p the plasma pressure. Solving the Grad-Shafranov equation, which is equation (2.4) expressed in terms of

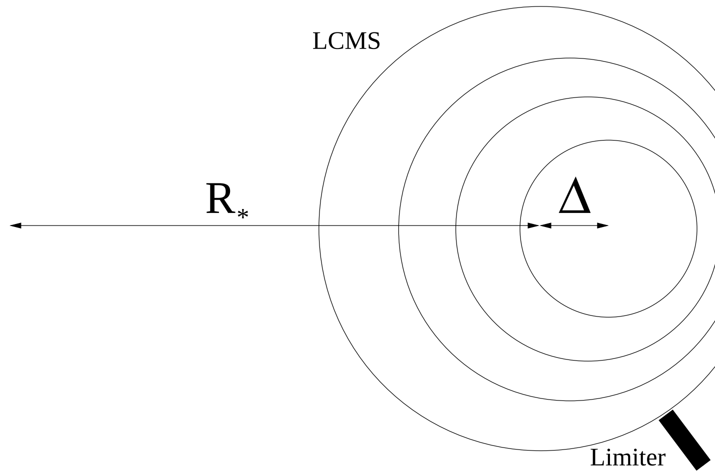

Figure 2.3: Shafranov shift $\Delta(r)$ reducing to zero at the Last Closed Magnetic Surface (LCMS) in a circular limiter tokamak.

flux functions, one notices that the magnetic surfaces are not centered on the same axis (see e.g. reference [67]). The most outward closed surface, the so-called Last Closed Magnetic Surface (LCMS), is determined by a limiter or a divertor. It is centered on the tokamak major radius R_*, and has a minor radius a. More inner magnetic surfaces are shifted outward by a distance $\Delta(r)$. The innermost (degenerated) circle defines the plasma axis, located in $R = R_* + \Delta(0)$ (see fig. 2.3 for the limiter case). Note that equation (2.4) also implies that the pressure gradient is perpendicular to the magnetic surfaces, such that magnetic surfaces are isobars.

2.2 Perturbation by the DED

2.2.1 DED configuration

The installation of the Dynamic Ergodic Divertor (DED) [16] at TEXTOR was completed in 2003. The major and minor radii of this tokamak are respectively of 1.75 m and 46 cm, and it is generally operated with a toroidal magnetic field around $2\,T$. The DED consists of a set of 16 coils plus 2 compensation coils and is shown in fig. 2.4. These coils are located inside the vacuum vessel at the high field side of the torus and are covered with tiles to protect them from the plasma. The pitch angle of the coils is such that they are parallel to the field lines of the $q = 3$ magnetic surface and follow them once around the torus. When supplied with electric current, these coils generate toroidal, poloidal and radial magnetic perturbations. The toroidal

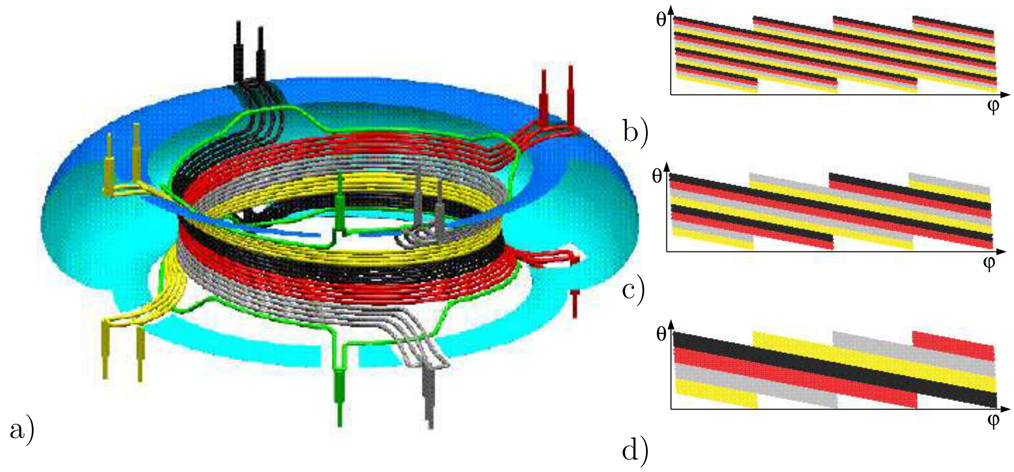

Figure 2.4: a) The 16 perturbation coils of the DED at TEXTOR. Each of the colors corresponds to a phase of the current, and the phase between adjacent coils of different colors is 90°. The uppermost and the bottom coils are compensation coils. The coils can be operated individually, by pair, or by quadruple, as shown respectively in a), b) and c) for the 12/4, 6/2 and 3/1 modes, with θ and φ the poloidal and toroidal angles (Note that there exist other coil configurations for these 3 modes, detailed in reference [17]).

perturbation is much smaller [15] than the two other ones, which are of the same order. However, the radial perturbation has a larger impact on radial transport since it destructs magnetic surfaces. In a stationary operation, it can be represented in the form

$$B_r^{DED} = B_r^0(r) \sin\left(M\theta - N\varphi\right). \tag{2.5}$$

The coils can be fed in three different configurations, $M/N = 12/4$, 6/2 or 3/1. In all of them, the perturbations from the DED coils are resonant with the unperturbed $q = 3$ surface. This surface is located in the edge region, and its radial position can be adapted e.g. by varying the plasma current.

In the 12/4 configuration, the phase difference between currents streaming in neighboring coils is 90°, and a relatively finely structured perturbation is generated. In the 3/1 set-up, the 16 coils are divided into four quadruples of neighboring coils, and each quadruple is fed with the same current. The near-field perturbation in the 3/1 set-up is less finely structured, but penetrates much deeper than in the 12/4 case, which affects only the very edge. The 6/2 configuration is an intermediate case. All these configurations can be operated in DC and AC current at diverse frequencies up to 10 kHz in some situations. The coils can be supplied with currents of several kA, with a maximum of 15 kA in the 12/4 case. The latter case allows a perturbation amplitude at the very edge of the order of 10^{-4} to 10^{-3} [15] for the ratio B_r^{DED}/B, with B the unperturbed amplitude of the magnetic field.

2.2.2 Generation of magnetic island chains

In the presence of the magnetic field perturbation (2.5), the topology of magnetic surfaces changes essentially [21] and a chain of magnetic islands is generated instead of the resonance surface with $q = M/N$, see fig. 2.5. The quantitative description of this new topology is out of the scope of the present work, but the reason for the formation of magnetic islands can be understood from a simple qualitative consideration. For simplification, the poloidal and toroidal perturbations of the magnetic field are neglected, as well as the radial dependence of B_r^{DED}, and the magnetic shear is assumed to be constant and positive, such that q increases with r. Consider a field line intersecting a resonant surface characterized by $q = q_0$ and $r = r_0$. The phase of B_r^{DED} along this field line is determined by the phase variable $\psi = \theta - \varphi/q_0$ according to equation (2.5), with $M_0/N_0 = q_0$, M_0 and N_0 being the poloidal and toroidal mode numbers of the DED perturbation in resonance with the surface $r = r_0$. At the intersection with the resonant surface, $\psi = \psi_0$. Assuming that $B_r^{DED}(\psi_0) > 0$, the field line followed in the direction of increasing φ shows a radial displacement towards larger radii. At the same time, due to the increase of q, the phase variable ψ diminishes. This can be seen by writing the variation of the phase variable ψ:

$$\Delta\psi = \Delta\theta - \frac{\Delta\varphi}{q_0} = \Delta\theta - \frac{q\Delta\theta}{q_0} = \Delta\theta - \frac{\Delta\theta}{q_0}(q_0 + q'(r - r_0)) = -\Delta\theta\frac{q'(r - r_0)}{q_0}$$

which is negative since q increases with r. Due to the the decrease of ψ, B_r^{DED} will vanish at a certain position. From this position, ψ gets still smaller since $q' > 0$ in this region, and B_r^{DED} becomes negative, such that the field line is deviated towards smaller radii. The field line will thus cross the resonant surface a second time at a position A, and from this crossing, ψ will start to decrease because then $q' < 0$. The further evolution of the field line is opposite to the one between the initial position and the position A: ψ increases with φ while $\left|B_r^{DED}\right|$ gets smaller. At a certain point, B_r^{DED} will go to zero again, and from this point, it will be again positive and increasing, while ψ will continue to decrease. Finally, the field line will cross the resonant surface once more, with the same value $\psi = \psi_0$ as at the original position.

Thus, any field line intersecting a resonant surface moves away from this surface, then comes back and crosses it once more, and so on. The projection of such a field line on the (r, ψ) plane gives a closed curve $\mathcal{C}$. Consider now an infinity of field lines crossing the resonant surface at different values of φ, all with $\psi = \psi_0$. In the (r, ψ) plane, they correspond to an infinity of closed curves identical to $\mathcal{C}$, but in the real space, they cover a closed surface whose poloidal cross-section is the curve $\mathcal{C}$ (such curves can be seen

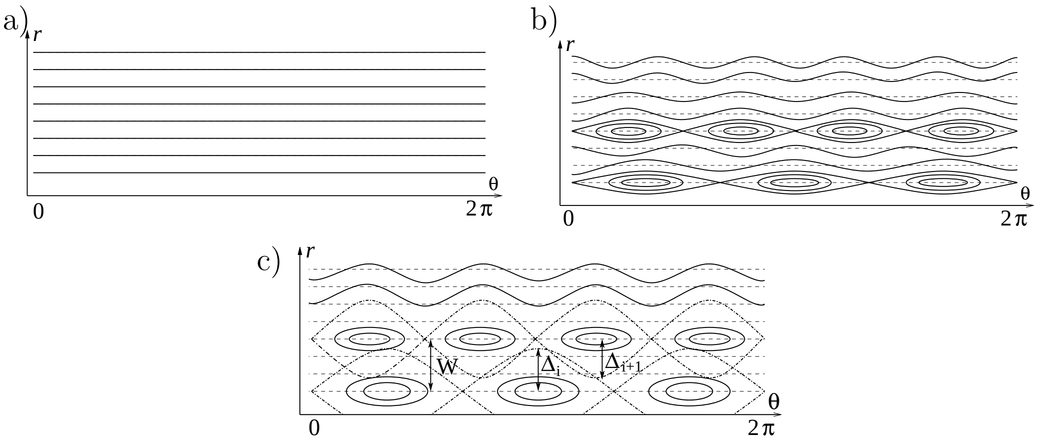

Figure 2.5: Rough representation of magnetic surfaces in the (r, θ) plane, at different DED perturbation levels. a) Without DED, b) moderate perturbation of magnetic surfaces, islands chains are formed on resonant magnetic surfaces and c) island chains with strong stochastization, and overlapping of neighboring island chains. The regions of overlapping are ergodized, only the central part of the islands is not destroyed. Note that an island chain on the M/N resonant surface consists of M islands in the (r, θ) plane, and N islands in the (r, φ) plane, but there are exactly N distinct islands on an M/N resonant surface. Δ_i and Δ_{i+1} are the half-widths of the island chains, and W is the distance between their axes.

in fig. 2.5). By varying the initial phase ψ_0, one would obtain in the real space an infinite set of closed, concentric surfaces. This set of magnetic surfaces is called a *magnetic island*. The term *island chain* refers to all the islands corresponding to the same resonant surface, and *separatrix* is used for the outermost surface of the island chain. Figure 2.6 shows a 2/1 island chain. Note that this island chain actually consists of a single island, though its cross section with a poloidal section of the tokamak contains 2 islands.

An analogy between magnetic island chains and a pendulum can be made by comparing the projection of one field line of a magnetic island on the (r, ψ) plane with the trajectory of the extreme point of a pendulum in the phase space. Consider first a field line inside of the island separatrix. As seen above, its projection on the (r, ψ) plane is a closed surface, comparable to the trajectory of an oscillating pendulum which has not enough energy to reach the upper vertical position, and for which the trajectory in the phase space is an ellipse. Focus now on the field lines lying on the separatrix. Their projection on the (r, ψ) plane is similar to the trajectory of a pendulum which has just the kinetic energy necessary to reach the upper vertical position after an infinite time. Finally, a field line outside of the separatrix corresponds to a pendulum passing regularly through the upper vertical position.

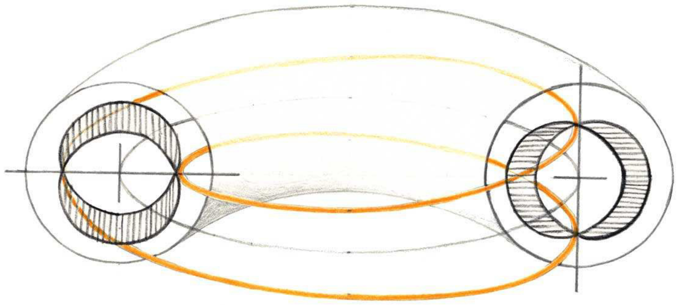

Figure 2.6: View in perspective of 2/1 island. By following the field line passing through the X-point of the island separatrix (orange line), it can be seen that this is a single island.

2.2.3 Stochastization of the magnetic field

Due to the finite extend of the DED and to the discrete localization of the perturbation currents, the actual perturbation B_r^{DED} is more complex than (2.5). Side band modes with different M and N numbers than that from the DED are thus excited as well, and in a Fourier representation, the radial DED perturbation is

$$B_r^{DED} = \sum_{M,N} B_r^{MN}(r) \sin(M\theta - N\varphi) \tag{2.6}$$

where B_r^{MN} are the amplitudes of the different harmonics. The DED generates thus a series of island chains with different M and N numbers.

An increase of the perturbation level will enlarge the island width. From a certain level, neighboring island chains with different mode numbers will overlap each other. The level of overlapping is characterized by the Chirikov parameter $\sigma_{ch} = (\Delta_i + \Delta_{i+1})/W$, where Δ_i and Δ_{i+1} are the half-widths of two adjacent island chains, and W is the distance between the axes of these island chains, see fig. 2.5. For $\sigma_{ch} \sim 1$, the field lines near the separatrices exhibit a stochastic behavior and the separatrices are consequently destroyed. This new magnetic configuration leads to transport between the islands of different island chains directly along the field lines, allowing for *radial* transport of plasma particles and energy *along* the magnetic field. A further increase of σ_{ch} will progressively destroy all magnetic surfaces and finally lead to a complete stochastization of the magnetic field in the region considered.

Some characteristics of the stochastic field can be obtained by field line tracing [24] or by field line mapping [17]. The first method, *field line tracing*, consists in following field lines by numerical integration of the magnetic field

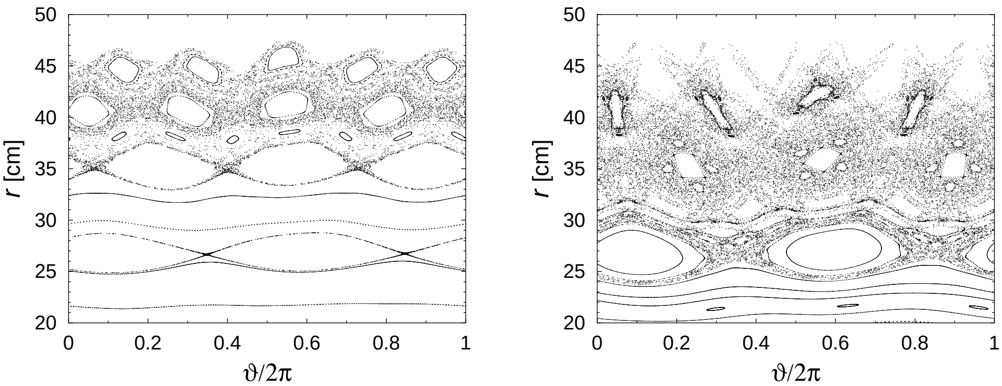

Figure 2.7: Poincaré plots from reference [17], obtained by field line mapping for the TEXTOR DED in a 3/1 configuration, with $B = 2.25\,T$ and with a current of a) 1.46 kA and b) 3.65 kA in the DED coils. These calculations are done for the vacuum, i.e. the only plasma effect taken into account is the macroscopic poloidal magnetic field produced by the plasma current (here 300 kA). Fig. a), can be divided in two regions. The upper one ($r > 35$ cm) is ergodic since island chains are overlapped, with some remnants. The lower one is just slightly perturbed, and one can see there different perturbed magnetic surfaces and an island chain with $M = 2$. The increase of the current, figure b), enlarges the ergodic region till $r \approx 24$ cm. Note the abscissa is the intrinsic angle ϑ, i.e. the poloidal angle θ with a small correction [17] due to toroidal geometry. Changing ϑ to θ would result in a small distorsion along the abscissa.

equations. In the second method, *field line mapping*, one establishes a correspondence between the intersection points of the field lines with two different poloidal cross sections, from some general characteristics of the magnetic geometry. By iteration of the mapping obtained this way, one can follow very fast field lines many times around the torus. This allows e.g. the visualization of the magnetic topology in a *Poincaré plot*. Such a plot shows the points of intersection between a tokamak poloidal cross-section and field lines taken at different radial positions, tracked for several hundredths of toroidal turns. Perturbed magnetic surfaces, island chains and ergodic regions are illustrated in the Poincaré plot 2.7.

Since a one-dimensional code is used to simulate plasma parameters, the description of the stochastic field lines should be restricted to a set of characteristics which depend only on r. In the following, the increase of the distance δ between nearby field lines with the distance l along them is of particular interest. A *statistical* description of this distance can be obtained by applying the formalism of the Hamiltonian dynamics [20]. For large values of l, field lines exhibit a diffusive behavior, i.e. the mean square distance between them evolves as [17, 47, 51]

$$\delta(l)^2 = 2D_{Fl}l \qquad (2.7)$$

where D_{Fl} is the field line diffusivity. For small values of l, the diffusive description fails. In this case, one can use the *Lyapunov exponent*, E_L, which is a quantitative measure of the exponential divergence of neighboring orbits (or of the field line divergence in the ergodic zone) [17, 21]. It is defined[2] by

$$E_L = \lim_{l \to \infty} \frac{1}{l} \ln \frac{\delta(l)}{\delta_0} \tag{2.8}$$

where $\delta_0 = \delta(0)$. The Lyapunov exponent is related to another statistical characteristic of chaotic systems, the *Kolmogorov time* [52] (or *Kolmogorov length* L_K for chaotic field lines), which characterizes the loss of information on the initial state with time. L_K is the inverse of E_L, averaged over a surface of constant r. Thus, on average

$$\delta\,(l) = \delta_0 \exp(l/L_K). \tag{2.9}$$

The increase of $\delta(l)$ is thus described by two expressions, equation (2.9) for $l <$ or $\approx L_K$, and equation (2.7) for $l \gg L_K$. They include two parameters, D_{Fl} and L_K, which depend only on r. The values of these parameters used in the next chapters are taken from computations with field line mapping [17]. Their dependence on the magnetic field perturbation can be obtained from a quasi-linear approximation. According to reference [21], $\sigma_{ch} \sim \sqrt{b}$, $D_{Fl} \sim b^2$ and $L_K \sim b^{-2/3}$, with $b = \delta B/B_0$, δB being the magnetic pertubation and B_0 the unperturbed magnetic field. The quasi-linear approximation generally overestimates the values of these parameters [17]. Typically, $D_{Fl} \approx 5 \cdot 10^{-6} - 2 \cdot 10^{-5}$ m, $L_K \approx 30-100$ m and $\sigma_{ch} \approx 0.8-1.3$ in the edge region for the DED operated in the 3/1 or 6/2 mode (values from field line mapping). For the 12/4 mode, which induces a smaller perturbation, the field line diffusivity and the Chirikov parameter are smaller than these values, and the Kolmogorov length is larger.

The description of stochastic field lines used here holds for infinite field lines [21]. However, though perturbed magnetic field lines are not limited in any way, at the plasma edge they are connected to the walls. This limits the motion of particles along them and introduces a new characteristic in the analysis of transport along the field lines. One defines the *connection length* of a point, L_c, as the shortest distance to the walls, taken along the field line passing through it. A comparison between L_c and L_K permits to distinguish between two regions at the boundary. In the region for which $L_c \gg L_K$, stochasticity prevails. This region is called the ergodic zone.

[2] Due to the finite connection length (see definition below), it is impossible to determine the global Lyapunov exponent according to equation (2.8), but a finite-time (or finite-length) Lyapunov exponent can be obtained by using a finite value for l in equation (2.8) [17].

On the contrary, in the region with $L_c \ll L_K$, the dominant effect is the connection to the walls. The latter region is called the laminar zone.

2.3 Model for effective transport in a stochastic magnetic field

The model of reference [61] is chosen as the basis for the description of radial transport in a stochastic magnetic field. Here this model is developed further by introduction of:

- a more relevant geometry for transport paths[3]

- the limitation of the particle velocity to the sound speed

- a more accurate description of the parallel velocity radial profile being of importance for viscous terms

- the anomalous perpendicular pinch velocity.

The assumptions done in the model are verified, and a comparison with other models is performed. However, in the laminar zone, the short connection length modifies completely the properties of the transport, which occurs then only along the field lines, and other approaches should be applied. Therefore, the calculations with RITM are done in the core region bounded by the laminar zone. An estimate for the radial width of the laminar zone is presented in chapter 4.

In sections 2.3.1 and 2.3.2, the models of reference [61] for heat transport and for background particle transport, and their improved versions, are presented.

2.3.1 Heat transport

Consider a heated plasma in a stationary state. The total radial heat flux is the heat transported by different particle species in the plasma, as well as through radiation. It is determined by the heating power. Consider now a radial heat flux of density q_r transfered by electrons, along a path as the one illustrated in fig. 2.8. Such a path is composed of a succession of segments parallel and perpendicular to the magnetic field, of lengths L and δ_0,

[3]more precisely, the averaged radial temperature gradient was approximated by $\frac{(\Delta_\perp T_e)/2+\Delta_\parallel T_e}{\delta_L/2}$ in reference [61] instead of equation (2.10) here, and a similar estimation was used for the averaged radial density gradient, to be compared with equation (2.23).

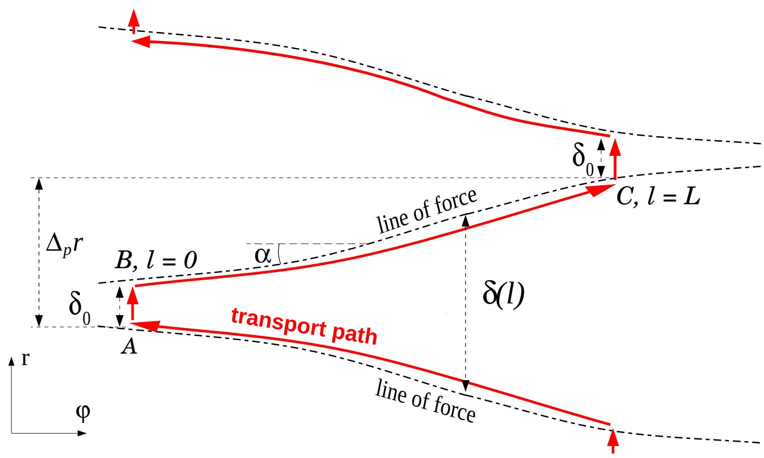

Figure 2.8: Transport path in a stochastic magnetic field. r and φ are the coordinates in the radial and toroidal directions, l is the coordinate along field lines, and α is the angle between the path and a surface of constant radius r. δ_0 and L are the lengths of the perpendicular (A to B) and parallel (B to C) segments of the path, and $\Delta_p r$ is the radial extend of the elementary piece of path.

respectively. The radial heat conductivity along this path, κ^{path}, is defined by

$$q_r = -\kappa^{path}\overline{\nabla}_r T_e = -\kappa^{path}\frac{\Delta_p T_e}{\Delta_p r} = -\kappa^{path}\frac{\Delta_\perp T_e + \Delta_\parallel T_e}{\left(\delta_0 + \delta_L\right)/2}, \tag{2.10}$$

where $\overline{\nabla}_r T_e$ is the radially averaged temperature gradient along the elementary piece of the path. It is taken as the ratio of the temperature change $\Delta_p T_e$ along the elementary piece of the path (from A to C in fig. 2.8) to the radial extend $\Delta_p r$ of this piece. $\Delta_\perp T_e$ and $\Delta_\parallel T_e$ are the changes of electron temperature T_e along the perpendicular and parallel parts of the elementary path piece (respectively from A to B and from B to C in fig. 2.8), and $\delta_L = \delta\left(L\right)$.

It is shown in this section that there are 'optimal' paths, along which the radial heat conductivity is the largest. Since this radial heat conductivity is the largest, it will dominate the heat transfer, and will be henceforth referred to as the effective heat conductivity κ^{eff}. For a given heat flux, κ^{eff} controls the radial temperature gradient in the ergodic layer:

$$\langle\nabla_r T_e\rangle = -\frac{q_r}{\kappa^{eff}}. \tag{2.11}$$

where $\langle\quad\rangle$ means averaging over the poloidal and toroidal angles. Indeed, on the one hand, the amplitude of $\langle\nabla_r T_e\rangle$ cannot be smaller than q_r/κ^{eff}, since κ^{eff} is the maximal reachable radial heat conductivity. On the other hand, if the amplitude of $\langle\nabla_r T_e\rangle$ were larger than q_r/κ^{eff}, heat transfer along the 'optimal' paths would produce large flows, reducing thereby the amplitude of the temperature gradient.

κ^{path} is now determined on the basis of equation (2.10). Perpendicular segments of path correspond to the places where perpendicular temperature gradients are so large that parallel heat transport is neglected with respect to radial heat transport. In this case, $\Delta_\perp T_e$ can readily be written

$$\Delta_\perp T_e = -\frac{q_r}{\kappa_\perp}\delta_0 \tag{2.12}$$

with the perpendicular temperature gradient estimated as $\Delta_\perp T_e/\delta_0$, and where $\kappa_\perp$ is the intrinsic perpendicular heat conductivity. The latter results from collisions and anomalous transport, and is determined in the next chapter.

Parallel segments of path correspond to places where parallel heat transfer contributes largely to the radial heat transfer. The radial heat flux has thus contributions from both parallel and perpendicular heat fluxes:

$$q_r = -\kappa_\parallel \sin\alpha \frac{\partial T_e}{\partial l} - \kappa_\perp \nabla_\perp T_e. \tag{2.13}$$

with $\kappa_\parallel$ the heat conductivity along field lines, and $\alpha\,(l)$ the angle between the direction of the segment and a surface of constant radius r. The perpendicular temperature gradient can be found only by a 3D calculation, such that a simplified expression is sought. Taking $\nabla_\perp T_e = 0$ is not satisfactory, since it leads to $\kappa^{path} \longrightarrow 0$ for $L \longrightarrow \infty$ and $\kappa^{path} \neq \kappa_\perp$ for $L = 0$, as can be seen in fig. 2.9. This reflects the fact that the contribution of perpendicular heat transport to q_r is not negligible, at least for small values of L. It is henceforth assumed that $\nabla_\perp T_e \approx \Delta_\parallel T_e/((\delta_L - \delta_0)/2)$, i.e. $\nabla_\perp T_e$ is replaced by its averaged value. With this approximation, equation (2.13) can be integrated in order to find the $T_e(l)$ dependence. Together with equation (2.10), it leads to (see appendix A)

$$\kappa^{path} = \kappa_\perp \left(1 + \frac{1}{2}\frac{\zeta_K\left(e^X - 1\right)}{\zeta_K + 1 + e^{-X}}\right) \tag{2.14}$$

with $\zeta_K = \kappa_\parallel \delta_0^2/\left(2\kappa_\perp L_K^2\right)$ and $X = L/L_K$, in the case $L \lesssim L_K$. For $L \gg L_K$, one has

$$\kappa^{path} = \kappa_\perp + \frac{3}{8}\kappa_\parallel \frac{D_{Fl}}{L}. \tag{2.15}$$

With equation (2.14), κ^{path} increases with L. On the contrary, in equation (2.15), κ^{path} decreases with L. The paths for which δ_L satisfies both equations (2.9) and (2.7) have thus the largest heat conductivity. This conditions provides one relation between δ_0 and L for the optimal paths:

$$\delta_0 \exp\left(L/L_K\right) = \sqrt{2D_{Fl}L}, \tag{2.16}$$

in agreement with the results of the variational analysis in references [20] and [21]. The elimination of δ_0 between equations (2.14) and (2.16) leads to

$$\kappa^{path} = \kappa_\perp \psi_K \tag{2.17}$$

with

$$\psi_K = \left(1 + \frac{1}{2}\frac{\zeta_T X\left(1 - e^{-X}\right)}{\zeta_T X e^{-X} + 1 + e^X}\right) \tag{2.18}$$

and $\zeta_T = (D_{Fl}/L_K)(\kappa_\parallel/\kappa_\perp)$. One can see in equation (2.17), as well as in fig. 2.9, that κ^{path} has a maximum as a function of X at a certain X_T. This maximum is taken as the effective heat conductivity κ^{eff}. Note that the existence of this maximum is a consequence of the different expressions for δ in the two limits $l \lesssim L_K$ and $l \gg L_K$.

In the derivation of equations (2.14), (2.15) and (2.17), it has been assumed that $\kappa_\parallel$ is determined by the local plasma parameters. Typically, the Spitzer-Härm (SH) formula[5] is used for electrons: $\kappa_{SH} \approx 3.16\, n_e v_{th,e} \lambda_{th,e} \sim T_e^{5/2}/Z_{eff}$, with n_e the electron density, $v_{th,e}$ the velocity of thermal electrons, $\lambda_{th,e}$ the mean free path length of thermal electrons, and Z_{eff} the effective ion charge. This formula was derived[56] in a fluid description of the plasma, under the assumption that the motion of particles is determined by collisions, i.e. $\lambda_{th,e} \ll L_{T_e,\parallel}$, with $L_{T_e,\parallel} = |\partial \ln T_e/\partial l|^{-1}$ the e-folding length of T_e along field lines. However, the major contribution to $\kappa_\parallel$ comes from electrons with a velocity 3-5 times larger than the thermal velocity [9]. Since the mean free path length is proportional to the fourth power of the velocity, these electrons, called *heat carrying electrons*, have a mean free path by a factor of ≈100-500 larger than thermal electrons. The validity condition for the SH approximation is then actually $\lambda_{hc,e} \ll L_{T_e,\parallel}$, with $\lambda_{hc,e}$ the mean free path of heat carrying electrons. Under the considered plasma conditions, this condition may be violated and a significant deviation from the SH approximation can occur. For instance, according to the SH formula, if $\lambda_{th,e} \longrightarrow \infty$, even a slight $\nabla_\parallel T_e$ would give an infinite heat flux. Computation of $q_{\parallel,M}$, the one-way heat flux density for a Maxwellian velocity distribution, yields $q_{\parallel,M} = \pi^{-1/2} n_e v_{th,e} T_e$, which provides some indication of a limit for the actual heat flux density for $\lambda_{th,e} \longrightarrow \infty$. Accordingly, a saturation of the flux occurs at a level $q_{\parallel,limit} = \alpha_e n_e v_{th,e} T_e$ ([57], chapter 26), with α_e ranging from 0.03

to 3 [18], and a kinetic correction is applied to $q_\parallel$ in the form of a geometric mean

$$\frac{1}{q_\parallel} = \frac{1}{q_{\parallel,SH}} + \frac{1}{q_{\parallel,limit}}. \tag{2.19}$$

This would lead to the application of a correction factor $(1+\alpha_e^{-1}\lambda_{th,e}/L_{T_e,\parallel})^{-1}$ to κ_{SH}. Rather than using $\alpha_e^{-1}\lambda_{th,e}$ and varying the more or less arbitrary value of the parameter α_e, the idea of ref. [41] is followed and the kinetic correction applied in the form

$$\kappa_\parallel \approx \frac{\kappa_{SH}}{1+\lambda_{hc,e}/L_{T_e,\parallel}}, \tag{2.20}$$

where $\lambda_{hc,e} = \lambda_{th,e}(v_{hc,e}/v_{th,e})^4$, and $v_{hc,e}$ is the velocity of heat carrying electrons. The influence of the ratio $v_{hc,e}/v_{th,e}$ on $\lambda_{hc,e}$ is then investigated on the range 3-5. For the term $L_{T_e,\parallel}$, $L_{T_e,\parallel} = 1/\overline{|\partial \ln T_e/\partial l|}$ is assumed, where $\overline{|\partial \ln T_e/\partial l|}$ is the mean value of $|\partial \ln T_e/\partial l|$ over a parallel segment of path:

$$L_{T_e,\parallel}^{-1} \approx \overline{|\partial \ln T_e/\partial l|} \approx \frac{1}{L_{T_e}}\sqrt{\frac{D_{Fl}}{2L_K X}}\left(1-e^{-X}\right) \tag{2.21}$$

with $L_{T_e} = |\partial \ln T_e/\partial r|^{-1}$ the radial e-folding length of T_e (for detailed calculation see appendix A).

All the reasoning of section 2.3.1 can be followed for ions, with $\kappa_\parallel$ and $\kappa_\perp$ computed for ions. The main difference lies in the SH heat conductivity of ions which is less by a factor of $\approx \sqrt{m_e/m_i}$ for ions than for electrons. For completeness, the values of κ_{SH} and λ_{th} for both ions and electrons are given:

$$\begin{aligned}\kappa_{SH,e} = 3.16 n_e v_{th,e}\lambda_{th,e} \approx 10^{22}\frac{T_e^{5/2}}{Z_{eff}}, \quad \lambda_{th,e} = v_{th,e}\tau_e \approx 8\cdot 10^{15}\frac{T_e^2}{n_e Z_{eff}} \\ \kappa_{SH,i} = 3.9 n_i v_{th,i}\lambda_{th,i} \approx 4.3\cdot 10^{20}\frac{T_i^{5/2}}{Z_{eff}^4\sqrt{\mu_p}}, \quad \lambda_{th,i} = v_{th,i}\tau_i \approx 1.13\cdot 10^{16}\frac{T_i^2}{n_i Z_{eff}^4}\end{aligned} \tag{2.22}$$

with τ_e and τ_i the electron and ion collision times[4], explicited in reference [5], and $\mu_p = m_i/m_p$, m_p being the proton mass. Temperatures are expressed in eV, densities in m^{-3}, lengths in m and heat conductivities in m^{-1}s^{-1}. Finally, the determination of $\kappa_\perp$ for both ions and electrons is the subject of the next chapter.

[4]The collision time of a species is defined as the mean time necessary to deviate the trajectory of a particle of this species by an angle of 90°.

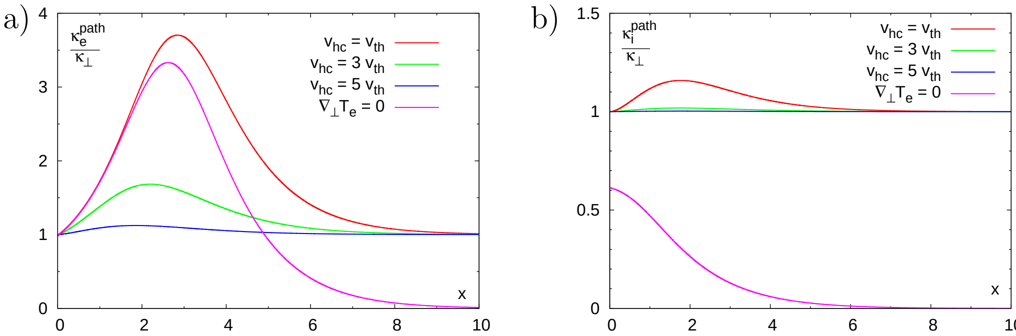

Figure 2.9: Heat conductivity of a) electrons and b) ions along a path according to equation (2.17), without and with kinetic corrections to κ_{SH}. Two different assumptions are made for the kinetic correction, namely the speed of heat carrying particles is 3 or 5 times the thermal velocity. The result of the assumption $\nabla_\perp T_e = 0$ in equation (2.13) is also shown. The parameter values are taken for typical TEXTOR edge conditions, namely $D_{Fl} = 10^{-5} m$, $L_K = 50\, m$, $Z_{eff} = 1$, $m_i = 2m_p$, $T_e = T_i = 150\, eV$, $\kappa_{\perp,e} = \kappa_{\perp,i} = 10^{19}\ m^{-1}s^{-1}$, $n = 10^{19} m^{-3}$ and $L_{T_e} = L_{T_i} = 5\, cm$, which corresponds to $\zeta_T = 55$ for electrons and $\zeta_T = 1.7$ for ions.

Figure 2.9 and 2.10.a show respectively $\kappa^{path}/\kappa_\perp$ and $\kappa^{eff}/\kappa_\perp$, both for $\kappa_\|$ with and without kinetic corrections. Figure 2.10.b shows X^{eff}, the value of X for which κ^{path} is maximum, as a function of ζ_T. Typically, $\zeta_T \sim 50$, but it can be much larger.

This section is concluded by summarizing the different steps to obtain κ^{eff}. First, an effective heat conductivity is defined by relating the temperature gradient averaged over the poloidal and toroidal angles to the radial heat flux transported by conduction by the considered particles. Then, the heat conductivity along different paths, differing by their lengths along and across the magnetic field, is calculated in the exponential and diffusive approximations for the field line divergence. From the condition that 'optimal' paths lead to the highest possible heat conductivity, a relation between the parallel and perpendicular dimensions of the optimal path is deduced. The effective heat conductivity is then obtained by determining the last free parameter, the parallel dimension of the path, through a maximization of κ^{path} versus this dimension. Finally, kinetic effects have been considered.

2.3.2 Transport of background particles

For particle transport, an approach similar to the one for heat transport is followed. A plasma in a stationary state with a negligible particle source is considered, in which a radial flux Γ_r of background particles streams along a path as the one displayed in fig. 2.8. D^{path}, the particle diffusivity along this path, and V^{path}, the pinch velocity related to this path are defined by

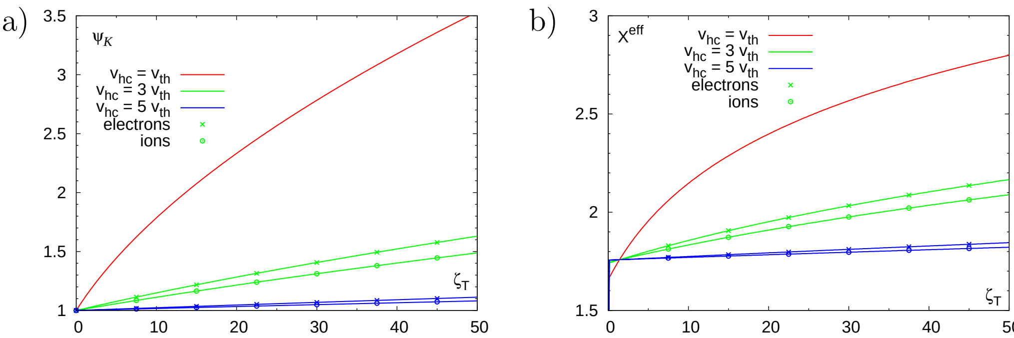

Figure 2.10: a) $\psi_K = \kappa^{eff}/\kappa_\perp$ for electrons and ions, without and with kinetic corrections. Two different assumptions are made for the kinetic correction, i.e. $v_{hc} = 3v_{th}$ and $v_{hc} = 5v_{th}$. The parameter values are the same as in fig. 2.9. Note that in all cases, the abscissa corresponds to the value of ζ_T for $v_{hc} = v_{th}$. b) X^{eff}, the value of X for which κ^{path} is maximal.

the following relation

$$\Gamma_r = -D^{path}\overline{\nabla}_r n + V^{path} n = -D^{path}\frac{\Delta_\perp n + \Delta_\parallel n}{(\delta_L + \delta_0)/2} + V^{path} n \tag{2.23}$$

where $\overline{\nabla}_r n$ is the average density gradient. With a similar reasoning as the one of section 2.3.1, one finds that the paths with the largest *particle* transport ('optimal' paths) determine the average radial density gradient. In order to define effective transport coefficients, i.e. D^{path} and V^{path} for the optimal paths, the value of these two coefficients is computed as a function of the path dimensions δ_0 and L, and the maximum of these coefficients with respect to δ_0 and L is sought (note that the optimal paths for heat and particle transport are different).

The change of density $\Delta_\perp n$ along the perpendicular part of the path (from A to B in fig. 2.8) can be found from the radial flux along this segment of path:

$$\Gamma_r = -D_\perp \frac{\Delta_\perp n}{\delta_0} + V_\perp n \tag{2.24}$$

where $D_\perp$ and $V_\perp$ are the anomalous perpendicular particle diffusivity[5] and pinch velocity. The first term on the right-hand side of equation (2.24) represents thus conductive transport, while the second stands for convective

[5]Since the concentration of impurities is very low compared to the ion density, and since only background ions of H or its isotopes are considered, it is assumed that $n_e \approx n_i \approx n$. In the present model, the electron and ion fluxes are assumed to be equal, both along and across the magnetic field lines, such that they have identical diffusivities and particle velocities, written $D_\perp$ and $V_\perp$.

transport, including terms proportional to the gradient of different quantities. The change of density along the parallel segment of the path (from B to C), $\Delta_{\|}n$, can be obtained from the particle balance along the field lines

$$\begin{aligned}\Gamma_r &= nV_{\|}\sin\alpha - D_{\perp}\nabla_{\perp}n + V_{\perp}n \\ &= nV_{\|}\sin\alpha - D_{\perp}\frac{\Delta_{\|}n}{(\delta_L-\delta_0)/2} + V_{\perp}n\end{aligned} \tag{2.25}$$

with $V_{\|}$ the parallel mass velocity, in the direction B to C in fig. 2.8. The first term on the right-hand side represents a flow along the field lines, while the two other ones account for pure perpendicular transport, as in equation (2.24). The perpendicular density gradient is approximated in a similar way as it was done for the perpendicular temperature gradient in equation (2.13). The parallel velocity is determined by the force balance along the field lines, which is given by the sum of the equations of motion for the electrons and the background ions [5]. For a stationary state, its projection onto the parallel direction gives:

$$m_i\frac{\mathbf{\Gamma}_{\perp}}{n}\cdot\nabla_{\perp}\left(nV_{\|}\right) + m_i\frac{\mathbf{\Gamma}_{\|}}{n}\cdot\nabla_{\|}\left(nV_{\|}\right) = -\nabla_{\|}p - \left(\nabla\cdot\overleftrightarrow{\pi}_i\right)_{\|} \tag{2.26}$$

where $p = n\,(T_e + T_i)$ is the plasma pressure, $\Gamma_{\perp}$ and $\Gamma_{\|}$ are the perpendicular and parallel heat flows, and $\overleftrightarrow{\pi}_i$ the ion stress tensor. Due to the much lower viscosity of electrons, the electron stress tensor is neglected. According to reference [5], the stress tensor is

$$\left(\nabla\cdot\overleftrightarrow{\pi}_i\right)_{\|} = -\nabla_{\perp}\cdot\left(m_i\mu_{\perp}n\nabla_{\perp}V_{\|}\right) - \nabla_{\|}\left(m_i\mu_{\|}n\nabla_{\|}V_{\|}\right). \tag{2.27}$$

In the following, the ordering $\delta < L_n \ll L$ is adopted, where L is the length of the parallel path segment. It is indeed found below that L exceeds L_K, which is most of the time larger than $10\,m$ in TEXTOR experiments, and one can check afterwards that δ lies generally under the centimeter. As for L_n, the perpendicular e-folding length of density, it is generally of the order of several centimeters.

The first derivatives of $V_{\|}$ are approximated with a division by the appropriate characteristic length: $\nabla_{\perp}V_{\|} \approx V_{\|}/\delta$ and $\nabla_{\|}V_{\|} \approx V_{\|}/L$. Its second derivatives are taken in the form of a division by the square of this characteristic length, with the suitable sign. For the perpendicular derivative, this yields $\nabla^2_{\perp}V_{\|} \approx -V_{\|}/\delta(l)^2$, which reproduces a decreasing importance of viscous terms with increasing distance between field lines [61]. However, viscous terms should be similar at both ends of the parallel segment of path (points B and C in fig. 2.8), such that the following approximation is adopted:

$\nabla_\perp^2 V_\parallel \approx -V_\parallel[(1/\delta(l))^2 + (1/\delta(L-l))^2]$. For the parallel derivative the approximation, reads $\nabla_\parallel^2 V_\parallel \approx V_\parallel/L^2$. With the assumptions that $\nabla_\parallel n \approx n/L$ and since the ratio $\mu_\parallel/\mu_\perp$ is very small[6], one notices that the second term on the right-hand side of equation (2.27) can be neglected with respect to the first one. According to references [6] and [53], the further assumption that the plasma flow is subsonic is made, i.e. that $V_\parallel$ is much smaller than the sound speed. This allows to neglect the second term on the left-hand side of equation (2.26). The validity of this assumption is discussed below. Finally, $\Gamma_\parallel = nV_\parallel$, and $\Gamma_\perp/n$ is approximated with $D_\perp/L_n + V_\perp$, where $L_n = |\partial \ln n/\partial r|^{-1}$. Equation (2.26) can now be rewritten[7]:

$$\begin{aligned}\frac{\partial p}{\partial l} = -m_i\mu_\perp nV_\parallel \left(\left(\frac{1}{\delta(l)}\right)^2 + \left(\frac{1}{\delta(L-l)}\right)^2\right) - m_i\frac{\mu_\perp}{L_n}\frac{nV_\parallel}{\delta(l)} - \\ - m_i\left(\frac{D_\perp}{L_n} + V_\perp\right)\frac{nV_\parallel}{\delta(l)},\end{aligned} \tag{2.28}$$

in which one can see that the parallel pressure gradient is determined by the perpendicular viscosity, with two corrections of the first order in δ/L_n; one due to viscosity, and one due to mass exchange between adjacent field lines along which $V_\parallel$ is different.

Equations (2.25) and (2.28) are integrated in appendix B, giving first $\Delta_\parallel n$ and then D^{path} and V^{path}. In the case $L \lesssim L_K$, one obtains:

$$\begin{aligned}D^{path} &= D_\perp\left[1 + \frac{1}{2}\frac{e^X - 1}{1 + g(X)}\right] \\ V^{path} &= V_\perp + \frac{D^{path} - D_\perp}{L_T}\end{aligned} \tag{2.29}$$

with

$$\begin{aligned}g(X) =& \frac{1}{\zeta_D}\frac{e^X + 1}{e^X - 1}\times \\ &\times\left[\frac{1 - e^{-3X}}{3} + e^{-X}\left(1 - e^{-X}\right) + \left(\frac{D_\perp + \mu_\perp}{\mu_\perp L_n} + \frac{V_\perp}{\mu_\perp}\right)\delta_0\frac{1 - e^{-2X}}{2}\right],\end{aligned}$$

[6]The ratio $\mu_\parallel/\mu_\perp^{cl}$ is of the order of $\omega_{ci}\tau_e$ [5], which is a very small quantity. Additionally, the anomalous perpendicular viscosity $\mu_\perp$ should be considered here, which is much larger than the classical perpendicular viscosity.

[7]Note that the term $m_iV_\perp V_\parallel\nabla_\perp n$ is neglected as well since it gives a second order correction in the small parameter δ/L_n.

$\zeta_D = c_s^2\delta_0^4/\left(2\mu_\perp D_\perp L_K^2\right)$ and $c_s = \sqrt{\left(T_e+T_i\right)/m_i}$ the sound speed. In the case $L \gg L_K$, one has:

$$\begin{aligned} D^{path} &= D_\perp\left[1+\frac{\zeta_n}{4}\left[\ln\frac{2L}{\delta_0}+\left(\frac{D_\perp+\mu_\perp}{\mu_\perp L_n}+\frac{V_\perp}{\mu_\perp}\right)\sqrt{2D_{Fl}L}\right]^{-1}\right] \\ V^{path} &= V_\perp+\frac{D^{path}-D_\perp}{L_T} \end{aligned} \tag{2.30}$$

where $\zeta_n = \left(2c_sD_{Fl}\right)^2/\left(D_\perp\mu_\perp\right)$. One can see that D^{path} and V^{path} increase with L in the case $L \lesssim L_K$, and that they decrease with L for $L \gg L_K$. The particle transport along the paths for which δ_L satisfies both equations (2.9) and (2.7) will thus be the largest. Like for heat conductivity, condition (2.16) is inserted into equations (2.29) with the purpose of eliminating δ_0:

$$D^{path} = D_\perp\psi_D, \qquad V^{path} = V_\perp+\frac{D_\perp}{L_T}\left(\psi_D-1\right) \tag{2.31}$$

with

$$\psi_D = \left[1+\frac{1}{2}\frac{e^X-1}{1+h\left(X\right)}\right] \tag{2.32}$$

and

$$\begin{aligned} h(X) = {}& \frac{e^X}{\zeta_nX^2}\frac{e^X+1}{e^X-1}\times \\ &\times\left[\frac{e^{3X}-1}{3}+e^X\left(e^X-1\right)+\left(\frac{D_\perp+\mu_\perp}{\mu_\perp L_n}+\frac{V_\perp}{\mu_\perp}\right)\sqrt{2D_{Fl}L_KX}\frac{e^{2X}-1}{2}\right]. \end{aligned}$$

Figure 2.11 illustrates the X dependence of D^{path} in equation (2.31) for particular values of the parameters D_{Fl} and L_K. One sees that it has a maximum, corresponding to the most efficient path for particle transport (V^{path} is maximum at the same position). This maximum determines D^{eff} and V^{eff}, which are shown in fig. 2.12 as a function of the parameter ζ_n. This parameter is generally of the order of 20 in the stochastic region in TEXTOR, and rarely exceeds 50.

The assumptions are now verified. First, for both heat and particle transport, transport coefficients were computed with the assumption that δ increases exponentially with l, and condition (2.16) was introduced into the obtained coefficients. A glance at fig. 2.10 and 2.12 shows that X^{eff}, the value of X corresponding to the maxima of the transport coefficients, is always larger than 1.18, and does not exceeds a value of about 3. It is thus in the expected range, i.e. between the two extremes $L \lesssim L_K$ and $L \gg L_K$, which was required for making assumption (2.16). Secondly, the correctness of the assumption that the parallel particle flow is subsonic is checked. It is justified if the neglected term is small with respect to the main term in equation (2.28):

$$\frac{m_i n V_\parallel \partial V_\parallel / \partial l}{\nabla_\perp \cdot \left(m_i \mu_\perp n \nabla_\perp V_\parallel\right)} \approx \frac{\overline{V}_\parallel \delta^2}{L \mu_\perp} \ll 1 \tag{2.33}$$

where $\overline{V}_\parallel$ is the mean value of $V_\parallel$ along a parallel section of path (see appendix C). Figure 2.13 shows this ratio as a function of ζ_n. One can see that the assumption fails when ζ_n significantly exceeds 1. In the latter case, the flow along the field lines dominates viscous terms in equation (2.26). Integration of the parallel pressure gradient yields then

$$\int_0^L \frac{\partial p}{\partial l} dl \approx -\int_0^L m_i n V_\parallel \frac{\partial V_\parallel}{\partial l} dl \tag{2.34}$$

or

$$\Delta_\parallel \Big(n(T_e + T_i) \Big) \approx -m_i n \Delta_\parallel V_\parallel^2. \tag{2.35}$$

There is thus a limitation for $V_\parallel$: $V_\parallel \leq c_s$. In the extreme case where the parallel velocity becomes comparable to the sound velocity, radial particle transport due to stochasticity will reach the limit value $\Gamma_{stoc} \approx D_{Fl} c_s \nabla_r n$ [53, 60]. By keeping both terms $m_i n V_\parallel \partial V_\parallel / \partial l$ and $\nabla_\perp \cdot \left(m_i \mu_\perp n \nabla_\perp V_\parallel\right)$, an analytical calculation of D^{path} and V^{path} is practically impossible. Solving it numerically is out of the scope of the present work, since it would lead to too long computation times with the code RITM. Consequently, particle transport is henceforth described by equation (2.31), and the condition $\Gamma_r < -(D_\perp + D_{Fl} c_s) \nabla_r n + V_\perp n$ is added, reflecting the limitation induced when a sonic regime is approached. In concrete terms, curves of fig. 2.12 are limited at $D^{eff} = 1.07 D_\perp$ for $D_{Fl} = 10^{-6}\, m$ and $D^{eff} = 1.7 D_\perp$ for $D_{Fl} = 10^{-5}\, m$.

Some differences between heat and particle transport models in stochastic fields are now stressed. In both cases, a flux is assumed to take place along the field lines, but their properties are slightly different: in the case of heat, this flux is due to conduction, and is thus proportional to the parallel temperature gradient. For the particle flow, the parallel flux is driven by the pressure gradient, but it is limited by viscosity, such that it is proportional neither to the pressure gradient, nor the density gradient. That is why in the case of particle diffusion there is no point for a kinetic correction like the one introduced for parallel heat conductivity.

2.4 Comparison with models from literature

The model of Rechester and Rosenbluth [51], established 30 years ago and being probably the most widely referenced in the field, is first considered. Like the models of section 2.3.1 and reference [61], this model assumes magnetic surfaces which are destroyed by overlapping of neighboring island chains, but only heat diffusion is envisaged, in two different cases: collisionless ($\lambda_{th,e} \gg L_K$) and collisional ($\lambda_{th,e} \ll L_K$). Since TEXTOR edge is characterized by $\lambda_{th,e} \ll L_K$, only the second case is discussed. In this case, a solution is sought in the form of a random walk. The radial displacement is seen as a diffusive process. The square of the radial step size is estimated as $\langle(\Delta r)^2\rangle = D_{Fl} L_{c\delta}$, where $L_{c\delta}$ is an estimation of the correlation length of the perturbation along the field lines: $L_{c\delta} = L_K \ln((L_{c,r}/L_K)\sqrt{\kappa_\parallel/\kappa_\perp})$. The correlation length of the perturbation in the radial direction, $L_{c,r}$, is assumed to be $L_{c,r} \approx r/M$, with M the dominating perturbation mode number at the considered radial position. The characteristic time for a radial step Δr is estimated on the base of the parallel heat diffusivity: $t_\delta \approx L_{c\delta}^2/\kappa_\parallel$. One obtains thus a radial heat conductivity in the form

$$\kappa_r = \frac{D_{Fl}\kappa_\parallel}{L_{c,\delta}}. \tag{2.36}$$

There is a fundamental difference between the radial heat conductivities of the model of Rechester and Rosenbluth, and the model developed here. Equation (2.36) gives a diffusion coefficient proportional to $\kappa_\parallel$, with a weak dependence on the ratio $\kappa_\parallel/\kappa_\perp$. On the contrary, equation (2.17) expresses the radial heat conductivity as basically proportional to $\kappa_\perp$, multiplied by a function of the ratio $\kappa_\parallel/\kappa_\perp$. In the case of a very low perpendicular heat conductivity, the Rechester and Rosenbluth model would thus lead to a much larger radial heat conductivity than the model developed here. A quantitative estimation of κ_r, with $D_{Fl} = 10^{-5}\,m$, $L_K = 50\,m$, $T_e = 150\,eV$, $n_e = 10^{19}\,m^{-3}$, $Z_{eff} = 1$, $r = 40\,cm$, $M = 12$ and $\kappa_\perp = 10^{19}\,m^{-1}s^{-1}$ yields $\kappa_r = 2.3\cdot10^{20} m^{-1}s^{-1}$ and $\kappa_e^{eff} = 1.7\cdot10^{19} m^{-1}s^{-1}$ (with $v_{hc,e}/v_{th,e} = 3$), i.e. a difference by a factor of 13.5 between the models. That is why comparison of simulations with these two models to experimental data is performed later, in order to see whether stochastization leads to a moderate or strong increase of the radial heat transport.

The model of Samain, Capes, Ghendrih and Nguyen [53] has some similarities with the models of sections 2.3.1 and 2.3.2. Heat and particle transport are envisaged as a sequence of steps with transport alternately perpendicular and parallel to the field lines as in the model developed here. However, the radial diffusion coefficient κ_r obtained has the form of (2.36), with

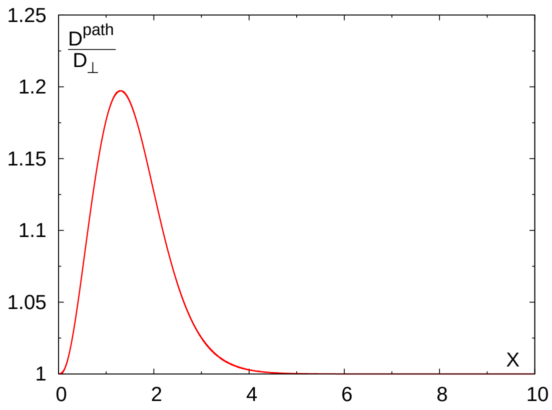

Figure 2.11: Particle diffusion along a path according to equation (2.31). The values of the parameters for these calculations are choosen for typical TEXTOR edge conditions, namely $D_{Fl} = 10^{-5}\ m$, $L_K = 50m$, $m_i = 2m_p$, $T_e = T_i = 150\ eV$, $D_\perp = \mu_\perp = 0.5\ m^2/s$ and $V_\perp = 0\ m/s$, which corresponds to $\zeta_n = 11.45$.

$L_{c,\delta} = L_K \ln(\sqrt{\zeta_T})$. Consequently, for $\zeta_T \ll 1$, the radial heat conductivity does not tend to $\kappa_\perp$, in the contrary of the smooth transition to $\kappa_\perp$ obtained in section 2.3.1. But the authors add the condition that $\kappa_r = \kappa_\perp$ for $\zeta_T \ll 1$. These differences are due to the different assumptions for the temperature differences along the segments of a path: in reference [53], the temperature differences along the perpendicular (between A and B in fig. 2.8) and parallel (between B and C) segments of the path are taken to be equal, while in section 2.3.1, they are computed from the heat balance equation.

Finally, the model of Kadomtsev and Pogutse [32] provides a radial heat conductivity close to the one obtained by Samain *et al.* for $\zeta_T \gg 1$, but additionally gives the scaling $\kappa_r \sim \sqrt{\kappa_\perp \kappa_\parallel}$ for $\zeta_T \lesssim 1$. The last scaling is close to the one obtained in section 2.3.1, as can be seen in fig. 2.10.

Till now, the value of the intrinsic perpendicular transport coefficients, i.e. the heat conductivity $\kappa_\perp$, the particle diffusivity $D_\perp$ and the viscosity $\mu_\perp$, have not been discussed. A model for these quantities is developed in the next chapter. The value of $V_\perp$ is then discussed in chapter 4.

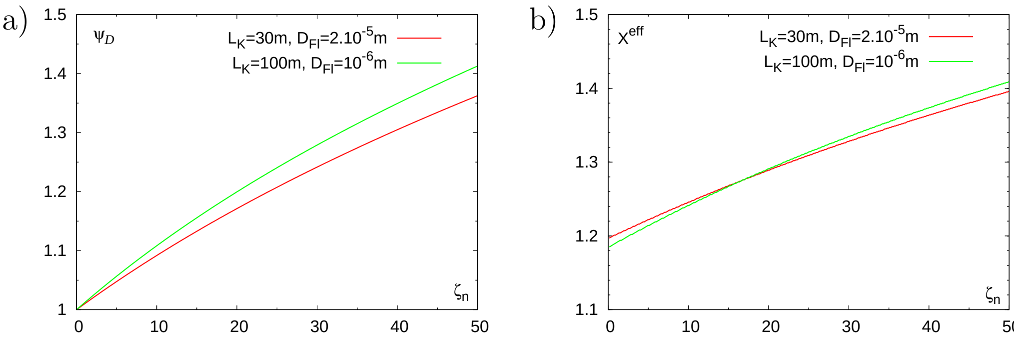

Figure 2.12: a) $\psi_D = D^{eff}/D_\perp$ as a function of the parameter ζ_n, with two different values for D_{Fl} and L_K. b) X^{eff}, i.e. X for which D^{path} is maximum, for the same values of D_{Fl} and L_K.

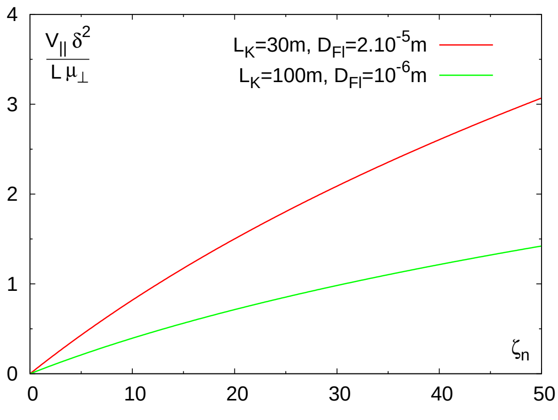

Figure 2.13: Ratio of the terms $m_i n V_\| \nabla_\| V_\|$ and $\nabla_\perp(m_i n \mu_\perp \nabla_\perp V_\|)$ as a function of ζ_n, with the same assumptions as in fig. 2.12.

Chapter 3

Model for anomalous perpendicular transport

In inhomogeneous magnetized plasmas, the observed transport is much larger than one would expect due to collisions. It is generally admitted that the additional transport, the so-called *anomalous transport*, results from the destabilization of low frequency modes, "low" meaning here much lower than the ion cyclotron frequency. These modes have a wavelength comparable to the ion Larmor radius[1] and are called micro-instabilities. In the following, a subset of the micro-instabilities is considered, namely the *drift instabilities*.

Section 3.1 presents the basis of the models commonly used for the study of micro-instabilities, i.e. plasma fluid equations and the drift ordering. In section 3.2, transport coefficients from the literature obtained on the base of fluid models are introduced. Each of these models considers only one type of micro-instability, and do not take into account the interactions between the different unstable modes. Therefore, a model combining different types of micro-instabilities has been developped for edge transport and is presented in section 3.3. It allows to investigate some effects of the stochastic field on anomalous transport by introduction of averaged values for quantities introduced in the previous chapter.

3.1 Plasma fluid equations

3.1.1 The plasma fluid equations

A plasma is a quasi-neutral mixture of electrons and ions. The ion species of interest for a fusion plasma are deuterium and tritium, but in present

[1] The term *Larmor radius* refers to the gyration radius of particles around field lines.

tokamaks, most experiments are performed with deuterium only (or hydrogen in some cases). Due to erosion of plasma facing components, impurity ions also enter the plasma, but their concentration generally lies under the percent (except for experiences where they are puffed on purpose). Therefore, it will be assumed that only the main ion species is of importance in the analysis of anomalous transport. The properties of the two plasma components, i.e. ions and electrons, are described by a distribution function $f_s(\boldsymbol{r}, \boldsymbol{v}, t)$, giving the particle density of the species s at the position $(\boldsymbol{r}, \boldsymbol{v})$ in the phase space, at time t. Henceforth, $s = i$ is adopted for ions, and $s = e$ for electrons.

A macroscopic (fluid) description of the plasma can be obtained by integration of f_e and f_i, and their various moments with respect to $\boldsymbol{v}$, over the velocity space (see e.g. [5]). The zeroth moment yields the density

$$n_s = \int f_s d^3\boldsymbol{v}, \tag{3.1}$$

the first moment gives the mean velocity

$$\boldsymbol{V}_s = \frac{1}{n_s} \int \boldsymbol{v} f_s d^3\boldsymbol{v}, \tag{3.2}$$

the second moment leads to the pressure tensor

$$\overleftrightarrow{\boldsymbol{P}}_s = m_s \int (\boldsymbol{v} - \boldsymbol{V}_s)(\boldsymbol{v} - \boldsymbol{V}_s) f_s d^3\boldsymbol{v}, \tag{3.3}$$

and the third moment provides the heat flux density

$$\boldsymbol{q}_{H,s} = \frac{m_s}{2} \int (\boldsymbol{v} - \boldsymbol{V}_s)(\boldsymbol{v} - \boldsymbol{V}_s)(\boldsymbol{v} - \boldsymbol{V}_s) f_s d^3\boldsymbol{v} \tag{3.4}$$

with m_s the particle mass. In the following, the pressure tensor is written in the form $\overleftrightarrow{\boldsymbol{P}}_s = p_s + \overleftrightarrow{\boldsymbol{\pi}}_s$, where p_s is the scalar pressure and $\overleftrightarrow{\boldsymbol{\pi}}_s$ is the stress tensor, with a zero trace. The temperature[2] T_s of each species is defined by $T_s = p_s/n_s$.

The time variation of f_s is given by the kinetic equation:

$$\frac{\partial f_s}{\partial t} + \boldsymbol{v}\frac{\partial f_s}{\partial \boldsymbol{r}} + \frac{\boldsymbol{F}}{m_s}\frac{\partial f_s}{\partial \boldsymbol{v}} = C_s. \tag{3.5}$$

The term $C_s(\boldsymbol{r}, \boldsymbol{v}, t)$ accounts for sources and sinks of particles (mainly ionization and recombination), and collisions with other species. $\boldsymbol{F}(\boldsymbol{r}, \boldsymbol{v}, t)$ is

[2]The temperature defined here has an energy dimension. This is because k_B, the Boltzmann constant, was included in T_s. If the definition $p_s = k_B n_s T_s$ was used instead, the temperature would have the usual dimension.

the *external* force acting on particles located at the point $(\boldsymbol{r}, \boldsymbol{v})$ at time t, i.e. $\boldsymbol{F}$ does not include collisions. An integration of the kinetic equation (3.5) over the velocity space leads to the *density continuity equation*:

$$\frac{\partial n_s}{\partial t} + \boldsymbol{\nabla} \cdot (n_s \boldsymbol{V}_s) = S_s, \tag{3.6}$$

where $S_s(\boldsymbol{r}, t)$ contains the sources and sinks of particles due to ionization and recombination. The $m_s \boldsymbol{v}$ moment of equation (3.5) gives the momentum equation, also known as the fluid *equation of motion*:

$$m_s n_s \left(\frac{\partial \boldsymbol{V}_s}{\partial t} + \boldsymbol{V}_s \cdot \boldsymbol{\nabla} \boldsymbol{V}_s \right) = n_s Q_s \left(\boldsymbol{E} + \boldsymbol{V}_s \times \boldsymbol{B} \right) - \boldsymbol{\nabla} \cdot \boldsymbol{P}_s + \boldsymbol{R}_s \tag{3.7}$$

where the force $\boldsymbol{F}$ on the particles is the electromagnetic force, $\boldsymbol{E}$ is the electric field, $\boldsymbol{R}_s$ is the force arising due to collisions with other species and Q_s is the particle charge. The $m_s v^2$ moment of equation (3.5) leads to the *heat balance equation*:

$$\frac{3}{2} \frac{\partial p_s}{\partial t} + \boldsymbol{\nabla} \cdot \left(\frac{3}{2} p_s \boldsymbol{V}_s \right) + p_s \boldsymbol{\nabla} \cdot \boldsymbol{V}_s + \pi_{jk} \frac{\partial V_{s,j}}{\partial x_k} + \boldsymbol{\nabla} \cdot \boldsymbol{q}_{H,s} = Q_{H,s} \tag{3.8}$$

where $Q_H = 1/2 \int mv^2 \, C_s d\boldsymbol{v}$ is the heat generated in a gas of particles of species s by collisions with particles of other species. The indices j and k correspond to the three coordinates of the real space, and a sum is performed over redundant indices. One can see from the above procedure that the equation describing the time variation of the zeroth moment of f_s, i.e. n_s, introduces the first moment $\boldsymbol{V}_s$ of f_s. In turn, the equation for the time variation of $\boldsymbol{V}_s$ introduces the second moment, $\boldsymbol{P}_s$. In the equation for the time variation of $\boldsymbol{P}_s$ (actually p_s), the third moment of f_s appears, and so on. This provides an exact treatment of the problem, but one would have to handle an infinite set of equations with this method. To get a finite, closed set of equations, an assumption will be made for $\boldsymbol{\nabla} p_s$, but the discussion of this point is postponed to section 3.3.

A plasma is quasi-neutral [8] over distances larger than the Debye length λ_D for frequencies significantly lower than the electron plasma frequency[3] ω_{pe}. For typical edge TEXTOR conditions ($n_e \approx 10^{19}\ m^{-3}$, $T_{i,e} \approx 150\ eV$), $\lambda_D \approx 2.9 \cdot 10^{-5}\ m$, i.e. it is much smaller than all macroscopic lengths of the tokamak, and $\omega_{pe} \approx 1.8 \cdot 10^{11}\ s^{-1}$, i.e. much larger than $1/\tau$ for all characteristic times τ over which the macroscopic parameters of the plasma can vary. Therefore, the assumption of *quasi-neutrality* is made:

$$n_e \approx n_i \approx n \tag{3.9}$$

[3] In the fusion community, the term "frequency" is often used to designate the pulsation, and this denomination will be used henceforth.

where it is assumed that ion species are deuterons with a charge equal to the elementary charge e.

3.1.2 Basic mechanism of a drift wave

With the purpose of introducing the drift ordering and facilitating comprehension of section 3.3, the basic mechanism for drift waves and drift resistive instabilities is now explained. Small perturbations $\widetilde{n}$ and $\widetilde{\phi}$ of respectively the density and the electrostatic potential are considered in the form $\widetilde{x} = X \exp(-i\omega t + ik_y y + ik_z z)$, which will be justified in section 3.3. X is the amplitude of the perturbation and ω is its complex frequency. k_z is the wave number in the direction z along the magnetic field and k_y is the wave number in the direction y, which is the direction perpendicular to the magnetic field, on the surface of radius r comprising the considered point. The time evolution of the density and potential perturbations is described by the fluid equations introduced in the previous section, in which only the terms linear in the perturbations $\widetilde{n}$ and $\widetilde{\phi}$ are kept. Two assumptions, discussed in section 3.3, are used: the quasi-neutrality approximation, i.e. $\widetilde{n}_e \approx \widetilde{n}_i \approx \widetilde{n}$, and $\boldsymbol{\nabla}\widetilde{p}_e \approx T_e \boldsymbol{\nabla}\widetilde{n}$, corresponding to isothermal electrons.

In the following, all frequencies ω and lengths l satisfy $\omega \ll \omega_{c,s}$ and $l \gg \rho_s$ for all species, with $\omega_{c,s}$ and ρ_s the cyclotron frequency and Larmor radius of the species s (these relations are verified in section 3.3.5). In this case, as already mentioned in chapter 2, the motion of particles can be described by the motion of their gyration center. This was actually already done in section 3.1.1 by integrating the different moments of f_s over the velocity space. In this context, the motion of particles perpendicular to the magnetic field is described by "drifts", due to different forces acting on the particles (see e.g. ref. [8]). For simplification, it is assumed in this section that the only force giving rise to a drift is the force due to the electric field perturbation (note that the pressure perturbation also produces a drift, but as it will be seen below it is much smaller than the one due to the electric field perturbation). It leads to the so-called $\boldsymbol{E} \times \boldsymbol{B}$ drift, $\widetilde{\boldsymbol{V}}_E = (\boldsymbol{B} \times \boldsymbol{\nabla}\widetilde{\phi})/B^2$. By introducing this drift into the ion density continuity equation (3.6) and neglecting the parallel gradient of the parallel velocity, one has:

$$-i\omega\widetilde{n} - i\frac{k_y}{B}\widetilde{\phi}\nabla_r n_0 = 0 \tag{3.10}$$

where the source S has been assumed to be constant both in time and space. The parallel component of the electron motion equation, equation (3.7), gives:

$$0 = ik_z en\widetilde{\phi} - ik_z T_e \nabla_\parallel \widetilde{n} + \widetilde{R}_{ei,\parallel}, \tag{3.11}$$

where inertia terms have been neglected due to the smallness of the electron mass. In a first stage, the interaction term with ions, $\widetilde{R}_{ei,\|}$, is neglected in order to describe a pure drift wave. Some quantities are introduced so as to facilitate the interpretation of the equations: $v_{th,i} = \sqrt{T_i/m_i}$, $\omega_{ci} = eB/m_i$ is the ion cyclotron frequency, $\rho_i = v_{th,i}/\omega_{ci}$ is the ion Larmor radius, $L_n = |\nabla_r \ln n_0|^{-1}$ is the perpendicular e-folding length of the background density n_0, $\alpha = T_e/T_i$, and $\omega_0 = v_{th,i}/L_n$. Combination of equations (3.10) and (3.11) leads to the dispersion relation of a pure drift wave:

$$\frac{\omega}{\omega_0} = \alpha k_y \rho_i. \tag{3.12}$$

As it will be seen in section 3.3.3, $k_y\rho_i \sim 0.1$ for drift modes at the plasma edge, such that $\omega \approx 0.1\,\omega_0$ for their characteristic frequency. For the typical TEXTOR edge parameters $T_e = T_i = 150\,eV$ and $L_n = 5\,cm$, one gets $\omega \approx 1.7 \cdot 10^5\,s^{-1}$.

The physical mechanism of the drift wave described above is the following: electrons are free to move along the magnetic field, such that their distribution leads to a balance between the pressure and electric forces, as one can see from equation (3.11) (with $\widetilde{R}_{ei,\|} = 0$). On the contrary, the motion of particles perpendicular to the magnetic field is not free and occurs only through drifts (in the present case through the $\boldsymbol{E} \times \boldsymbol{B}$ drift). Consider now a particular position. Because of the background[4] radial density gradient, the radial component of the $\boldsymbol{E} \times \boldsymbol{B}$ drift brings plasma with a higher or lower density at this position, depending on the direction of the drift. The density perturbation changes thus in time due to drifts, and so does the electric potential perturbation because the motion of electrons along $\boldsymbol{B}$ balances the pressure and electric forces. Alternatively, one can consider the isobar and isopotential surfaces. Without perturbations, they coincide with magnetic surfaces, while in presence of perturbations, they exhibit small oscillations on both sides of magnetic surfaces, and these oscillations propagates. Note that the amplitude of the perturbations is constant in time. This can be seen by noticing that the drift velocity is zero at the positions where the density perturbation reaches one of its extrema, as is illustrated in fig. 3.1.

By neglecting ion-electron collisions, equations (3.10) and (3.11) describe a mode with an amplitude constant in time, for which perturbations of density and electrostatic potential are in phase, i.e. $\hat{n} = \hat{\phi}$, with $\hat{n} = \widetilde{n}/n$ and $\hat{\phi} = e\widetilde{\phi}/T_e$ the dimensionless perturbations. If some mechanism leads to a phase shift between the perturbations, ω becomes complex: $\omega = \omega_r + i\gamma$, with

[4] In the following, the term *background* refers to the unpertubed part of the different quantities considered.

ω_r being the real frequency of the wave and γ its growth rate. For $\gamma > 0$, the mode is unstable. Resistivity for instance can provide such a destabilizing mechanism, in which case the unstable mode is called a *drift resistive mode*. Taking now the resistive part of $\widetilde{R}_{ei,\parallel}$ into account in equation (3.11), one obtains[5] a relation of the form $\hat{\phi} = (1 + i\delta)\hat{n}$, with δ being real and proportional to resistivity. The frequency of the mode is then $\omega = (1 + i\delta)\omega_0\, k_y\rho_i$, and the growth of the mode is $\gamma = \delta\omega_0 k_y\rho_i$.

In figure 3.1.b, one can see that with friction the radial drift velocity does not vanish at the positions where the density perturbation reaches its extrema. From the relative position of density and radial drift perturbations, one can see that the amplitude of the density perturbation grows with time (and consequently so does the potential perturbation), such that the mode is unstable. A futher consequence of the fact that density and radial drift perturbations are not out of phase by exactly 90° is a net flux of particle directed towards regions of lower density: this is a source of anomalous diffusion.

3.2 Anomalous perpendicular transport coefficients from the literature

On the base of the fluid model described above, several expressions for anomalous perpendicular transport coefficients are proposed in the literature. These models sometimes include kinetic corrections or equations for higher momenta of the distribution function f_s. Some of the expressions for anomalous transport coefficients obtained with the models for the unstable modes assumed to bring the largest contribution to transport are briefly presented and will be used in the following. These models can be separated between models for core transport and models for edge transport. The former group includes toroidal Ion Temperature Gradient (ITG) modes and Trapped Electrons (TE) modes while the latter contains Drift-Alfvèn (DA) and Drift Resistive Ballooning (DRB) modes.

Toroidal ion temperature gradient modes

These modes arise due to the toroidal geometry of the tokamak, which is responsible for a non-zero flux divergence in the continuity equation (3.6). They are destabilized when the ion temperature gradient exceeds a critical level, or more precisely when the ratio $\eta_i = L_n/L_{T_i}$ exceeds a critical value, with $L_{T_i} = |\nabla_r \ln T_i|^{-1}$ the e-folding length of the ion temperature.

[5] Details of calculation are left to section 3.3 with a more complicated case.

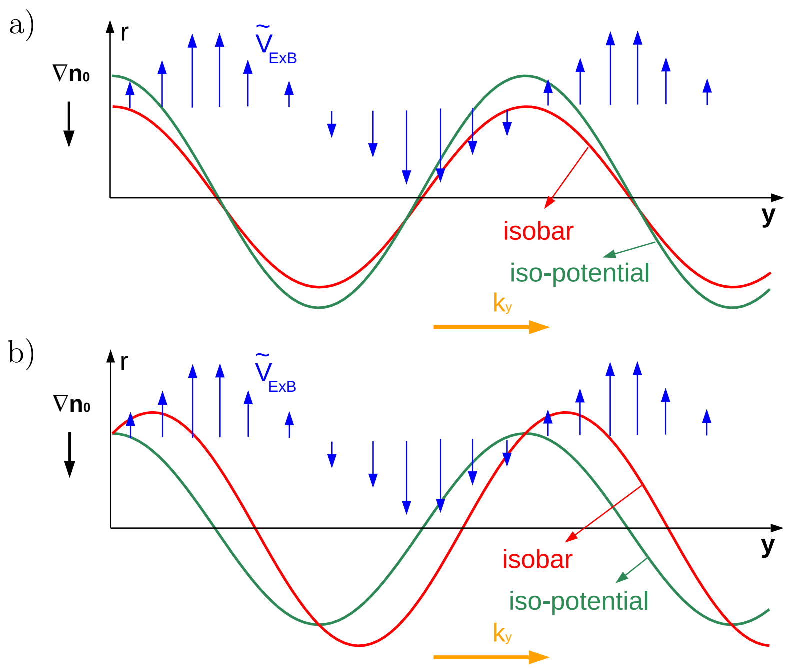

Figure 3.1: Isobar (or iso-density) and iso-potential perturbed curves corresponding to a drift mode in the (r, y) plane. a) Density and potential perturbations are in phase, and the perturbation $\boldsymbol{E} \times \boldsymbol{B}$ drift is disphased by 90° with respect to the density perturbation. The isobar and iso-potential curves move in time to the right, and keep a constant amplitude. b) There is a slight phase difference between density and potential perturbations, such that the phase difference between density and $\boldsymbol{E} \times \boldsymbol{B}$ drift perturbations is not exactly 90°. From the relative position of the density perturbation and the $\boldsymbol{E} \times \boldsymbol{B}$ drift, one sees that the amplitude of the density perturbation grows with time, and so does the potential perturbation: the mode is unstable.

The transport contribution from unstable ITG modes is computed using the results of reference [65] in the limit of a perpendicular wave length of the perturbations much larger than the ion Larmor radius:

$$D_{\perp}^{ITG} = \frac{T_e}{eBk_{ITG}} \left[\left(\frac{1}{L_{T_i}} - \frac{2}{3L_n} \right) \frac{2\tau}{R} - \frac{1}{4} \left(\frac{2}{R} - \frac{1}{L_n} \right)^2 - \frac{40}{9} \frac{\tau^2}{R^2} \right]^{1/2} \quad (3.13)$$

where $\tau = T_i/(T_e Z_{eff})$ and Z_{eff} is the effective plasma charge, assumed to be one in the following. The characteristic perpendicular wave vector of the most unstable ITG modes is of the order $k_{ITG} \approx 0.3/\rho_s$ [65], where $\rho_s = \tau^{-1/2}\rho_i$, $\rho_i = v_{t,i}/\omega_{ci}$ is the ion Larmor radius, and $v_{t,i} = \sqrt{T_i/m_i}$ and $\omega_{ci} = Z_{eff}eB/m_i$ are the thermal velocity and cyclotron frequency of ions.

Trapped electron modes

Adiabatic invariants [67] are quantities associated with the motion of charged particles. They are constant during changes of the motion if the variations of other quantities are much slower than the cyclotron frequency and much larger than the Larmor radius of these particles. One of these adiabatic invariants is the magnetic moment $\mu = m_s u_{\perp}/(2B)$ of a particle, with $u_{\perp}$ the perpendicular velocity of the particle (not of its gyration center). Consider a region where the collision frequency is low enough such that the total energy of the particle is conserved over one poloidal turn (of its gyration center) in the tokamak. As already mentioned in chapter 2, the amplitude of the magnetic field decays from the tokamak axis as $1/R$. Since μ and the total square velocity u^2 are constant for a particle, there are particles on the low field side of the tokamak which will have transfered all their kinetic energy into their perpendicular motion $u_{\perp}$ before they reach the high field side. These particles will be reflected (they gyration center will move back) before they complete a poloidal turn in the tokamak, i.e. they are *trapped* on the low field side of the tokamak. The fraction f_{tr} of trapped particles at radius r in absence of collisions is [67] $f_{tr} = \sqrt{2r/(R_* + r)}$. Particles can actually be trapped only in regions where the collision time is larger than the time between two reflexions, i.e. where temperature is large enough. That is why TE modes can be expected in the plasma core, but not at the edge.

A consequence of electron trapping is a reduction of the electron mobility along the magnetic field, which in turn reduces their ability to cancel spatial charge separation. It can result in an instability, whose growth rate is then proportional to f_{tr}. The corresponding particle diffusion coefficient is assumed in the form:

$$D_\perp^{TE} = \frac{f_{tr}\eta_e}{k_{TE}^2}\frac{\omega_*^2\nu_{eff}}{\omega_*^2+\nu_{eff}^2} \tag{3.14}$$

with $\eta_e = L_n/L_{T_e}$, $L_{T_e} = |\nabla_r \ln T_e|^{-1}$ the e-folding length of the electron temperature, $k_{TE} \approx 1/\rho_i$ the perpendicular wave length of the mode, $\omega_* = T_e k_{TE}/(eBL_n)$ the electron drift frequency, $\nu_{eff} = \nu_e R/r$ and ν_e the electron-ion collision frequency. This expression reproduces both the cases of low collisionality of reference [43] and high collisionality of reference [42].

Drift resistive ballooning modes

As indicated by their name, DRB unstable modes are triggered by resistivity. The amplitude of the perturbations related to these modes, as well as the corresponding transport, exhibits a particular shape: it is larger on the Low Field Side (LFS) of the tokamak (outer side) than on the High Field Side (HFS, inner side). By analogy with a balloon which expands when it is pumped up, these modes are said to have a *ballooning character* since they tend to grow on the outer side of the tokamak.

In order to understand the origin of this character, it is necessary to precise how equation (3.11) can be solved. A qualitative description is given here, the analytical treatment being presented in section 3.3.2. According to ref. [5], the resistive part of $\widetilde{R}_{ei,\parallel}$ is $\widetilde{R}_{ei,\parallel}^{res} = 0.51\, m_e\nu_e\widetilde{j}_\parallel/e$. By applying the operator $\nabla_\parallel$ on equation (3.11), one can determine the resitive term with the help of the quasi-neutrality condition $\nabla_\parallel\widetilde{j}_\parallel = -\boldsymbol{\nabla}_\perp\widetilde{\boldsymbol{j}}_\perp$ (see equation (3.41)). Since the magnetic field depends on the poloidal angle θ and since the perturbed perpendicular current $\widetilde{\boldsymbol{j}}_\perp$ is proportional to $1/B$, $\nabla_\parallel\widetilde{j}_\parallel$ depends on θ. A quantitative treatment shows that the poloidal dependence of B leads to an increase of the resistive term on the LFS of the tokamak and to a decrease of the latter on the HFS. Thus, the poloidal dependence of the magnetic field makes the mode more unstable on the LFS and more stable on the HFS, such that the unstability exhibits a ballooning character.

The particle diffusion coefficient for DRB instabilities is taken from reference [23]:

$$D_\perp^{DRB} = (q\rho_e)^2\,\nu_e\frac{R}{L_n} \tag{3.15}$$

where $\rho_e = \sqrt{m_e T_e}/(eB)$ is the ion Larmor radius. Note that although the unstability depends on the poloidal angle, expression (3.15) does not. This is because $D_\perp^{DRB}(\theta)$ has been averaged on the poloidal angle. All transport coefficients obtained in the following are averaged on the poloidal angle in order to introduce them in a one dimensional transport code.

Drift-Alfvèn modes

DA modes are drift modes combined with electromagnetic fluctuations. As DRB instabilities, DA instabilities are triggered by resistive effects. To describe the anomalous transport to which they give rise, the model of references [11, 37] can be used:

$$D_{\perp}^{DA} = \frac{\chi_{GB}}{\sqrt{\mu_a}} f(\beta_n, \nu_n) \tag{3.16}$$

where $\chi_{GB} = \rho_s^2 \tau^{-1/2} v_{t,i}/L_{p_e}$, $L_{p_e} = |\nabla_r \ln p_e|^{-1}$ is the e-folding length of the electron pressure and $\mu_a = k_{\parallel} L_{p_e} \sqrt{m_i/m_e}$, with $k_{\parallel} \approx 1/(qR)$ the parallel component of the mode wave vector. The function $f(\beta_n, \nu_n)$ and its parameters are defined as follows:

$$\begin{gathered} f(\beta_n, \nu_n) = \sqrt{\frac{(1+\beta_n^2)^{-3} + \nu_n^2}{1 + \beta_n^2 + \nu_n^{4/3}}} \\ \beta_n = \sqrt{\frac{m_i}{m_e}} \frac{\beta}{k_{\parallel} L_{p_e}}, \qquad \nu_n = \left(\frac{m_i}{m_e}\right)^{1/4} \frac{1}{\lambda_{th,e}} \sqrt{\frac{L_{p_e}}{k_{\parallel}}} \end{gathered} \tag{3.17}$$

with $\beta = \mu_0 n_e T_e / B^2$.

The perpendicular anomalous viscosity coefficient $\mu_{\perp}$ and heat conductivity $\kappa_{\perp}$ are not defined in the previous models, except for $\kappa_{\perp}$ in the case of DA modes. For the anomalous viscosity, the approximation $\mu_{\perp} \approx D_{\perp}$ is made henceforth, as will be argued in section 3.3.4. Concerning heat conductivity, the assumption $\kappa_{\perp} = 3/2\, n D_{\perp}$ is made, as obtained in references [11, 37] for DA instabilities.

3.3 Model developed for anomalous transport coefficients

The aim of this section is the development of a model for anomalous transport due to edge instabilities. It is not intended to obtain an advanced model, which could be the subject of a thesis on its own, but well to get a relatively simple model, combining DA, Drift Resistive (DR) and DRB instabilities. Additionally, some effects of the stochastic magnetic field on anomalous transport are investigated.

This section is structured as follows: in section 3.3.1, the drift ordering and the geometry of the model are presented. In section 3.3.2, the fluid equations obtained in section 3.1 are used to describe small pertubations of different plasma quantities. These perturbations are represented in terms of Fourier modes, and equations are linearized with respect to the perturbations. Then, in section 3.3.3, a dispersion relation for each Fourier mode is obtained. The perturbation saturation level necessary to predict anomalous transport is estimated in section 3.3.4 on the base of a quasi-linear approximation. Under the assumption that the mode with the largest growth rate will dominate, the time averaged transport due to this mode is calculated, and transport coefficients are obtained. Finally, the validity of the model is discussed in section 3.3.5.

3.3.1 Drift ordering and geometry of the model

As explained in section 3.1.2, drift modes are distabilized if some effect introduces a phase shift between the density and potential perturbations. It will be seen in section (3.3.2) that the resistive term $\widetilde{R}^{res}_{ei,\|}$ in equation (3.11), which produces such a phase shift, can be expressed as a function of $\nabla_\perp \widetilde{n}$ and $\nabla_\perp \widetilde{\phi}$. It is thus proportional to $k_\perp \widetilde{n}$ and $k_\perp \widetilde{\phi}$, with $k_\perp$ the wave number in the perpendicular direction. The two other terms in this equation, namely $\nabla_\| \hat{n}$ and $\nabla_\| \widetilde{\phi}$, are proportional to $k_\| \widetilde{n}$ and $k_\| \widetilde{\phi}$, with $k_\|$ the wave number along the magnetic field. Hence, the larger the ratio $k_\perp / k_\|$, the larger the effect of resistivity, and the larger the instability. The most unstable modes have thus a wave vector almost perpendicular to the magnetic field, and the ordering $k_\| \ll k_\perp$ is used henceforth.

Since the modes are almost aligned with the magnetic field, it is interesting to work in the base ($\boldsymbol{e}_r$, $\boldsymbol{e}_y$, $\boldsymbol{e}_\|$) aligned on the magnetic field. It is related to the base ($\boldsymbol{e}_r$, $\boldsymbol{e}_\theta$, $\boldsymbol{e}_\varphi$) through the following relations:

$$\begin{aligned} \boldsymbol{e}_\| &= \frac{B_\theta}{B}\boldsymbol{e}_\theta + \frac{B_\varphi}{B}\boldsymbol{e}_\varphi \\ \boldsymbol{e}_y &= \frac{B_\varphi}{B}\boldsymbol{e}_\theta - \frac{B_\theta}{B}\boldsymbol{e}_\varphi \end{aligned} \quad \Longleftrightarrow \quad \begin{aligned} \boldsymbol{e}_\theta &= \frac{B_\varphi}{B}\boldsymbol{e}_y + \frac{B_\theta}{B}\boldsymbol{e}_\| \\ \boldsymbol{e}_\varphi &= -\frac{B_\theta}{B}\boldsymbol{e}_y + \frac{B_\varphi}{B}\boldsymbol{e}_\|, \end{aligned} \tag{3.18}$$

where $\boldsymbol{e}_r$, $\boldsymbol{e}_\theta$ and $\boldsymbol{e}_\varphi$ are the unit vectors respectively along the radial, poloidal and toroidal directions, $\boldsymbol{e}_\|$ is the unit vector along the magnetic field and $\boldsymbol{e}_y = \boldsymbol{e}_\| \times \boldsymbol{e}_r$, i.e. the direction y is the direction on unperturbed magnetic surfaces, perpendicular to the magnetic field, see fig. 3.2.

For the following, the expression of the $\boldsymbol{\nabla}$ operator in the base ($\boldsymbol{e}_r$, $\boldsymbol{e}_y$, $\boldsymbol{e}_\|$) has to be found. In order to do this, it is usefull to introduce the dependences

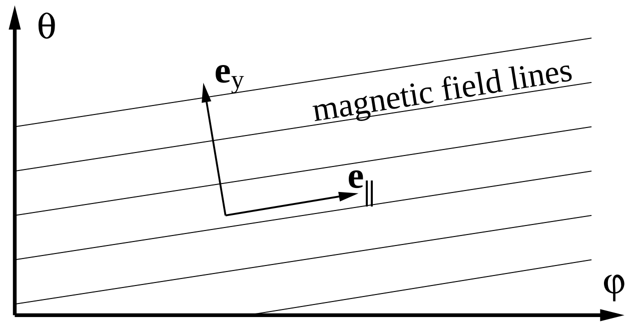

Figure 3.2: Relative orientation of the ($\boldsymbol{e}_r$, $\boldsymbol{e}_y$, $\boldsymbol{e}_\parallel$) and ($\boldsymbol{e}_r$, $\boldsymbol{e}_\theta$, $\boldsymbol{e}_\varphi$) bases. The vector $\boldsymbol{e}_r$ is perpendicular to the (θ, φ) plane.

of the pertubations and of the backgroung magnetic field on the different coordinates. The magnetic field is first considered. It is almost constant in the toroidal direction, but it varies along the poloidal and radial directions. Though small, these poloidal and radial dependences are of importance for the DRB instability. They can be found from the $\boldsymbol{\nabla} \times \boldsymbol{B} = \boldsymbol{0}$ Maxwell's equation (where the plasma current is neglected, since its effect on B_φ is very small, see chapter 5):

$$B_\varphi(r,\theta) = B_* \frac{R_*}{R(r,\theta)} = B_* \frac{R_*}{R_*(1+\frac{r}{R_*}\cos\theta)} \approx B_* \left(1 - \frac{r}{R_*}\cos\theta\right), \quad (3.19)$$

where B_* is the amplitude of the magnetic field on the plasma axis, and $r/R_* \ll 1$ has been taken into account. The poloidal magnetic field is given by equation (2.2), such that the total unperturbed field is

$$\boldsymbol{B} = B_\varphi \boldsymbol{e}_\varphi + B_\theta \boldsymbol{e}_\theta, \qquad B = B_\varphi \sqrt{1 + \left(\frac{r}{qR}\right)^2} \approx B_\varphi \quad (3.20)$$

with $q \approx 3$ at the edge. The pertubations are decomposed into Fourier modes, by assuming them in the form

$$\widetilde{x} = X(l)\exp(-i\omega t + ik_y y + ik_r r), \quad (3.21)$$

where l is the coordinate along the magnetic field. Since non-linear terms are not taken into account, the different Fourier harmonics are not coupled and can be considered separately. ω is the complex frequency of the mode, and k_y its wave number in the y direction. The perturbations are not periodic in the radial direction, and an exact calculation of the modes should include their radial structure (see e.g. [50]). This is out of the scope of this thesis, such that the radial dependence of the modes is assumed in the form of (3.21). The modes are assumed to be isotropic in the perpendicular direction, i.e. $k_r \approx k_y = k_\perp$. Note that if kinetic effects are taken into account, the radial extend of the mode is seen to be limited to a width $w \approx \rho_i Rq/(\hat{s}L_n)$ by the so-called Landau damping [65]. Since $w \gg k_r^{-1}$ the assumption $k_r \approx k_y$ is not in contradiction with Landau damping. Finally, $X(l)$ is the complex amplitude of the perturbation and varies smoothly along the magnetic field, due to the poloidal variation of the latter. Perturbations are thus assumed to be periodic in time and in the radial and y directions, with an amplitude varying slightly along the magnetic field.

Expressions for the perturbation derivatives can now be precised. From equation (3.21), one has $\partial/\partial t = -i\omega$, $\nabla_y = ik_y$ and $\nabla_r = ik_r$. It remains to find an expression for $\nabla_\parallel$. For this purpose, a general property [50] of drift modes is used: they have large poloidal (M) and toroidal (N) mode numbers. This means that in the ($\boldsymbol{e}_r$, $\boldsymbol{e}_\theta$, $\boldsymbol{e}_\varphi$) base, they can be represented by $X(\theta)Y(\omega,r)e^{iM\theta+iN\varphi}$, with large M and N, and where the correspondence between $X(l)$ and $X(\theta)$ can be found from the relation $\partial l = qR\partial\theta$. Their poloidal and toroidal derivatives read:

$$\begin{aligned}\nabla_\theta\Big(X(\theta)Y(\omega,r)e^{iM\theta+iN\varphi}\Big) &= \left(i\frac{M}{r}X(\theta)+\frac{1}{r}\frac{\partial X(\theta)}{\partial\theta}\right)Y(\omega,r)e^{iM\theta+iN\varphi}\\ \nabla_\varphi\Big(X(\theta)Y(\omega,r)e^{iM\theta+iN\varphi}\Big) &= i\frac{N}{R}X(\theta)Y(\omega,r)e^{iM\theta+iN\varphi}\end{aligned} \tag{3.22}$$

By using relations (3.18), one obtains the expressions of $\nabla_\parallel$ and ∇_y:

$$\begin{aligned}\nabla_\parallel = \frac{\boldsymbol{B}\cdot\boldsymbol{\nabla}}{B} &= \boldsymbol{e}_\parallel\cdot\left(\boldsymbol{e}_r\nabla_r+\boldsymbol{e}_\theta\left(i\frac{M}{r}+\frac{1}{r}\frac{\partial}{\partial\theta}\right)+i\frac{N}{R}\boldsymbol{e}_\varphi\right)\\ &\approx \frac{1}{R}\left(iN+i\frac{M}{q}+\frac{1}{q}\frac{\partial}{\partial\theta}\right),\\ \nabla_y = \frac{\boldsymbol{e}_y\cdot\boldsymbol{\nabla}}{B} &\approx i\frac{M}{r}+\frac{1}{r}\frac{\partial}{\partial\theta}+i\frac{r}{qR}\frac{N}{R}\end{aligned} \tag{3.23}$$

It was seen above that the most unstable modes are characterized by a smallest possible parallel wave number. From equation (3.23), one sees that these modes develop close to rational magnetic surfaces chartacterized by $q = -M/N$ (note that q can be either positive or negative, depending on the relative directions of the magnetic field and the plasma current). Therefore

$$\nabla_\parallel = \frac{\partial}{\partial l} = \frac{1}{qR}\frac{\partial}{\partial\theta} \tag{3.24}$$

is henceforth assumed. Since M is large, $(\partial X(\theta)/\partial\theta)/X(\theta) \ll M/r$, and one can see from equation (3.23) that ∇_y does not apply on $X(\theta)$. It is thus reasonable to write ∇_y in the form $\nabla_y = ik_y$.

It is stressed that the θ-dependence of X accounts only for the smooth poloidal dependence of the unperturbed magnetic field, and that it does not include the fast poloidal variations of the perturbations, the latter ones being described by the exponential factor in equation (3.21).

The derivatives obtained above have been calculated in the assumption of an unperturbed magnetic field. In a perturbed magnetic field, the parallel derivative of a perturbed quantity C becomes

$$\nabla_{\|}C = \frac{\boldsymbol{B}\cdot\boldsymbol{\nabla}}{B}C = \nabla_{\|}\widetilde{C} + \frac{\widetilde{B}_r}{B}\nabla_r C_0 + \frac{\widetilde{B}_y}{B}\nabla_y C_0 \tag{3.25}$$

where $\widetilde{C}$ is the pertubation of C, and C_0 its background value. Since background quantities depend on r only, the last term of equation (3.25) is zero. The perpendicular derivatives are also modified by the fluctuations of the magnetic field, and the corresponding change is detailed where necessary (see appendix D). However, only the magnetic field perturbations due to the parallel perturbation current $\widetilde{j}_{\|}$ are taken into account in the present model for anomalous transport, not the ones due to the DED[6].

In the following it will be assumed that the drift ordering is applicable. It implies an ordering of the different terms according to the derivatives they contain. The background plasma parameters f vary radially only, and their radial derivative can be written as $-f/L_{\perp}$, with $L_{\perp} = -dr/d\ln f$ being typically of the order of several *cm* at the plasma edge. As for the background magnetic field, its radial derivative is of the order of $1/R$, with $R \approx 1.75\,m$. The perpendicular derivative of perturbations is of the order $k_{\perp} \sim 0.1/\rho_i$, with $\rho_i \approx 1\,mm$ at TEXTOR edge, such that $k_{\perp} \approx 1\,cm^{-1}$. Their parallel derivative is of order $k_{\|} \approx 1/(qR)$. The ordering used henceforth is

$$\frac{\partial}{\partial l}, \frac{1}{R} \ll k_{\perp}, \frac{1}{L_{\perp}}, \qquad K_{\perp}^3 \ll 1, \qquad \frac{K_{\perp}}{L_{\perp}}, \frac{K_{\perp}}{R} \ll 1 \tag{3.26}$$

with $K_{\perp} = k_{\perp}\rho_s$. Finally, the time derivative produces terms of the order of $K_{\perp}$. This can be seen by combining equations (3.10) and (3.12) with $\hat{\phi} \approx \hat{n}$.

[6]The most convenient way to represent the perturbations induced on the magnetic field by the DED would be a sum of Fourier modes like in equation (2.6) (note that such a representation should also be used for the poloidal component of the DED perturbation). However, even taking a single of these modes into account would already lead to a considerable complication of the model. Therefore, such a task is left to 3D numerical modellings as the one of reference [49].

3.3.2 Basic equations of the model

The equations for perturbations of the density n, the parallel electric current $j_\parallel$, the electrostatic potential ϕ, and the magnetic field are derived in this section. Perturbed quantities are assumed in the form $x = x_0 + \widetilde{x}$, where x_0 denotes the unpertubed quantity, and $\widetilde{x}$ the perturbation. The introduction of $\widetilde{n}$ leads to two remarks. First, since all characteristic lengths for the variations of perturbations are much larger than the Debye length, and since $\omega \ll \omega_{pe}$, the assumption of quasi-neutrality (equation (3.9)) is also applicable for density perturbations, $\widetilde{n} = \widetilde{n}_e \approx \widetilde{n}_i$. Secondly, $\widetilde{n}_e \approx \widetilde{n}_i$ does not imply that $\boldsymbol{\nabla} \cdot \boldsymbol{E} = 0$. Though very small, the difference between $\widetilde{n}_e$ and $\widetilde{n}_i$ gives rise to a significant electric field [67], defined as

$$\boldsymbol{E} = -\boldsymbol{\nabla}\phi - \frac{\partial \boldsymbol{A}}{\partial t}, \tag{3.27}$$

where $\boldsymbol{A}$ is the electromagnetic vector potential. It is related to the magnetic field through $\boldsymbol{B} = \boldsymbol{\nabla} \times \boldsymbol{A}$, and governed by the Maxwell's equation:

$$\boldsymbol{\nabla} \times \boldsymbol{B} = \mu_0 \boldsymbol{j} + \frac{1}{c^2}\frac{\partial \boldsymbol{E}}{\partial t} \tag{3.28}$$

with μ_0 the permeability of free space, and c the speed of light in vacuum. In the following, the time derivative of the electric field is neglected since the modes studied in the present chapter propagate at a velocity much lower than that of light.

A first relation between $\widetilde{n}$ and $\widetilde{\phi}$ is obtained from the ion continuity equation (see equation (3.6))

$$\frac{\partial \widetilde{n}}{\partial t} + \boldsymbol{\nabla} \cdot \left(\widetilde{n\boldsymbol{V}_i}\right) = 0, \tag{3.29}$$

where S_i has been set to zero since time and space varitions of ion source terms are negligible. In the drift ordering, the perpendicular velocity, which results from drifts, is given by [65]

$$\boldsymbol{V}_\perp = \boldsymbol{V}_E + \boldsymbol{V}_* + \boldsymbol{V}_p + \boldsymbol{V}_\pi \tag{3.30}$$

with

$$\begin{aligned} \boldsymbol{V}_E &= \frac{\boldsymbol{B} \times \boldsymbol{\nabla}\phi}{B^2} \\ \boldsymbol{V}_* &= \frac{\boldsymbol{B} \times \boldsymbol{\nabla} p}{ZenB^2} \\ \boldsymbol{V}_p &= m\frac{\boldsymbol{B} \times \frac{d\boldsymbol{V}}{dt}}{ZeB^2} \\ \boldsymbol{V}_\pi &= \frac{\boldsymbol{B} \times (\boldsymbol{\nabla} \cdot \overleftrightarrow{\pi})}{ZenB^2} \end{aligned} \tag{3.31}$$

where $\boldsymbol{V}_E$ is the $\boldsymbol{E}\times\boldsymbol{B}$ drift, $\boldsymbol{V}_*$ is the diamagnetic drift, $\boldsymbol{V}_p$ is the polarization drift, $\boldsymbol{V}_\pi$ is a drift due to viscosity, and $d/dt = \partial/\partial t + \boldsymbol{V}\cdot\boldsymbol{\nabla}$. As already mentioned in section 3.1, it is assumed that $Z=1$ for ions ($Z=-1$ for electrons). In the fluid description of the plasma introduced in section 3.1, it was mentioned that a closure relation is needed for the pressure tensor divergence. In the following, this relation is obtained under the assumption that electrons and ions are isothermal, i.e. that $\widetilde{\boldsymbol{\nabla} p_{e,i}} = T_{e,i}\widetilde{\boldsymbol{\nabla} n}$, and this assumption is discussed in section 3.3.5. Contributions from electron and ion stress tensors are discussed in appendix D.

The divergence of the ion perpendicular perturbation flux is calculated in appendix D. The contribution from the ion parallel perturbation velocity is neglected due to the ordering $\partial/\partial l \ll k_\perp$ adopted (using the parallel component of the ion motion equation, one finds that $\widetilde{V}_{i,\parallel}$ is proportional to parallel derivatives of $\widetilde{n}$ and $\widetilde{\phi}$, interactions with electrons being negligible due to the small ratio m_e/m_i). However, it was seen in chapter 2 that $\partial V_{\parallel,st}/\partial l$ is always positive, where $V_{\parallel,st}$ is the parallel velocity resulting from the stochastic field. The averaged value of $\partial V_{\parallel,st}/\partial l$, henceforth written $\nu_\parallel$, is computed in appendix C. With equation (D.29) and the previous considerations, the ion continuity equation reads

$$0 = -i\omega\widetilde{n} + \frac{ik_y}{B}\left(\widetilde{n}\nabla_r\phi_0 - \widetilde{\phi}\nabla_r n_0\right) + \widetilde{n}\nu_\parallel - i\omega\frac{n_0\left(k_r^2+k_y^2\right)}{\omega_{ci}B}\left(\widetilde{\phi}+\frac{\widetilde{p}_i}{en_0}\right)$$

or

$$0 = \bar{\omega}\hat{n} - \alpha K_y\left(\hat{\phi} - \hat{n}\frac{L_n}{L_\phi}\right) + i\hat{n}\bar{\nu}_\parallel + \bar{\omega}\left(\alpha\hat{\phi}+\hat{n}\right)\left(K_r^2+K_y^2\right) \tag{3.32}$$

with $\hat{n} = \widetilde{n}/n$, $\hat{\phi} = e\widetilde{\phi}/T_e$, $L_{p_i}^{-1} = |\nabla_r \ln p_{0,i}|$, $L_\phi = -e\nabla_r\phi_0/T_e$, $\bar{\omega} = \omega/\omega_0$, $\bar{\nu}_\parallel = \nu_\parallel/\omega_0$, $K_y = k_y\rho_i$ and $K_r = k_r\rho_i$. In order to find a second relation between $\widetilde{n}$ and $\widetilde{\phi}$, the parallel component of the electron equation of motion (equation (3.7)) is considered:

$$m_e\left[n\frac{\partial V_{e,\parallel}}{\partial t} + \widetilde{n\left(\boldsymbol{V}_e\cdot\boldsymbol{\nabla}\right)V_{e,\parallel}}\right] = -en\left(\widetilde{E} + V_{0,e}\times\widetilde{\boldsymbol{B}}\right)_\parallel - \widetilde{\nabla_\parallel p_e} + \widetilde{R}_{e,\parallel} \tag{3.33}$$

where the electron viscosity has been neglected (this point can be checked using the drift ordering and reference [5] for the definition of $\overleftrightarrow{\pi}_e$). One could wonder why there is no term due to the magnetic field stochastization in equation 3.33, since the stochastization affects parallel transport, while the term $\nu_\parallel$ has been introduced in equation 3.32. The reason for this is that both the motion equation (2.26) in the model of section 2.3.2 and motion equation (3.33) are satisfied independently of each other, and thus decoupled. The term $R_{e,\parallel}$, denoting electron-ion interactions, reads [5]

$$R_{e,\parallel} = 0.51\frac{m_e \nu_e}{e} j_\parallel - 0.71 n \nabla_\parallel T_e. \tag{3.34}$$

The first component reflects electron-ion friction, while the second corresponds to the thermal force. The latter results from the temperature dependence of the electron collision length. The parallel electric current is defined by $j_\parallel = en(V_{i,\parallel} - V_{e,\parallel})$. Comparing the parallel components of the electron and ion motion equations, one sees that $\widetilde{V}_{i,\parallel} \ll \widetilde{V}_{e,\parallel}$, such that $\widetilde{j}_\parallel = -en\widetilde{V}_{e,\parallel}$ is assumed from now on. The unperturbed electron parallel velocity is assumed to be zero. According to equations (3.31), the unperturbed perpendicular electron velocity is

$$\boldsymbol{V}_{e,0} = \frac{\boldsymbol{B}}{B^2} \times \left(\boldsymbol{\nabla}_r \phi_0 - \frac{\boldsymbol{\nabla}_r p_{e,0}}{e n_0} \right) = -\frac{T_e}{eB} \left(\frac{1}{L_\phi} - \frac{1}{L_{p_e}} \right) \boldsymbol{e}_y, \tag{3.35}$$

with $L_{p_e}^{-1} = -\nabla_r \ln p_{e,0}$ and where the viscous drift is neglected due to the ordering. Equation (3.33) can now be written

$$\begin{aligned}
& m_e \left(i\omega + \frac{i k_y T_e}{eB} \left(\frac{1}{L_\phi} - \frac{1}{L_{p_e}} \right) \right) \frac{\widetilde{j}_\parallel}{e} \\
&= e n_0 \left(\nabla_\parallel \widetilde{\phi} + \nabla_r \phi_0 \frac{\widetilde{B}_r}{B} + \frac{\partial \widetilde{A}_\parallel}{\partial t} - \frac{T_e}{eB} \left(\frac{1}{L_\phi} - \frac{1}{L_{p_e}} \right) \widetilde{B}_r \right) \\
&\quad - T_e \nabla_\parallel \widetilde{n} - \nabla_r n_{e,0} \frac{\widetilde{B}_r}{B} + 0.51 \frac{m_e \nu_e}{e} \widetilde{j}_\parallel \\
&= e n_0 \left(\nabla_\parallel \widetilde{\phi} - i\omega \widetilde{A}_\parallel - \frac{T_e}{eB} \left(\frac{2}{L_\phi} - \frac{1}{L_{p_e}} - \frac{1}{L_n} \right) \widetilde{B}_r \right) - T_e \nabla_\parallel \widetilde{n} + 0.51 \frac{m_e \nu_e}{e} \widetilde{j}_\parallel
\end{aligned} \tag{3.36}$$

where equations (3.25) and (3.27) have been used together with the assumption of isothermal electrons. $\widetilde{A}_\parallel$ can be deduced from the parallel component of equation (3.28), making use of the definition $\boldsymbol{B} = \boldsymbol{\nabla} \times \boldsymbol{A}$:

$$\nabla_\parallel \left(\boldsymbol{\nabla} \cdot \widetilde{\boldsymbol{A}} \right) + \nabla^2 \widetilde{A}_\parallel = -\mu_0 \widetilde{j}_\parallel \qquad \text{or} \qquad \widetilde{A}_\parallel \approx \frac{\mu_0}{k_r^2 + k_y^2} \widetilde{j}_\parallel \tag{3.37}$$

in the drift ordering.. From this result, $\widetilde{B}_r$ can be determined:

$$\widetilde{\boldsymbol{B}} = \boldsymbol{\nabla} \times \widetilde{\boldsymbol{A}}_\parallel = (i k_y \boldsymbol{e}_r - i k_r \boldsymbol{e}_y) \widetilde{A}_\parallel \qquad \text{or} \qquad \widetilde{B}_r = i k_y \frac{\mu_0}{k_r^2 + k_y^2} \widetilde{j}_\parallel. \tag{3.38}$$

Equation (3.33) reads then

$$\begin{aligned} T_e\nabla_\parallel\widetilde{n} - en_0\nabla_\parallel\widetilde{\phi} =& m_e\Bigg[-\left(i\omega + \frac{ik_yT_e}{eB}\left(\frac{1}{L_\phi} - \frac{1}{L_{p_e}}\right)\right)\left(1 + \frac{1}{m_e}\frac{n_0e^2\mu_0}{k_r^2+k_y^2}\right) \\ &- \frac{ik_yT_e}{eB}\left(\frac{1}{L_\phi} - \frac{1}{L_n}\right)\frac{1}{m_e}\frac{n_0e^2\mu_0}{k_r^2+k_y^2} + 0.51\nu_e\Bigg]\frac{\widetilde{j}_\parallel}{e}, \end{aligned} \tag{3.39}$$

where $\widetilde{j}_\parallel$ has to be related to $\widetilde{n}$ and $\widetilde{\phi}$. Adding the continuity equations of ions and electrons after multiplication by their respective charge, the equation of charge density conservation can be obtained

$$\frac{\partial\rho}{\partial t} + \boldsymbol{\nabla}\cdot\boldsymbol{j} = 0 \tag{3.40}$$

with $\rho = e(n_i - n_e)$ is the charge density, and where S_e is taken to be zero for the same reason as evoked for ions in equation (3.29). Together with the quasi-neutrality condition, it becomes

$$\boldsymbol{\nabla}\cdot\boldsymbol{j} = 0 \qquad \text{or} \qquad \nabla_\parallel\widetilde{j}_\parallel = -\boldsymbol{\nabla}_\perp\cdot\widetilde{\boldsymbol{j}}_\perp. \tag{3.41}$$

The perpendicular perturbation current can be found from the sum of the ion and electron motion equations. Cross-multiplying this sum with $\boldsymbol{B}$ yields

$$m_in\boldsymbol{B}\times\frac{d\boldsymbol{V}_i}{dt} + m_en\boldsymbol{B}\times\frac{d\boldsymbol{V}_e}{dt} = \boldsymbol{B}\times(\boldsymbol{j}\times\boldsymbol{B}) - \boldsymbol{B}\times\boldsymbol{\nabla}\cdot(\boldsymbol{p}_i+\boldsymbol{p}_e)\,. \tag{3.42}$$

Calulating the divergence of the perpendicular component of equation (3.42), one gets:

$$\begin{aligned} \boldsymbol{\nabla}\cdot\widetilde{\boldsymbol{j}}_\perp =& \boldsymbol{\nabla}\cdot\left[\frac{\boldsymbol{B}\times\left(m_in\frac{d\boldsymbol{V}_i}{dt} + \widetilde{m_en\frac{d\boldsymbol{V}_e}{dt}} + \boldsymbol{\nabla}\cdot(\boldsymbol{p}_i+\boldsymbol{p}_e)\right)}{B^2}\right]_\perp \\ \approx& \boldsymbol{\nabla}\cdot\left[en\boldsymbol{V}_{p,i} + \widetilde{en\boldsymbol{V}_{*,i}} - en\boldsymbol{V}_{*,e}\right] \\ =& -i\omega\frac{k_r^2+k_y^2}{B\omega_{ci}}\left(en_0\widetilde{\phi} + T_i\widetilde{n}\right) - \frac{(T_e+T_i)\,\widetilde{n}}{RB}\left(ik_r\sin\theta + ik_y\cos\theta\right), \end{aligned} \tag{3.43}$$

with the assumption $m_e \ll m_i$. Results of appendix D, equation (D.30), were used in the last step. Applying $\nabla_\parallel$ to equation (3.39), and replacing

$\nabla_\parallel \widetilde{j}_\parallel$ found from relations (3.41) and (3.43), one obtains

$$T_e \nabla_\parallel^2 \widetilde{n} - en_0 \nabla_\parallel^2 \widetilde{\phi} = \tag{3.44}$$

$$\frac{m_e}{e}\left[-\left(i\omega + \frac{ik_y T_e}{eB}\left(\frac{1}{L_\phi} - \frac{1}{L_{p_e}}\right)\right)\left(1 + \frac{1}{m_e}\frac{n_0 e^2 \mu_0}{k_r^2 + k_y^2}\right) - \frac{ik_y T_e}{eB}\left(\frac{1}{L_\phi} - \frac{1}{L_n}\right)\frac{1}{m_e}\frac{n_0 e^2 \mu_0}{k_r^2 + k_y^2} + 0.51\nu_e\right] \times$$

$$\times \left[i\omega \frac{k_r^2 + k_y^2}{B\omega_{ci}}\left(en_0\widetilde{\phi} + T_i \widetilde{n}\right) + \frac{(T_e + T_i)\,\widetilde{n}}{RB}\left(ik_r \sin\theta + ik_y \cos\theta\right)\right]$$

or

$$\nabla_\parallel^2 \hat{n} - \nabla_\parallel^2 \hat{\phi} =$$

$$\frac{m_R}{\alpha L_n^2}\left[+\left(\bar{\omega} + \alpha K_y\left(\frac{L_n}{L_\phi} - \frac{L_n}{L_{p_e}}\right)\right)\left(1 + \frac{1}{m_R}\frac{\beta}{K_r^2 + K_y^2}\right) + \alpha K_y\left(\frac{L_n}{L_\phi} - 1\right)\frac{1}{m_R}\frac{\beta}{K_r^2 + K_y^2} + i0.51\bar{\nu_e}\right] \times \tag{3.45}$$

$$\times \left[\bar{\omega}\left(K_r^2 + K_y^2\right)\left(\alpha\hat{\phi} + \hat{n}\right) + \frac{L_n}{R}\left(1 + \alpha\right)\hat{n}\left(K_r \sin\theta + K_y \cos\theta\right)\right]$$

with $\bar{\nu_e} = \nu_e/\omega_0$, $m_R = m_e/m_i$ and $\beta = \mu_0 n_0 T_i/B^2$. The combination of the two equations obtained for the relation between the density and electric potential perturbations, equations (3.32) and (3.45), leads to an eigen-value equation for the density perturbation amplitude $N(l)$, see appendix E. It reads

$$\frac{\partial^2 N(\vartheta)}{\partial \vartheta^2} + S\big(T_1 + T_2 \cos\vartheta\big)N(\vartheta) = 0 \tag{3.46}$$

with $\vartheta = \theta - \frac{\pi}{4}$ and

$$S(\bar{\omega}, K_\perp) = m_R\left(\frac{qR}{L_n}\right)^2 \times \frac{(\bar{\omega} - \alpha K_\perp G_p)\left(1 + \frac{\beta}{2m_R K_\perp^2}\right) - \alpha K_\perp G_n \frac{\beta}{2m_R K_\perp^2} + i0.51\bar{\nu_e}}{\bar{\omega}\big[1 + (1+\alpha)\,2K_\perp^2\big] - \alpha K_\perp G_n + i\bar{\nu}_\parallel}$$

$$T_1(\bar{\omega}, K_\perp) = 2\alpha K_\perp^2 \bar{\omega}\left[K_\perp\left(1 + \alpha F\right) + \bar{\omega} + i\bar{\nu}_\parallel\right]$$

$$T_2(\bar{\omega}, K_\perp) = \sqrt{2}K_\perp^2 \frac{L_n}{R}\left(1 + \alpha\right), \tag{3.47}$$

with $F = \frac{L_n}{L_\phi}$, $G_p = \frac{L_n}{L_{pe}} - F$ and $G_n = 1 - F$. The assumption $k_r \approx k_y = k_\perp$ introduced in section 3.3.1 was used, with $K_\perp = k_\perp \rho_i$. The variables l and ϑ are related through $\partial l = qR\partial\vartheta$ according to equation (3.24), and the amplitude function $N(\vartheta)$ corresponds to $N(l)$ in definition (3.21).

3.3.3 Dispersion relation

Equation (3.46) can be rewritten in the form of a Mathieu equation by introduction of the variable $z = (\pi - \vartheta)/2$ and the functions $A = 4ST_1$ and $C = 4ST_2$:

$$\frac{\partial^2 N(z)}{\partial z^2} + \big(A - C\cos(2z)\big)N(z) = 0. \tag{3.48}$$

Periodic eigen-functions of the Mathieu equation are well known for real A and C [2]. They can be classified according to the number d of zeros they have on the interval $[0, \pi[$ and to their parity. Since the tokamak geometry imposes that $N(\theta)$ has a period of 2π, only π-periodic solutions $N(z)$ are considered in the following, i.e. d should be even. Reference [2] also gives the asymptotic dependences of A on C. This allows to establish approximate relations between these two parameters. For the lowest orders, one obtains:

$$A_{0,e} = -\frac{2C^2}{4+C}, \quad A_{2,e} = \frac{128 + 40C - 2C^2}{32 + C} \text{ and } A_{2,o} = \frac{96 + 4C - 2C^2}{24 + C} \tag{3.49}$$

where the indice of A is composed of the number d of zeros, and of a letter indicating whether A corresponds to an even (e) or an odd (o) Mathieu function.

However, in the present case, A and C are complex. In order to see whether the relations between complex A and C are the same and whether the corresponding eigen-functions have the same properties as the Mathieu functions, equation (3.48) has been solved numerically. By representing N as $N(z) = U(z) + iV(z)$ with $U(z)$ and $V(z)$ being real, equation (3.48) can be rewritten as a system of two second order equations with real parameters, and integrated numerically. This substitution provides also the value of A when C is given. Figure 3.3 represents the lowest order functions obtained by numerical integration for $C = 1.74 + i0.439$, which corresponds to typical TEXTOR edge parameters. For each of the couples (A, C) obtained, there is multitude of periodic solutions satisfying equation (3.49). They all have the same module (after normalisation), and two of these functions (with different boundary conditions) are represented in figure 3.3 for each couple. The integration for the above mentioned value of C leads to $A_{0,e} = -1.18 - i0.51$, $A_{2,e} = 4.94 + i0.379$ and $A_{2,o} = 3.77 - i0.124$, while relations (3.49) yield $A_{0,e} = -1.02 - i0.454$, $A_{2,e} = 5.69 + i0.356$ and $A_{2,o} = 3.78 - i0.115$. By varying the value of C, it has been found that the complex values of A calculated with relations (3.49) do not differ by more than 20 % from the ones obtained by numerical integration.

Relations (3.49) can be rewritten in the form of polynomial dispersion equations between the dimentionless wave number $K_\perp$ and the complex frequency ω, including other plasma parameters. These equations, which are respectively of the third and fourth orders in $\bar{\omega}$ for the zeroth and second order eigen-functions, are solved numerically by using a standard subroutine. Only the roots with the maximum growth rate $\gamma = \mathrm{Im}\,\omega$ are selected under the assumption that the corresponding modes are dominant in the transport. The $K_\perp$-spectrum of the growth rate for the zeroth and second orders solutions calculated according to equation (3.49) are shown in fig. 3.4 for the Tore Supra parameters used in section 6.1. It clearly shows that the growth rate of the zeroth order solution is much larger than the one of the second order solutions, such that in the following, only zeroth order solutions are considered. Solutions of order higher than 2 have not been investigated, and are assumed to bring much smaller contributions than the zeroth order. Figure 3.4 also shows that the dominant growth rate is maximum around $K_\perp = 0.1$.

The investigation of the solutions of equation (3.48) for complex A and C allowed to contribute to the study of plasma detachment and radiation at the edge, see reference [62].

3.3.4 Quasi-linear approximation for anomalous transport coefficients

The average radial component of the perpendicular particle flux due to unstable modes is determined by perturbations of the density and radial drift velocity, $\widetilde{n}$ and $\widetilde{V}_\perp$ and the phase between them:

$$\langle \Gamma_{\perp,r} \rangle = \widetilde{n}\widetilde{V}_r^\star + \widetilde{n}^\star \widetilde{V}_r \tag{3.50}$$

where $\langle\ \rangle$ denotes a time average, and * the complex conjugate. In appendix F, $\langle \Gamma_{\perp,r} \rangle$ is derived as the function of $\hat{\phi}$ only. This leads to

$$\langle \Gamma_{\perp,r} \rangle = 2\alpha^2 K_\perp^2 n v_{th,i} \frac{\mathcal{B}}{\mathcal{D}} |\hat{\phi}|^2 \tag{3.51}$$

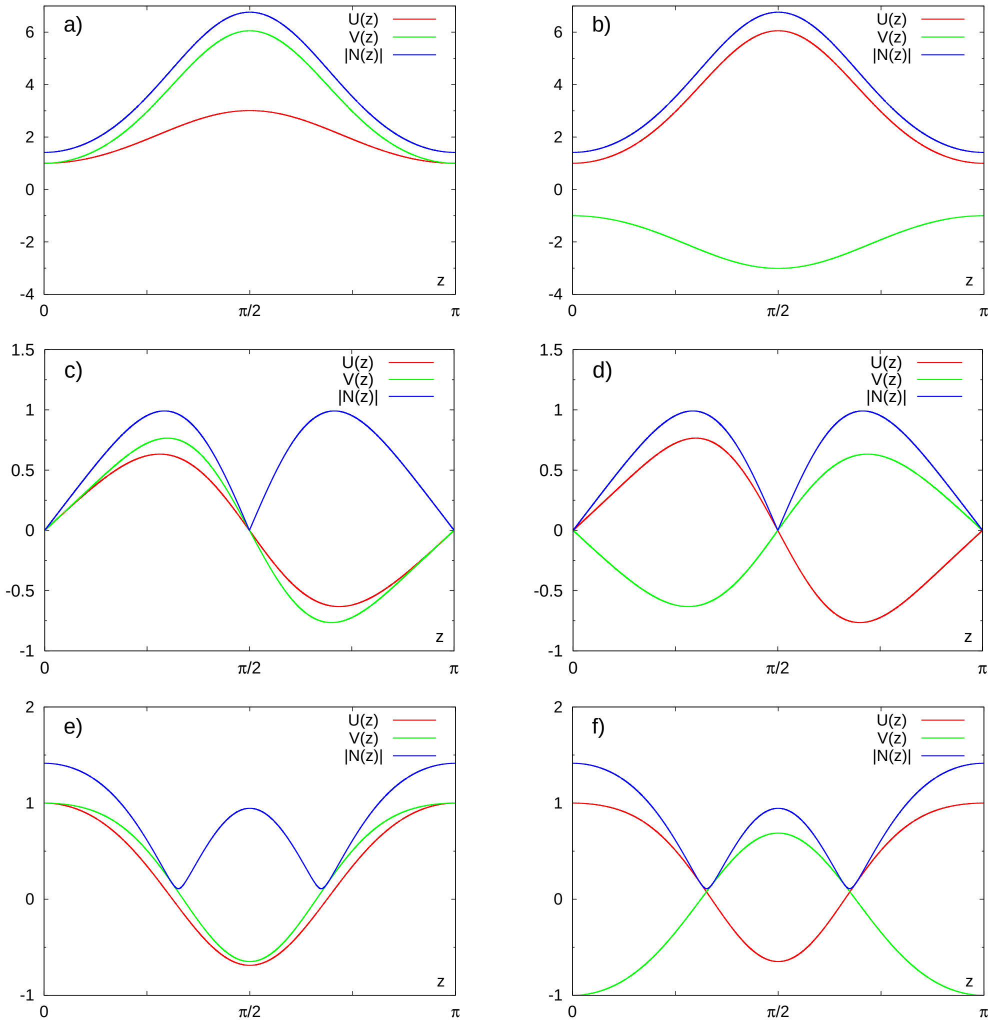

Figure 3.3: Solutions of equation (3.48) for complex A and C, obtained by numerical integration. a), b) represent even functions of order 0, c), d) odd functions of order 2 and e), f) even functions of order 2. The boundary conditions are given by fixing the value of the function (cases a), b), e) and f)) or its derivative (cases c) and d)) for $z = 0$. Other choices for the boundary conditions conserve $|N|$ (after normalisation), while the shapes of U and V are modified. The value of C was chosen for typical edge TEXTOR conditions, namely $n = 10^{19}\,m^{-3}$, $T_e = T_i = 150\,eV$, $L_n = 5\,cm$, $L_{p_e} = L_{p_i} = 2.5\,cm$, $q = 3$ and $R = 1.75\,m$, with the assumptions $K_\perp \approx \bar{\omega} \approx 0.1$. The electric shear and the parameter $\nu_\parallel$ are not taken into account. This yields $C = 1.74 + i0.439$, and the corresponding values obtained for A are $A_{0,e} = -1.18 - i0.51$ for the 0-th order, and $A_{2,e} = 4.94 + i0.379$ and $A_{2,o} = 3.77 - i0.124$ for the second order even and odd functions.

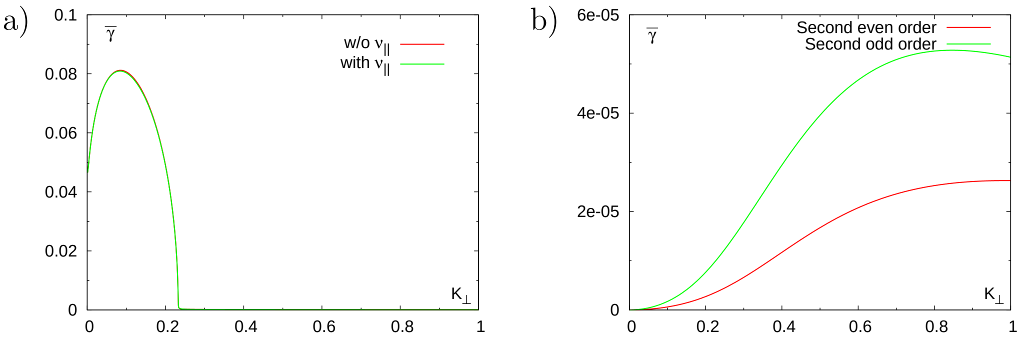

Figure 3.4: $K_\perp$-spectra of the growth rate for the a) zeroth and b) second order solutions of equation (3.48), calculated with the Tore Supra parameters used in section 6.1, namely $T_e = T_i = 205\,\mathrm{eV}$, $n = 1.3 \cdot 10^{19}\,m^{-3}$, $L_{T_e} = L_{T_i} = 7\,cm$, $L_n = 35\,cm$ and $L_\phi = \infty$. For the zeroth order, the influence of the parameter $\bar{\nu}_{||}$ is shown.

with

$$\begin{aligned} \mathcal{B} =& \bar{\gamma}\left[1 + 2K_\perp^2\left(1 + \alpha F\right)\right] + \left(1 - 2\bar{\omega}_r K_\perp\right)\bar{\nu}_{||} \\ \mathcal{D} =& \left[\alpha K_\perp F + \bar{\omega}_r\left(1 + 2K_\perp^2\right)\right]^2 + \left[\bar{\gamma}\left(1 + 2K_\perp^2\right) + \bar{\nu}_{||}\right]^2 . \end{aligned} \tag{3.52}$$

From a linear model, no saturation can be obtained for the perturbations. A quasi-linear approximation for the saturation level is estimated by renormalization [10, 13, 65]. It consists in balancing the linear growth with the non-linearity. Applying this balance on the ion continuity with the dominant drifts, namely the $\boldsymbol{E} \times \boldsymbol{B}$ and diamagnetic drifts, one gets a similar result as in references [28] and [65]:

$$\left|\frac{\partial \tilde{n}}{\partial t}\right| = \gamma\tilde{n} \sim \left|\left(\widetilde{V}_{E,i} + \widetilde{V}_{*,i}\right)\nabla_\perp \tilde{n}\right| \approx k_r k_y \rho_i v_{th,i}\left(\left|\hat{\phi}\right| + \left|\hat{n}\right|\right)\tilde{n} \tag{3.53}$$

or

$$\left|\hat{\phi}\right| \sim \frac{1}{2}\frac{\gamma}{K_\perp^2}\frac{\rho_i}{v_{th,i}} \tag{3.54}$$

where it is assumed that $\left|\hat{\phi}\right| \approx \left|\hat{n}\right|$ (see equation (E.1)). Under the assumption that the anomalous flux is purely diffusive, introduction of (3.54) into equation (3.51) yields the diffusion coefficient:

$$D_\perp = \omega_0 \rho_i^2 \frac{\alpha^2}{2}\frac{\bar{\gamma}^2}{K_\perp^2}\frac{\mathcal{B}}{\mathcal{D}}. \tag{3.55}$$

In order to compare this model with the ones of the literature, some simplifications are now applied to $D_\perp$: $\bar{\nu}_\parallel$ and the electric shear are neglected, $\alpha = 1$ is assumed, and only terms of the leading order in $K_\perp^2$ are kept. $D_\perp$ reads then

$$D_\perp = g\frac{\gamma}{k_\perp^2}\frac{\bar{\gamma}^2}{\bar{\omega}_r^2 + \bar{\gamma}^2} \quad \text{or} \quad D_\perp = gD_{gB}\frac{\bar{\gamma}}{K_\perp^2}\frac{\bar{\gamma}^2}{\bar{\omega}_r^2 + \bar{\gamma}^2}, \tag{3.56}$$

where $D_{gB} = \omega_0 \rho_i^2$ is the *gyro-Bohm* diffusion coefficient. The latter gives an estimation of the amplitude of $D_\perp$. For the typical TEXTOR edge conditions $T_i = 150\,eV$, $L_n = 5\,cm$ and $B = 2\,T$, one has $D_{gB} = 1.33\,m^2 s^{-1}$, which is of the order of magnitude needed to explain experimental observations. The particle diffusion coefficient obtained in equation (3.56) reproduces the so-called *improved*[7] *mixing-length estimate*, widely used for the particle diffusivity [10, 65, 67]. The coefficient g varies from author to author and it is 1/2 according to the present approach. However, since (3.55) (or (3.56)) is based on a quasi-linear approximation, a reasonable prediction for the dependence of $D_\perp$ on the different plasma parameters can be expected and only a rough estimate for the amplitude of $D_\perp$. Therefore, the factor g is henceforth considered as a parameter which can be adapted in order to match experimental observations.

The anomalous perpendicular heat conductivity $\kappa_\perp$ and viscosity coefficient $\mu_\perp$ still need to be determined. The perpendicular viscosity considered in chapter 2 results from transfer of parallel momentum across the magnetic field. This momentum transfer has two origins, namely collisions and anomalous transport. The former one brings a relatively small contribution to the transfer of momentum. According to reference [5], the corresponding viscosity coefficient is of the order of 10^{-2} to $10^{-3}\,m^2 s^{-1}$ for TEXTOR edge parameters. Therefore, the momentum transfer is dominated by anomalous transfer, and $\mu_\perp \approx D_\perp$ is assumed, as in reference [53]. The dependence on the background temperature gradient of $\langle q_{\perp,r} \rangle$, the radial component of the perpendicular heat flux due to unstable modes, has not been investigated. The anomalous perpendicular heat conductivity is henceforth assumed to be $\kappa_\perp = 3/2\, nD_\perp$ as was obtained in references [11] and [37].

3.3.5 Validity domain of the plasma fluid equations

The fluid model which has been introduced above contains some intrinsic limitations. By integration of the kinetic equation over the velocity space,

[7] The *mixing-length* estimate is a simpler version of (3.56), namely $D_\perp \approx \gamma / k_\perp^2$. It is obtained under the assumption that the background density gradient provides a limitation for the density pertubation amplitude, see e.g. reference [65].

information on the Larmor gyration of the particles is lost. This implies that this fluid model is suitable only for phenomena with frequencies much lower than the cyclotron frequency of the considered particles, and scale lengths perpendicular to $\boldsymbol{B}$ much larger than their Larmor radius. In both cases, ions give the most restrictive constraints, thus

$$\omega \ll \omega_{ci}, \qquad l_\perp \gg \rho_i \tag{3.57}$$

is required for any frequency ω or length $l_\perp$ perpendicular to $\boldsymbol{B}$. For a deuterium plasma with the typical conditions $B = 2$ T and $T_i = 150$ eV at the edge of TEXTOR, one has $\omega_{ci} \approx 10^8\,s^{-1}$ and $\rho_i \approx 0.9$ mm for the ion cyclotron frequency and Larmor radius. From the drift ordering, it is clear that the second relation of (3.57) is fulfilled. The frequency of the mode is of the order of $K_\perp v_{th,i}/L_n$, i.e. $\omega \approx 1.7 \cdot 10^5\,s^{-1}$ for the same conditions as above, and with $L_n = 5\,cm$ and $K_\perp \sim 0.1$, such that the first condition is also fulfilled.

By using a fluid model to represent the plasma, the further assumption that kinetic effects are negligible is implicitely made. In the perpendicular direction, particles are localized by the magnetic field such that kinetic effects can be neglected for $l_\perp \gg \rho_i$, this condition having just been checked above. In the parallel direction, conditions are more difficult to fulfil. One situation where kinetic effects can be neglected is

$$\frac{\omega}{k_\parallel} \gg v_{th}, \tag{3.58}$$

which correpsond to processes occuring so fast that particles appear to be stationary and thus localized [65]. For ions, condition (3.58) can be rewritten $\omega/k_\parallel \approx K_\perp q R v_{th,i}/L_n \gg v_{th,i}$, or $L_n \ll K_\perp q R \approx 50\,cm$ for $K_\perp = 0.1$, $R = 1.75\,m$ and $q = 3$. This last inequality shows that condition (3.58) is satisfied for ions, and kinetic effects can be neglected for them. For electrons, the situation is opposite, i.e. the phase velocity $\omega/k_\parallel$ is much smaller than the electron thermal velocity: $\omega/k_\parallel \approx K_\perp q R v_{th,i}/L_n \ll v_{th,e}$, or $L_n \gg \sqrt{m_e/m_i} K_\perp q R \approx 1\,cm$. In this case, kinetic effects cancel provided that the electron velocity distribution is symmetric [65]. Since electrons are isothermal (see appendix G), the electron velocity distribution is indeed symmetric, and the conditions required for a fluid description of the plasma to be valid in the parallel direction are fulfilled.

The quasi-neutrality approximation can be checked by calculating the Debye length and the electron plasma frequency for typical TEXTOR edge conditions. For $T_e = 150\,eV$ and $n = 10^{19}\,m^{-3}$, one finds $\lambda_D = 2.9 \cdot 10^{-5}\,m$ and $\omega_{pe} = 1.8 \cdot 10^{11}\,s^{-1}$, such that $\omega \ll \omega_{pe}$ and $l_\perp \gg \lambda_D$ are fulfilled, which confirms the validity of the quasi-neutrality approximation for both background and perturbation densities.

In section 3.3, the assumption $\boldsymbol{\nabla}\widetilde{p}_{e,i} = T_{e,i}\boldsymbol{\nabla}\widetilde{n}$ has been used, that is electrons and ions are assumed to be isothermal. It is shown in in appendix G that this assumption is correct for electrons at TEXTOR edge, but is not valid for ions if their temperature is lower than about $100\,eV$. Therefore, the present model is valid only for $T_i \gtrsim 100\,eV$.

Chapter 4

The RITM transport code

The transport code RITM has been used in the present work in order to simulate self-consistently plasma parameters in TEXTOR discharges. The main features of this code and the equations it solves are presented in section 4.1. Since the boundary layer for computations with RITM, the Last Closed Magnetic Surface (LCMS), is destroyed by magnetic field stochastization, a new boundary layer is defined in section 4.2 for discharges with DED. Then, some precisions on the transport model used in RITM are given in section 4.3. Finally, the main problems faced during simulations are briefly shown in section 4.4 and the impact of some free parameters in RITM is discussed in section 4.5.

4.1 Main features and equations solved by the code RITM

The code RITM [34, 59] (Radiation from Impurities in Transport Model) allows to compute the variation of diverse plasma parameters along the effective minor radius r, from the plasma axis to the LCMS. It is a 1.5D fluid code, ".5" meaning that it takes the into account the effects of the toroidal geometry, through the Shafranov shift (section 2.1), the elongation and the triangularity of magnetic surfaces. It solves continuity equations for the densities n_e and n_Z of electrons and impurity ions with different charges Z:

$$\begin{aligned}
\frac{\partial n_e}{\partial t} + \frac{1}{rg_1}\frac{\partial}{\partial r}(rg_2\Gamma_r^e) &= S_b + S_r + \sum_Z ZS_Z \\
\frac{\partial n_Z}{\partial t} + \frac{1}{rg_1}\frac{\partial}{\partial r}(rg_2\Gamma_r^Z) &= S_Z
\end{aligned} \tag{4.1}$$

where Γ_r^e and Γ_r^Z are the particle fluxes perpendicular to the magnetic field, including both diffusive and convective components:

$$\begin{aligned} \Gamma_r^e &= -D_{eff}^e \frac{\partial n_e}{\partial r} + V_{eff}^e n_e \\ \Gamma_r^Z &= -D_{eff}^Z \frac{\partial n_Z}{\partial r} + V_{eff}^Z n_Z \end{aligned} \tag{4.2}$$

with $D_{e,Z}^{eff}$ and $V_{e,Z}^{eff}$ being the electron and impurity radial diffusivities and pinch velocities. Note that all these quantities (and the ones introduced in the following) are averaged over the poloidal angle. The metric coefficients $g_1(r)$ and $g_2(r)$ are calculated from the Grad-Shafranov equation and account for the toroidal geometry: g_1 takes into account the increase of the area of the magnetic surfaces due to the Shafranov shift, and g_2 is a correction for the poloidal dependence of the distance between neighboring magnetic surfaces. The particle source densities S_b, S_r and S_Z are respectively due to ionization of energetic atoms from the neutral beam injection, of neutrals entering the LCMS and of impurity ions of charge Z. The radial distribution of S_b is taken from the code TRANSP and its amplitude is an input parameter of RITM.

The source S_r of neutrals is composed of four neutral species: *molecules* desorbed from the walls and other plasma facing components; *Franck-Condon atoms*[1] generated by molecule dissociation; *reflected atoms*, that is atoms arising from reflection of plasma ions on material surfaces; *hot atoms* resulting from charge-exchange with molecules, Franck-Condon atoms or reflected atoms, or coming from ion-electron recombination. The distribution of the first three species of neutrals is approximated by a two-velocity distribution function over the radial velocity component v_r. It is assumed in the form

$$f_n(r, v_r) = \frac{1}{2} n_n(r) \left[\delta(v_r - v_n) + \delta(v_r + v_n)\right] \tag{4.3}$$

where $\delta(\,)$ is the Dirac delta function, and n_n, T_n, $v_n = \sqrt{T_n/m_n}$ and m_n are the density, temperature, thermal velocity and mass of the considered neutrals. The radial variation of n_n and T_n is described by the transport equations obtained as moments of the kinetic equations for f_n:

$$\frac{v_r}{g_1} \frac{\partial f_n}{\partial r} = S_n - \nu_n f_n \tag{4.4}$$

[1]Franck-Condon atoms result from ionization or dissociation of a molecule, $D_2^+ \rightarrow D_{fc} + D^+$ and $D_2 + e^- \rightarrow 2D_{fc} + e^-$ respectively.

where S_n is the density of neutral particle sources and ν_n the effective frequency for destruction of particles by ionization, dissociation or charge exchange. In the case of molecules and reflected atoms, S_n is located at the edge. For Franck-Condon atoms, the source is distributed over a wider region since it results from the destruction of molecules. Note that g_1 is taken into account in equation (4.4) but not g_2 since neutrals are not sensitive to the magnetic topology. For hot atoms, the kinetic equation

$$\frac{1}{g_1}\frac{\partial}{\partial r}(v_r f_*) = S_* - \nu_* f_* + k_{cx} n_i n_* \tag{4.5}$$

is used, where f_*, n_* and S_* are respectively the distribution function, density and source density of hot atoms, and ν_* is the frequency at which they undergo ionization or charge exchange, $\nu_* = k_i n_e + k_{cx} n_i$. The charge exchange process involving hot atoms destroys hot atoms with a distribution f_* and produces new ones with a density $k_{cx} n_i n_*$. The latter source has an isotropic velocity distribution since ions have a negligible radial drift velocity and undergo charge exchange at all angular positions of their Larmor gyration with an equal probability.

The density and flux of main ions are computed according to the quasi-neutrality condition:

$$\begin{aligned} n_i &= n_e - \sum Z n_Z \\ \Gamma_r^i &= \Gamma_r^e - \sum Z \Gamma_r^Z . \end{aligned} \tag{4.6}$$

Calculations can be performed with ions of He, C, O, Ne, Si and Ar impurities of all charge states, but since impurities have not been taken into account in this work, one has $n_i = n_e$ and $\Gamma_r^i = \Gamma_r^e$.

The electron and ion temperatures are determined from the heat balance equations

$$\begin{aligned} \frac{3}{2}\frac{\partial}{\partial t}(n_e T_e) + \frac{1}{r g_1}\frac{\partial}{\partial r}(r g_2 H_r^e) &= Q_{oh} + Q_{aux}^e - Q_{ei} - Q_{en} - Q_{eI} \\ \frac{3}{2}\frac{\partial}{\partial t}(n_\Sigma T_i) + \frac{1}{r g_1}\frac{\partial}{\partial r}(r g_2 H_r^\Sigma) &= Q_{aux}^i + Q_{ei} - Q_{in} \end{aligned} \tag{4.7}$$

with $n_\Sigma = n_i + \sum n_Z$. Q_{oh} is the ohmic heating source density, Q_{ei}, Q_{en} and Q_{eI} are the energy loss densities of electrons respectively through Coulomb collisions with ions, excitation and ionization of neutral and impurities, and Q_{in} is the density of energy exchange between ions and neutrals. $Q_{aux}^{e,i}$ are the electron and ion heating source densities from auxiliary heating. The latter come from neutral beam injection and radio frequency waves, and their radial profiles are taken from TRANSP simulation results. The electron and ion radial energy fluxes are

$$H_r^{e,\Sigma} = \frac{3}{2}\Gamma_r^{e,\Sigma} T_{e,i} - \kappa_{e,i}^{eff} \frac{\partial T_{e,i}}{\partial r} \tag{4.8}$$

with $\kappa_{e,i}^{eff}$ the effective electron and ion radial heat conductivities.

The boundary conditions for equations (4.1) and (4.7) are fixed by setting the radial derivatives to zero at $r = 0$, and by prescribing the density and temperature e-folding lengths for electrons and ions at the LCMS, these lengths being taken from measurements. The other input parameters of the code are the geometric properties of the tokamak (minor and major radii in the case of a circular tokamak like TEXTOR), the toroidal magnetic field, the plasma current, the additional heating power and the gas puffing rate.

4.2 Estimate of the LCMS position with DED magnetic field perturbations

The LCMS separates the regions of the plasma where transport is dominated by perpendicular transport (inside of the LCMS) and by parallel transport (outside of it). This surface forms the boundary for RITM simulations because the transport model of the latter is not suitable for describing the region where parallel transport prevails. However, if the edge magnetic field is stochastic, the LCMS is destroyed and another boundary layer has to be defined. As mentioned in sections 2.2.3 and 2.3, the edge region is then divided into two zones: the ergodic zone, where transport results from a combination of parallel and perpendicular transports, and the laminar zone, where transport takes place only along the field lines. The former zone can be described by the models of chapters 2 and 3, but not the latter one. Therefore, RITM simulations are restricted to the central part of the plasma. There is however no commonly accepted definition for the border between the ergodic and laminar zones. In the present work, this is defined as the radial position from which field lines hit the limiter or the plates[2] protecting the DED after a distance corresponding to one half of a poloidal turn. In other words, the laminar zone includes all the field line segments connecting the LFS of the tokamak to the DED plates (located at the HFS) or to the limiter by the shortest way, being not larger than one half poloidal turn.

[2] In the absence of stochastization, the LCMS is generally determined by the limiter, but when the DED is operated, the plasma is often shifted towards the latter in order to increase the perturbation level. Therefore both the DED plates or the limiter can limit the plasma radius.

The width of the so defined zone has been calculated [38] under the assumption that the radial magnetic field perturbation from the DED is in the form [15]

$$B_r(r,\theta,\varphi) = B_r^0 \left(\frac{r}{r_c}\right)^{M_*-1} \sin(M_*\theta - N_*\varphi) \tag{4.9}$$

with $B_r^0 \approx 5\mu_0 I_{DED} N_*/(\pi r_c)$, r_c the radial position of the DED coils, I_{DED} the current in these coils, and M_*, N_* the poloidal and toroidal numbers of the main perturbation mode induced by the DED. The radial and longitudinal coordinates along a field line are related by

$$\frac{dr}{B_r} = \frac{dl}{B_\varphi}, \tag{4.10}$$

and the longitudinal coordinate can be related to the phase variable $\psi_* = \theta - N_*\varphi/M_*$ through the relation

$$d\psi_* = d\theta - \frac{d\varphi}{q_*} = \frac{d\varphi}{q(r)} - \frac{d\varphi}{q_*} = \frac{dl}{R}\left(\frac{1}{q(r)} - \frac{1}{q_*}\right) \tag{4.11}$$

where $q_* = M_*/N_*$ is the safety factor on the resonant surface of radius r_* and $q(r)$ is the safety factor varying along the considered field line. By combining equations (4.10) and (4.11) and assuming a parabolic radial profile [1] for the safety factor in the edge region, namely $q(r) = q_*(r/r_*)^2$, one obtains an equation for the radial displacement of a field line as a function of ψ_*:

$$\int_{r_L}^{r_p} r_c^{M_*-1} \frac{r_*^2 - r^2}{r^{M_*-1}} dr = \int_{\psi_*^i}^{\psi_*^f} \frac{B_r^0}{B_\varphi} q_* R \sin(M_*\psi_*) d\psi_* \tag{4.12}$$

with r_p the radial position of the DED plates and r_L the radial position of the layer at the limit between the ergodic and laminar zones, i.e. the searched radius. The initial and final values ψ_*^i and ψ_*^f of the variable ψ_* are not known a priori. Therefore, the maximal value of $w_L = r_p - r_L$ corresponding to the laminar zone width, has been searched for by numerical integration of (4.12) for all possible values ψ_*^i. The obtained maximal width w_L is shown in figure 4.1 as a function of the DED coil current for the different DED modes. In the following, the radius r_L corresponding to the maximal w_L is taken as the boundary layer for RITM simulations with DED, except if the limiter imposes a smaller radius.

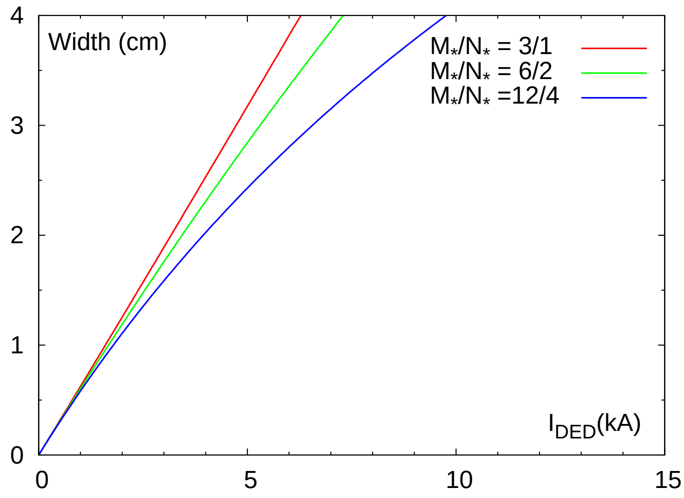

Figure 4.1: Estimated laminar zone width as a function of the DED current for the 3 possible configurations. The parameters for this calculation are $B_\varphi = 2.25\,T$, $r_* = 35\,cm$, $r_p = 46\,cm$ and $r_c = 53.25\,cm$.

4.3 Incorporation of the developed transport model into RITM

The model developed in chapter 2 for effective transport coefficients in the radial direction has been implemented into the code RITM (in equations (4.2) and (4.8)). For the anomalous perpendicular transport coefficients on which this model is based, two different models have been considered: the one from the literature, presented in section 3.2, and the one developed in section 3.3. The former will be referred to as model A and the latter as model B.

For model A, the total anomalous particle diffusivity is assumed

$$D_\perp^e = D_\perp^\Sigma = D_\perp^c + f_{tr} D_\perp^{ITG} + D_\perp^{TE} + D_\perp^{DRB} + f_{DA} D_\perp^{DA}, \tag{4.13}$$

where $D_\perp^c$ is a semi-empirical coefficient assumed in the form $D_\perp^c[m^2/s] = 0.1(1-(r/a)^2)$, with a the plasma radius. It is added in order to prescribe transport in the core where all drift contributions are low due to small gradients. The reason for which $D_\perp^{ITG}$ is proportional to the trapped particle fraction is that in a linear electrostatic approximation, an ITG instability does not produce electron transport, and thus also no particle transport [65]. However, such an instability can generate particle losses through stochastization of closed drift orbits, which most easily happens to trapped particles [27] (this stochastization has nothing to do with the DED). The coefficient f_{DA} has been used in simulations of ohmic shots because the DA contribution to particle transport in the plasma core was seen to be much higher in this case than one could expect from this instability. The value of this coefficient is discussed where it is used, and it is 1 if not stated otherwise.

For model B, the contribution from edge instabilities to the anomalous perpendicular particle diffusivity is given by equation (3.55). The contribution from core instabilities is computed according to the model of reference [34]. This model takes ITG and TE instabilities into account by assuming small perturbations of density, electric potential and ion temperature. From the ion continuity, motion and heat balance equations for these perturbations, a dispersion relation is obtained, and an anomalous particle transport is defined on the same way as in section 3.3.4. The total anomalous diffusivity for model B reads

$$D_\perp^e = D_\perp^c + f_{tr} D_\perp^{ITG} + D_\perp^{TE} + D_\perp^{edge} \tag{4.14}$$

where $D_\perp^{ITG}$ and $D_\perp^{TE}$ are the contributions from ITG and TE instabilities extracted from the total transport according to reference [34], and $D_\perp^{edge}$ is the coefficient given by (3.55).

In both models, the electron anomalous perpendicular heat conductivity is taken in the form

$$\kappa_\perp^e = \frac{3}{2} n_e D_\perp^e. \tag{4.15}$$

with the same justification as the one given in section 3.3.4. The ion heat conductivity assumes the form

$$\begin{aligned} \kappa_\perp^i &= \kappa_\perp^{i,neo} + \frac{3}{2} n_\Sigma \left(D_\perp^c + D_\perp^{ITG} + D_\perp^{DRB} + D_\perp^{DA} \right) && \text{(model } A\text{)} \\ \kappa_\perp^i &= \kappa_\perp^{i,neo} + \frac{3}{2} n_\Sigma \left(D_\perp^c + D_\perp^{ITG} + D_\perp^{edge} \right) && \text{(model } B\text{)} \end{aligned} \tag{4.16}$$

where $\kappa_\perp^{i,neo}$ is the neoclassical contribution to heat transport due to collisions, calculated according to reference [25]. The fact that the electron neoclassical contribution is neglected and not the ion one results from the proportionality of $\kappa_\perp$ to the square root of the particle mass. Since ITG instabilities lead to ion heat transport even without orbit stochastization, the factor f_{tr} does not appear in the heat conductivity, but well in the particle diffusivity.

It is generally assumed that peaked density profiles observed in tokamaks result from the existence of an inward particle pinch [12, 66, 70]. The nature of this pinch remains a wide open question in the literature, but different mechanisms leading to such a pinch have been proposed [3, 19, 64]. In the following, the pinch velocity is assumed in the form

$$V_\perp^e = -\left(\frac{4r}{3R} f_{tr} D_\perp^{ITG} + D_\perp^{TE} \right) \frac{\nabla_r q}{q} + \alpha_T \left(f_{tr} D_\perp^{ITG} + D_\perp^{TE} \right) \frac{\nabla_r T_e}{T_e}. \tag{4.17}$$

The first term is the so called curvature pinch. It is due to the conservation of the longitudinal adiabatic invariant $J = \oint v_{\|} dl$ [8] associated with the bounce motion of trapped particles. It is demonstrated in reference [44] that through the conservation of J, trapped electrons tend to maintain the product nq constant, leading to a pinch velocity $-D_{\perp}^{TE} \nabla_r q/q$. In reference [3], it is shown that in the case of ion-driven turbulence, trapped particles tend to keep the relation $n \propto 1 - 4/(3R) \int_0^r \nabla_r q/q \; dr$ between n and q, giving rise to a pinch velocity $-4r/(3R) f_{tr} D_{\perp}^{ITG}$. The second term is due to the so called thermodiffusion [12]. Though one can expect [7] particle diffusion to depend on other gradients than the density gradient, the physical reason for thermodiffusion is not completely clear yet. Therefore, the coefficient α_T is taken as a free parameter, and the value it takes in order to reproduce experimental profiles varies from model to model [66].

4.4 Achievement of stable code operation for TEXTOR

After implementation of the transport model into RITM and adaptation of the geometry to TEXTOR, the ability of the code to reproduce TEXTOR discharges has been tested. A number of problems has been faced during these tests, some of which are detailed below. This series of tests also allowed to introduce some corrections in the code.

The largest difficulty encountered was to reach steady state profiles. In order to understand this difficulty, it is useful to know the scheme used in RITM to solve the equations presented in section 4.1. Equation (4.1) for instance is in the form:

$$\frac{\partial n}{\partial t} + \nabla_r \left[-D_{\perp}(n, T) \frac{\partial n}{\partial r} \right] = 0, \tag{4.18}$$

where the convective part nV^{eff} of the particle flux and the source term S on the right-hand side are not considered for the sake of clarity. In RITM, after discretization of time and spatial dimensions, it takes the form

$$\frac{n^{k,j} - n^{k-1,conv}}{\tau} + \nabla_r \left[-D_{\perp}(n^{k,j-1}, T^{k,j-1}) \frac{\partial n^{k,j}}{\partial r} \right] = 0 \tag{4.19}$$

where τ is the time increment between consecutive time steps denoted by the superscripts $k-1$ and k, and the superscript j stands for the internal iterations performed for a single time step. One sees from this equation that the density at iteration j is calculated with transport coefficients which are themselves computed on the basis of plasma parameters from the previous iteration $(j-1)$. An iteration over the superscript j is thus necessary in order to reach a converged state $n^{k,conv}$ for each time step k. Initially, RITM solved the non-linear transport equations by iterating the following loop and using the convergence test 1 below:

$$\kappa_\perp^{k,j}, D_\perp^{k,j}, S^{k,j}, ... \quad \text{calculated with} \quad n^{k,j-1}, T^{k,j-1}, \frac{\partial}{\partial r} n^{k,j-1}, \frac{\partial}{\partial r} T^{k,j-1}, ...$$

$$\Downarrow$$

$$n^{k,j,int}, T^{k,j,int} \quad \text{calculated with} \quad \kappa_\perp^{k,j}, D_\perp^{k,j}, S^{k,j}, ...$$

$$\Downarrow$$

$$\begin{aligned} n^{k,j} &= (1-a_{mix})n^{k,j-1} + a_{mix}n^{k,j,int} \\ T^{k,j} &= (1-a_{mix})T^{k,j-1} + a_{mix}T^{k,j,int} \end{aligned} \qquad a_{mix} \leq 0.1$$

$$\Downarrow$$

$$\text{convergence (test 1) ?}$$

$$\text{if} \quad \left| \frac{n^{k,j} - n^{k,j-1}}{n^{k,j-1}} \right| \geq \epsilon \quad \text{or} \quad \left| \frac{T^{k,j} - T^{k,j-1}}{T^{k,j-1}} \right| \geq \epsilon \quad \Longrightarrow \text{next } j$$

$$\text{else} \quad \begin{aligned} n^{k,conv} &= n^{k,j} \\ T^{k,conv} &= T^{k,j} \end{aligned} \quad \Longrightarrow \text{next time step}$$

Note that $n^{k,j}$ and $T^{k,j}$ are obtained by mixing the solution at an intermediate step $(n^{k,j,int}, T^{k,j,int})$ with the solution from the previous iteration $(n^{k,j-1}, T^{k,j-1})$. This slows down convergence, but if this is not done, overshootings occur, which can result in oscillations from iteration to iteration.

Figure 4.2 shows the converged (with test 1) density and temperature profiles obtained at different time steps for a simulation of discharge # 97315 at TEXTOR with transport model B (these profiles correspond to $n^{k,conv}$ and $T^{k,conv}$ for different values of k). To see whether the steady state has been really reached or not, the converged profiles at successive time steps (successive values of k) are compared. A comparison of the density and temperature profiles for $k = 15$, 18, 19 and 20 (see figs 4.2 a) and b)) seems to indicate that the steady state has been reached. This is however not the case. One can see in figs 4.2 c) and d) that the profiles $n^{k,conv}$ and $T^{k,conv}$ for which the convergence criterion (test 1) is satisfied differ considerably from the profiles $n^{k,j,int}$ and $T^{k,j,int}$ calculated directly from the transport equations at the last step. If the code is run for another 20 time steps, density and temperature profiles still change significantly (see figs 4.2 e) and f)). By running RITM for 100 time steps[3], one gets another problem:

[3]Note that 100 time steps correspond to 10 s, which is already longer than a TEXTOR discharge, and much longer than characteristic time scales for variation of profiles.

profiles exhibit oscillations (related to the spatial discretization of equations) despite the smoothing procedure used in order to damp these oscillations. This problem of oscillations has been investigated but could not be solved.

Consider now the test 1 performed above to check whether convergence has been reached or not: the profiles compared are the ones from two consecutive iterations. That is why so large differences are observed between the "converged" profiles ($n^{k,conv}$ and $T^{k,conv}$) and the profiles obtained at the intermediate step ($n^{k,j,int}$ and $T^{k,j,int}$ for $j = j^{conv}$). The reason for the non-convergence of the profiles is the decrease[4] of a_{mix} to very small values. The mixing between the solutions from the previous iteration and from the intermediate step then almost does not take the latter into account. Fixing a constant value for a_{mix} most of the time leads to numerical problems, generally oscillations around the solution of the transport equations. In order to overcome this problem, the convergence test as been changed to the following convergence test 2:

$$\begin{array}{lccl} \text{if} & \left|\dfrac{n^{k,j} - n^{k,j,int}}{n^{k,j,int}}\right| \geq \epsilon \quad \text{or} \quad \left|\dfrac{T^{k,j} - T^{k,j,int}}{T^{k,j,int}}\right| \geq \epsilon & & \Longrightarrow \text{next } j \\ \text{else} & \begin{array}{c} n^{k,conv} = n^{k,j} \\ T^{k,conv} = T^{k,j} \end{array} & & \Longrightarrow \text{next time step} \end{array}$$

that is profiles are compared with the solutions computed at the intermediate step and not with profiles from the previous iteration (which can be quite different from the ones from equations). Despite the modification of convergence test, no actual steady state solution could be obtained for discharge # 97315 with transport model B.

Since all these investigations consumed a large amount of time, it was decided to simplify and continue the present work with well-tested transport models from the literature, i.e. transport model A instead of B. This allows to avoid the problems linked to the new model for anomalous transport and get converged solutions. Note however that no convergence problems were faced when this model was used to describe the H-mode[5] power threshold in TEXTOR, see ref. [36].

[4]The code is written in such a way that a_{mix} is decreased when the relative difference between successive profiles increases from iteration to iteration.

[5]The H-mode is an improved confinement regime which has been observed in several tokamaks when a high auxiliary heating power is applied.

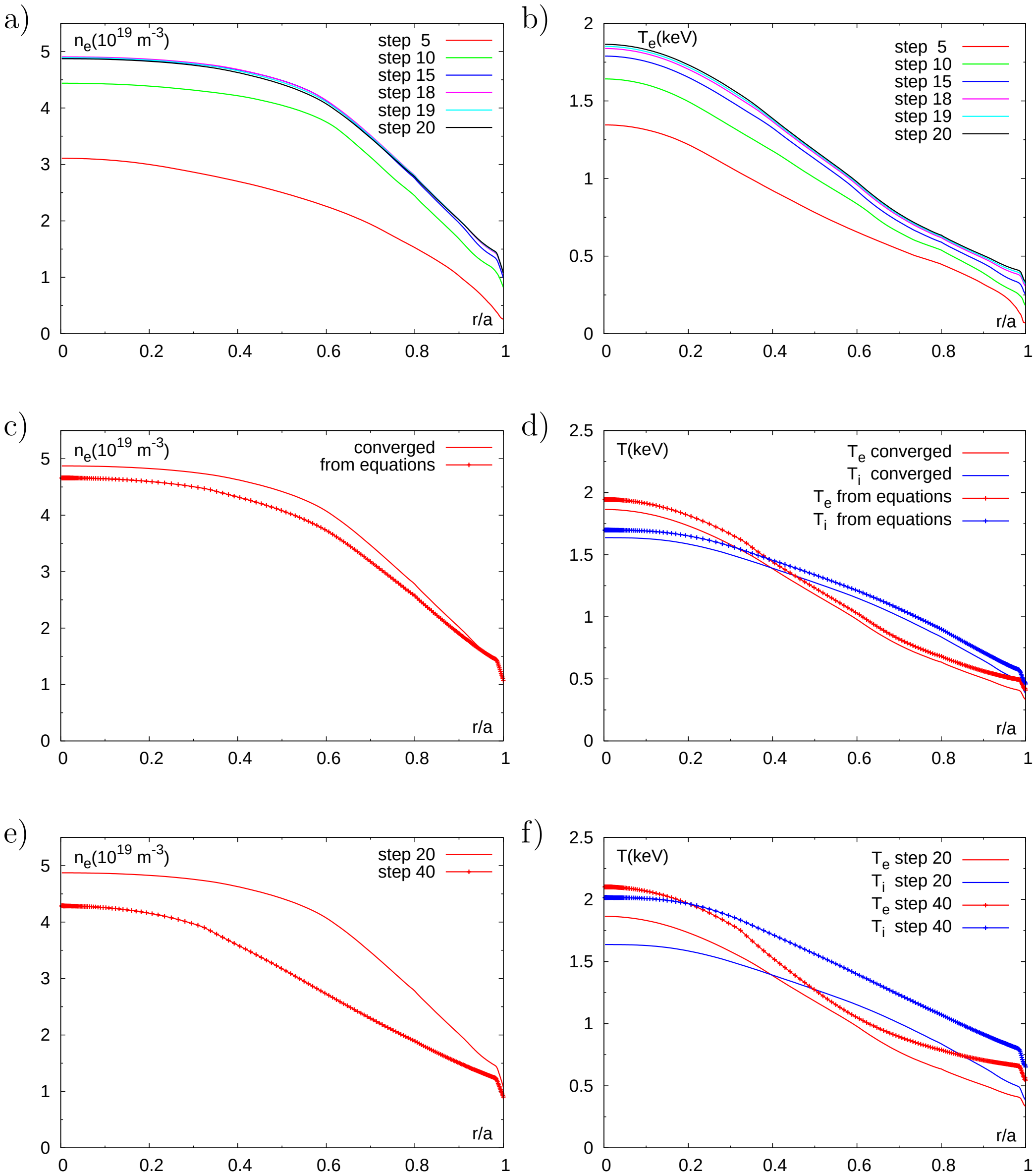

Figure 4.2: Figures a) and b) show the converged (with test 1) density and temperature profiles $n^{k,conv}$ and $T^{k,conv}$ obtained with RITM at different time steps (different values of k) versus the reduced radius r/a. These simulations were performed for an auxiliary heated discharge with transport model B. In figures c) and d), these profiles for time step 20 (thus $k = 20$) are compared with the intermediate ones ($n^{20,j,int}$ and $T^{20,j,int}$) calculated directly from the transport equations at the same time step. Figures e) and f) show the further evolution of these profiles by comparing the converged profiles for time steps 20 and 40. Note that for the sake of clarity ion temperature profiles are not represented in figure b), but they show the same 'converging' behavior as electron density and temperature.

a) b)

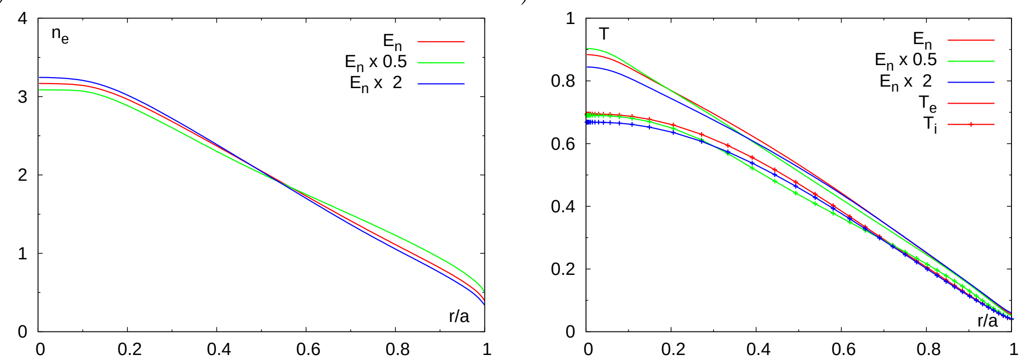

Figure 4.3: Density a) and temperature b) profiles for the simulation of an ohmic discharge in TEXTOR. The different curves show the modification of the profiles when the energy of neutrals is multiplied by a certain factor. The gas puffing was adjusted in order to have the same line averaged density for all these simulations.

4.5 Investigation of free parameters

Several parameters in RITM can be freely choosen. This is the case for some parameters in the transport model and for the input parameters coming from experimental data. The dependence of the density and temperature profiles on these parameters has been investigated, and some of these investigations are presented here.

First of all, the gas puffing rate is not always provided by measurements. And when it is, then the recycling coefficient for the particles reentering the plasma is not given. In RITM, the uncertainty on these two parameters is removed by fixing the recycling coefficient, and adjusting the gas puffing rate until the line average density matches the experimental one.

Secondly, the energy of the neutrals recycling into the plasma, or produced by charge-exchange and recombination in the plasma, is not well defined. Tests of density and temperature dependences on these energies have been performed. They show that a modification of the energy of neutrals by a factor as large as two leads to noticeable changes in density and temperature profiles (see figure 4.3), but not dramatic (they remain below errors for experimental data).

The boundary condition given by the e-folding lengths of density and temperatures also introduce some uncertainties. Measurements by means of beam emission spectroscopy on thermal helium [26] provide these lengths for some discharges in TEXTOR. They show that for ohmic discharges, the edge density e-folding length is of the order of 2 cm while the electron temperature e-folding length is about 5 cm. Since this measurement does not provide the ion e-folding length, it is assumed that it is equal to the electron one. For discharges with auxiliary heating, the density e-folding length slightly increases till about 3.5 cm for 1.2 MW of heating power, while the electron temperature e-folding length remains unchanged. The effect of the density e-folding length value on density and temperature profiles for an ohmic discharge are shown in fig. 4.4 a). One can see that for a variation of 25 %, it has a very weak impact on temperature profiles, and a moderate effect on the density profile. The temperature e-folding lengths have a much weaker impact on the density and temperature profiles, and are therefore not shown here.

Finally, the importance of thermodiffusion has been examined by varying the parameter α_T in equation (4.17). One can see in figure 4.4 b) that this parameter has a relatively weak impact on temperatures, and provides a moderate density peaking. Note that in some particular cases, a modification of the parameter α_T leads to the suppression of ITG instabilities, and its impact on density and temperature profiles is then larger than shown in fig. 4.4 b). An extensive discussion of thermodiffusion is however out of the scope of the present work.

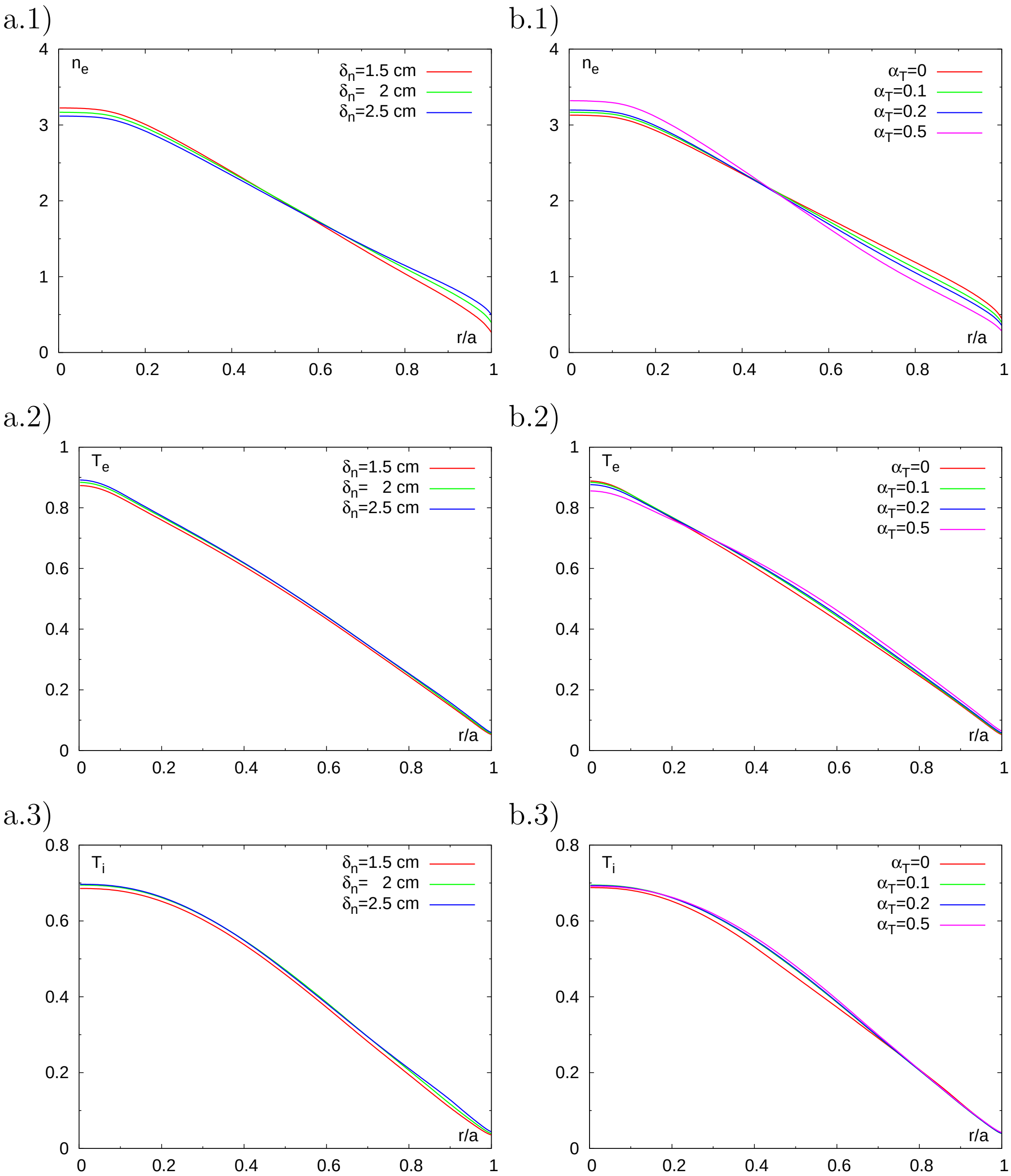

Figure 4.4: Density and temperature profiles calculated with RITM for an ohmic discharge. The left column shows the impact of the electron boundary e-folding length δ_n on these profiles while the right column shows the impact of thermodiffusion (parameter α_T). The gas puffing was fixed so as to give the same line averaged density for all the computations

Chapter 5

Experimental investigation of the DED effect on the energy confinement

The influence on plasma energy confinement is one of the most important characteristics of the DED performances. In order to validate the modelling approach presented in previous chapters, measurements with the so-called *diamagnetic loops* have been performed to measure the plasma diamagnetic energy. Due to the lack of staff, this diagnostic was not operated since the DED has been installed. Significant efforts have been applied to put it back into operation, and some problems, which were not recognized before, have been solved.

In this chapter, an overview of the diamagnetic energy measurement at TEXTOR with a short presentation of corrections to be done and a discussion of the error sources are given. The principles of diamagnetic measurements are explained in section 5.1, and the experimental setup is described in section 5.2. The corrections done are presented in section 5.3, and the validity of the diamagnetic measurement is discussed in section 5.4.

5.1 Principles of diamagnetic energy measurements

5.1.1 Diamagnetic and paramagnetic effects

The currents in a magnetized plasma in a tokamak have two origins: external coils, and the Larmor gyration of charged particles. The plasma current induced in the toroidal direction produces a poloidal magnetic field, which twists the magnetic field lines as explained in section 2.1 (see figures 2.1 and 2.2). The magnetic pressure balance shows that due to this component, the toroidal magnetic field on the torus axis is larger than the value it would take in absence of plasma current. This is the "paramagnetic effect" due to the current flowing in the plasma. Conversely, the Larmor gyration of the particles has a diamagnetic effect. The induced decrease in the toroidal field is proportional to the density of particles, and to their temperature[1]. Hence, if paramagnetic and diamagnetic contributions can be distinguished, the product nT, with $T = T_e + T_i$, can be obtained from a measure of the difference between magnetic fluxes with and without plasma.

5.1.2 Difference between total plasma energy content and diamagnetic energy

The term *total plasma energy content* refers to the sum of the kinetic energy of all particles in the plasma. For a maxwellian velocity distribution, the average energy E_{av} per particle along a given direction d is $E_{av,d} = k_B T_d/2$, where T_d is the temperature in this direction, expressed in eV, and k_B is the Boltzmann constant. Under some conditions, for instance with a high auxiliary heating, the plasma temperature can be anisotropic. In this case, $T_\parallel \neq T_\perp$, with $T_\parallel$ and $T_\perp$ the temperatures in the directions parallel and perpendicular to the magnetic field. The total plasma energy content W_{tot} is then

$$W_{tot} = \frac{1}{2} k_B n T_\parallel + k_B n T_\perp. \tag{5.1}$$

Diamagnetic measurements are sensitive to the perpendicular motion of the particles only, i.e. they can provide the product $nT_\perp$, but cannot give information on $T_\parallel$. The diamagnetic energy W_{dia} is computed according to

$$W_{dia} = \frac{3}{2} k_B n T_\perp, \tag{5.2}$$

i.e. it is equal to the total plasma energy content provided parallel and perpendicular temperatures are equal. Diamagnetic energy and total plasma

[1]The magnetic flux produced by the Larmor gyration of a particle is proportional to the current induced by the motion of this particle, and to the area delimited by its trajectory. The current is proportional to the gyration (cyclotron) frequency and the charge of the particle, and the area it delimits is proportional to the square of its Larmor radius. Since the cyclotron frequency does not depend on the temperature, and since the Larmor radius is proportional to the square root of the temperature, the magnetic flux induced by particles is proportional to their temperature.

energy are thus equal only if the plasma is isotropic. Note that in the case where the velocity distribution is not Maxwellian, the temperature cannot be defined (or is defined on another way), but a measurement of diamagnetism still provides the energy in the perpendicular direction. Diamagnetic energy measurements are thus not sensitive to the parallel velocity distribution.

5.2 Description of the measurement

As mentioned in section 5.1, the determination of the diamagnetic energy is based on a measurement of the difference between the toroidal fluxes with and without plasma. In section 5.2.1, the way to perform this measurement is explained, and corrections to be done to it are presented in section 5.3. Then, the method used to distinguish between diamagnetic and paramagnetic fluxes is presented in section 5.2.2, together with the calculation leading to the diamagnetic energy.

5.2.1 Experimental set-up

There are two[2] independent systems of diamagnetic loops at TEXTOR. Each of them is made up of a pair of magnetic flux loops: one inner loop measuring the toroidal flux in the plasma and one outer loop measuring the flux in the vacuum around the plasma. The outer loop is asymmetrical in the poloidal direction in order to take into account the variation of the vacuum magnetic field with R, see fig. 5.1. The voltage ΔV induced in a loop is proportional the time derivative of the flux crossing this loop, and can be written:

$$\Delta V = -N \int_S \frac{\partial \boldsymbol{B}}{\partial t} \cdot \boldsymbol{ds} \tag{5.3}$$

where S is the area of the loop, $\boldsymbol{ds}$ is the unit vector perpendicular to this surface, and N is the number of wire turns of the loop. A time integration of ΔV gives the magnetic flux crossing the loop, provided this integration is started when $B = 0$. Since the difference $\Delta\Phi$ between the fluxes inside and outside of the plasma is sought, the voltages from both loops are subtracted before integration. The subtraction is performed in an adjustable resistor bridge, which allows to correct for the small difference of area of both loops. The adjustment is such that the voltage difference is zero in a magnetic field without plasma. Some details of the data acquisition chain are shown in fig. 5.2.

[2]For a long time, only one system could be used since a wire of the other system had been replaced by heating wire. This led to impedance problems, and has been solved only

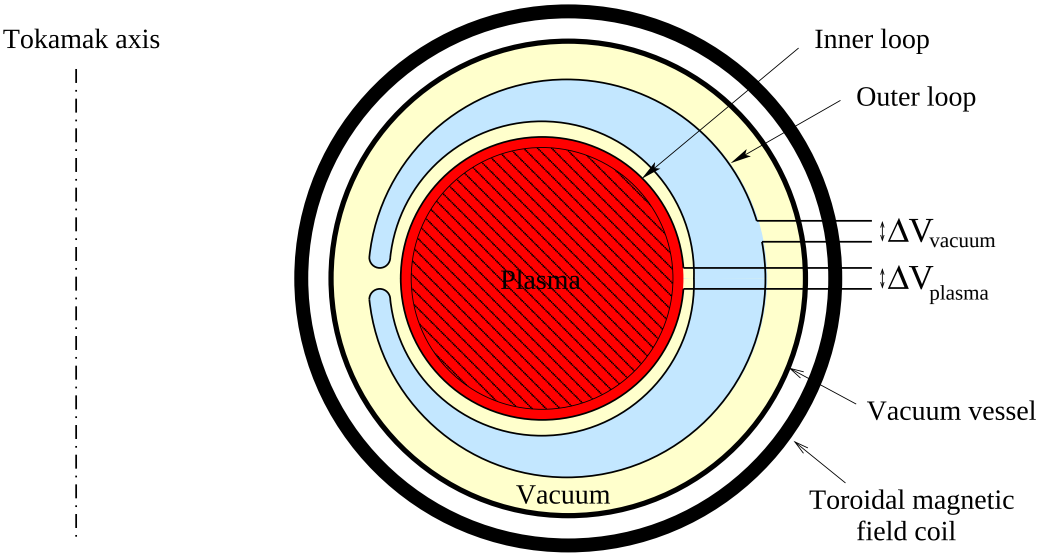

Figure 5.1: A pair of diamagnetic loops in a poloidal cross section of TEXTOR. The plasma (hatched region) is located in the vacuum chamber (yellow region), which is surrounded by toroidal magnetic field coils. The inner loop measures the toroidal magnetic flux in the plasma (red region), while the outer one measures the flux around the plasma (blue region).

5.2.2 Separation between diamagnetic and paramagnetic fluxes

In the previous section, it was shown how to measure $\Delta\Phi$, the sum of the paramagnetic and diamagnetic fluxes over the plasma cross section. In the present section, the contributions from this two fluxes are separated according to the approach of ref. [29], under the assumption of a cylindrical geometry. The diamagnetic energy is then calculated. From the equilibrium equation (2.4), one has

$$\frac{dp}{dr} = -\frac{dB_\varphi}{dr}\frac{B_\varphi}{\mu_0} - \frac{1}{r}\frac{d\,(rB_\theta)}{dr}\frac{B_\theta}{\mu_0}. \tag{5.4}$$

some months ago.

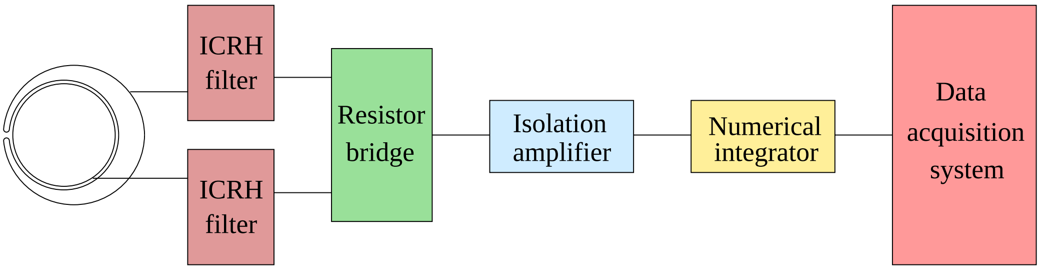

Figure 5.2: Data acquisition chain for the diamagnetic energy measurement at TEXTOR. The signals from the diamagnetic loops are first filtered in order to eliminate interferences from Ion Cyclotron Resonant Heating (ICRH). The signals are then subtracted in a resistor bridge. Before integration, the signal coming out of the bridge goes through an isolation amplifier, which protects the electronic devices from high voltage peaks occurring during plasma shot disruptions. The integrated signal is finally sampled and stored by the data acquisition system.

By multiplying this equation by r^2 and integrating from $r = 0$ to $r = a$, with a the plasma radius, one obtains

$$\begin{aligned}
\int_0^a \frac{dp}{dr} r^2 dr &= \left[pr^2\right]_0^a - \int_0^a 2p\, r dr = -\langle p\rangle\, a^2 \\
&= -\frac{1}{\mu_0}\int_0^a \frac{dB_\varphi}{dr} B_\varphi r^2 dr - \frac{1}{\mu_0}\int_0^a \frac{d\left(rB_\theta\right)}{dr} B_\theta r dr \\
&= -\frac{1}{\mu_0}\left[\frac{B_\varphi^2}{2} r^2\right]_0^a + \frac{1}{\mu_0}\int_0^a \frac{B_\varphi^2}{2} 2r dr - \frac{1}{\mu_0}\left[\frac{\left(rB_\theta\right)^2}{2}\right]_0^a \\
&= -\frac{B_{\varphi a}^2 a^2}{2\mu_0} + \frac{\left\langle B_\varphi^2\right\rangle a^2}{2\mu_0} - \frac{B_{\theta a}^2 a^2}{2\mu_0},
\end{aligned} \tag{5.5}$$

where $\langle\,\rangle$ denotes an average over a poloidal cross section of the plasma, and $B_{\varphi a}$ and $B_{\theta a}$ are the values of the toroidal and poloidal magnetic field at radius $r = a$. This result can be rewritten by using the so-called poloidal beta, β_p, which is the ratio of the kinetic and magnetic pressures:

$$\beta_p = \frac{\langle p\rangle}{B_{\theta a}^2/2\mu_0} = 1 + \frac{B_{\varphi a}^2 - \left\langle B_\varphi^2\right\rangle}{B_{\theta a}^2} \tag{5.6}$$

The mean value of the toroidal field can be evaluated as follows:

$$\begin{aligned}
\left\langle B_\varphi^2\right\rangle &= \left\langle \left(B_{\varphi a} + \delta B_\varphi\right)^2\right\rangle \\
&\approx \left\langle B_{\varphi a}^2 + 2B_{\varphi a}\delta B_\varphi\right\rangle \\
&= B_{\varphi a}^2 + 2B_{\varphi a}\left\langle \delta B_\varphi\right\rangle
\end{aligned} \tag{5.7}$$

where δB_φ is the variation of the toroidal magnetic field caused by the plasma. Its average value is related to the measured flux difference by

$\langle \delta B_\varphi \rangle = \Delta\Phi/(\pi a^2)$. In the second step, the smallness of the ratio $\langle \delta B_\varphi \rangle / B_{\varphi a}$, being typically of order of 10^{-3}, has been used. The poloidal magnetic field is produced by the toroidal electric current. This allows to calculate $B_{\theta a}$:

$$B_{\theta a} = \frac{\mu_0}{2\pi a} \int_0^{2\pi} \int_0^a j_\varphi(r) r dr d\theta = \frac{\mu_0}{2\pi a} I_\varphi \tag{5.8}$$

where j_φ is the toroidal electric current density, and I_φ is the current induced in the plasma. By combining equations (5.6), (5.7) and (5.8), one gets

$$\beta_p = 1 - \frac{8\pi B_{\varphi a}}{\mu_0^2 I_\varphi^2} \Delta\Phi. \tag{5.9}$$

Since the calculations of this section were made for a cylindrical geometry, the meaning of $B_{\varphi a}$ is clear. In a toroidal geometry, $B_{\varphi a}$ depends on the poloidal angle. Its value is taken on the plasma axis, i.e. $B_{\varphi a} = B_{\varphi a}(R_*)$. This value and the plasma current I_φ are given by other TEXTOR diagnostics. Finally, the diamagnetic energy is calculated. According to equation (5.2), it is

$$\begin{aligned} W_{dia} =& \frac{3}{2} k_B \langle p \rangle V \\ =& \frac{3}{2} k_B \frac{\beta_p B_{\theta a}^2}{2\mu_0} 2\pi R_* \pi a^2 \\ =& \frac{3}{8} k_B \mu_0 R_* I_\varphi^2 \left(1 - \frac{8\pi B}{\mu_0^2 I_\varphi^2} \Delta\Phi\right) \end{aligned} \tag{5.10}$$

where V is the plasma volume.

5.3 Corrections to apply to the measurement

Since the relative variation of the magnetic field due to the plasma is very small, namely about 10^{-3}, a great care must be taken in order to achieve a reasonable precision in the measurements. In particular, the inner and outer loops are not perfectly aligned vertically and they both catch a small fraction of the positioning magnetic fields, this fraction being slightly different for each loop. The correction for this misalignment is performed by measuring for each positioning field separately the flux produced in the loops without plasma. The proportionality coefficient between the positioning field and the $\Delta\Phi$ it produces is then deduced, allowing for a correction of $\Delta\Phi$ for experiments with plasma. This leads to a correction of the diamagnetic energy by $10 - 20\,\%$.

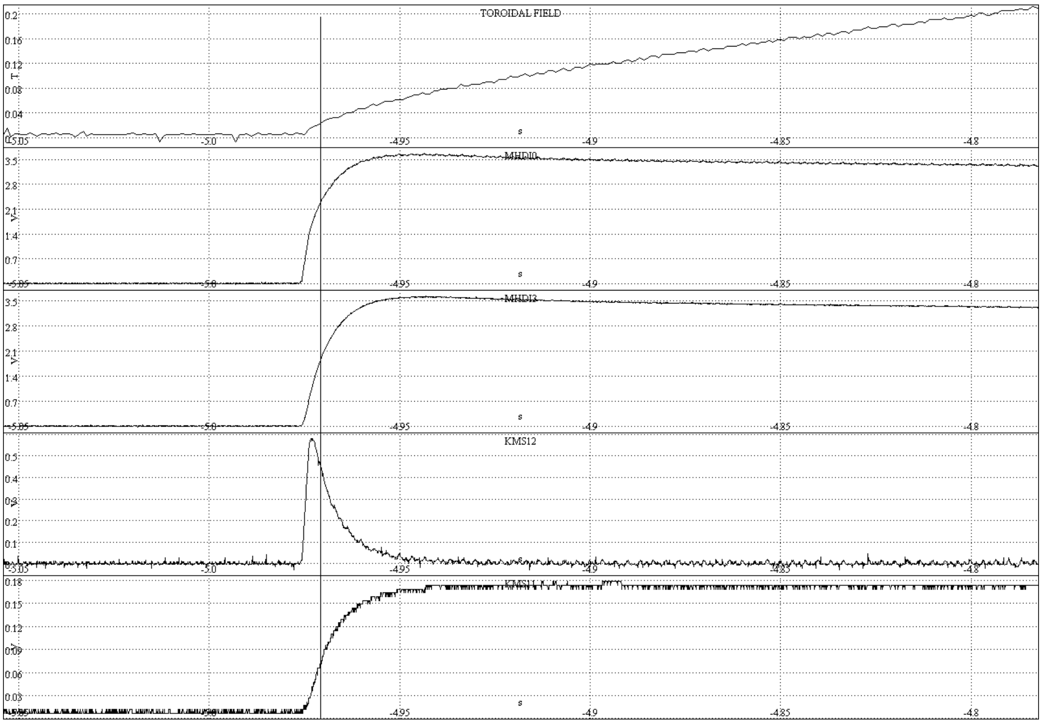

Figure 5.3: From the top to the bottom: the rise of the toroidal magnetic field, the voltages it induces in the inner and outer diamagnetic loops, the difference between these two voltages, and the integration of this voltage difference. The voltages induced in both loops do not increase at the same speed. Indeed, though they come to the same level after about $25\,ms$, the upper signal reaches $2.2\,V$ at $t = -4.97\,s$ (vertical line), while the lower one reaches only $1.8\,V$ at this time.

Another perturbation of the measurement which had not been recognized before comes from the difference in response time of both loops. Figure 5.3 shows the rise of the magnetic field with the voltage it induces in each loop and the $\Delta\Phi$ it produces. One can see that the induced voltages ΔV are approximately in the form $\Delta V = V_f\,(1 - \exp(t/\tau))$, where V_f is the final voltage reached. This corresponds to RL electric circuits, with a rise time τ. However, this rise time is different for each loop. Using the definition according to which the rise time is the time needed to reach 63 % of the final stationary value, one obtains $\tau = 5.1\,ms$ for one loop, and $\tau = 6.9\,ms$ for the other loop. Though the final voltage induced in each loop is the same, these voltages differ during the $25\,ms$ of the rising phase. The integration of this difference results in a non zero $\Delta\Phi$, even though there is no plasma. For the shot of fig. 5.3, this leads to a flux of 1 mWb, while the total flux due to the plasma is 2.7 mWb. The way this effect has been corrected is detailed in appendix H. Note that it has no influence when the magnetic field does not vary during the phase with plasma, since only the variations of the flux during this phase are taken into account for the calculation of the energy.

Finally, a drift of the integrated signal is observed, i.e. the signal shows a constant increase (or decrease in some cases) when all plasma parameters are constant in time. This drift varies from shot to shot. The origin of this problem, which was already observed before the installation of the DED, has been searched for, but without success. The only clue which has been found results from the integration of the signal at the same time by analogic and numerical integrators. Both integrators show the same drift, indicating that the drift corresponds to the integration of an offset, whose origin lies before the integrator in the data acquisition chain. A correction is applied to remove the effect of the drift: the value of the drift is calculated on the base of the values of $\Delta\Phi$ at the beginning and at the end of the plasma phase, and the obtained slope is subtracted from the integrated signal.

5.4 Validity of the measurement

A precise estimation of the error on the diamagnetic energy measurement would require a deep analysis and is out of the scope of the present work. Instead of this, the error sources are listed and discussed.

First, the cylindrical geometry assumption introduces some errors. The evaluation of this error would require the resolution of equation (5.4) in a toroidal geometry, taking the Shafranov shift $\Delta(r)$ introduced in section 2.1 into account [31, 54]. According to the calculation performed in ref. [54], the main correction to the poloidal beta would be the subtraction of a term of order $\Delta(0)/R_*$ for low β_p values, and of order $\Delta(0)/a$ for large β_p values. By neglecting this correction, an overestimation of the energy is made. This results in error lower than 15 % in all cases.

Secondly, the measuring devices introduce an error in the measurement. A rigorous estimation of this error is practically impossible since technical data sheets are available for only parts of the measuring devices, and in the available ones, the error is not specified. However, a qualitative analysis can be performed. The ICRH filters are made of selfs and capacitors and operate in the tenth of MHz range, such that they are expected to cause a negligible distortion of the signal in the range of characteristic diamagnetic energy variation times. The resistor bridge should also have a negligible impact on the measurement since it is adjusted manually to cancel the output signal in the absence of plasma. The isolation amplifier is a high-quality one and is expected to cause a very small perturbation of the signal. The data acquisition system works with a 12-bits AC/DC converter and the signal generally reaches one tenth of its input range. Under the assumption that the error is one half of the least significant bit, this leads to a relative error of about $2.5 \cdot 10^{-3}$ during the digitization process. The most delicate operation is the integration, since errors are integrated. These errors are of two kinds: the error produced by the measuring devices before integration, and the error caused by the digitization of the signal in the integrator. By performing the integration simultaneously with a analog integrator, it has been checked that the latter error source is not significant. The first one could not be investigated since the isolation amplifier cannot be removed (it protects the other devices from high voltage peaks), but for the reasons mentioned above it is not expected to lead to a significant error. The cylindrical geometry assumption leads very likely to a much larger error.

Thirdly, the DED is located very close to the diamagnetic loops. It can influence the flux measurement by magnetic induction if the sum of the currents in the DED coils is not zero (it should theoretically be, but the relative phase of the currents in the coils could be slightly different from what is programmed). This effect was investigated by performing flux measurements with DED and without plasma. For the DC operation of the DED, it has been seen that the influence is moderate. In the worst case, a variation of $2 \cdot 10^{-2}$ mWb was observed, to be compared with the typical value of 2 mWb measured for $\Delta\Phi$. For operation of the DED at high frequencies, it seems no rule can be extracted out of the measurements performed. These measurements are summarized in table 5.1 and show both a drift and an oscillation of $\Delta\Phi$. The amplitude of oscillations is weak compared to the typical value of $\Delta\Phi$ and should not lead to problems for the interpretation of diamagnetic energy measurements. The drift is more embarrassing. However, since it

Shot number #	Frequency (kHz)	Drift (mWb/s)	Oscillations (mWb/kA DED)	DED mode M/N
94410	1	$2.5 \cdot 10^{-2}$	$1.7 \cdot 10^{-2}$	3/1
95732	1	0	0	12/4
95741	1.875	$7 \cdot 10^{-2}$	$8 \cdot 10^{-4}$	12/4
95742	1.875	$1.4 \cdot 10^{-2}$	$8 \cdot 10^{-4}$	12/4
94405	3.75	$2.5 \cdot 10^{-2}$	0	3/1

Table 5.1: Oscillations and drift of $\Delta\Phi$ with DED operated at different frequencies and modes without plasma.

is a slow drift, the following conclusions are drawn: fast variations of the diamagnetic energy can be interpreted as being real effects on the plasma, but small drifts have probably no physical meaning, and should be treated carefully.

Finally, the measurements have been compared with the scaling laws of ref. [69]. These laws characterize the performances obtained in a series of tokamaks by the product of the dimensions and typical plasma parameters of these machines elevated at certain powers, these powers being determined by fitting methods. There is thus a priori no physics contained in these relations, but they provide a good agreement with the observations and are used to predict performances of future machines. The comparison of the measurements performed at TEXTOR show a fair agreement with scaling laws. This does not prove that the measurements are reliable, but confidence is gained from this comparison.

From the previous discussions, a conservative upper limit of 20 % of error on the absolute value of W_{dia} is estimated. However, since the error from the cylindrical geometry assumption always leads to an overestimation of the energy, the error made by comparing the diamagnetic energy from different discharges should be smaller. For experiments with DED, fast changes can be regarded as physically meaningful, while slow variations should be treated with care, they are probably due to pick-up from the DED coils. Finally, diamagnetic energy measurements should always be compared with density and temperature measurements in order to see whether they show similar behaviors.

The measured diamagnetic energy will be compared in chapter 6 with the predictions from the modelling of the plasma parameter profiles with the code RITM.

Chapter 6

Results of calculations and comparison with experiment

Calculations of transport coefficients for experimental conditions at the tokamak Tore Supra, France, have been performed with the transport model described in chapters 2 and 3, and are compared with the expriment in section 6.1. In section 6.2, predictive calculations for the H-mode power threshold at TEXTOR made with RITM are presented. In sections 6.3 and 6.4, simulations of respectively an ohmic and an auxiliary heated discharge at TEXTOR are discussed and compared with experiment. These simulations were done with RITM and the models of chapters 2 and 3, without and with DED.

6.1 Calculations for Tore Supra with ED

In the tokamak Tore Supra, an ED has been in operation for several years. It consists of a set of six octopolar coils evenly spaced toroidally [22], located on the low field side of the torus. At full current, the ratio of the amplitudes of perturbation and toroidal magnetic fields is about 10^{-3} in the vicinity of the (destroyed) resonant magnetic surface.

Stochastization of the magnetic field at the edge by an ED was expected to allow radial transport along the field lines, and hence to increase radial transport. However, measurements give indication [22, 48] for a decrease of heat transport during ED operation in the region around $r \approx 0.85\,a$, with a the plasma radius. The models developed in chapters 2 and 3 have been applied in this region in order to see whether the decrease of transport can be reproduced. The comparison with experimental data was performed by computing transport coefficients according to these models with the experimental pa-

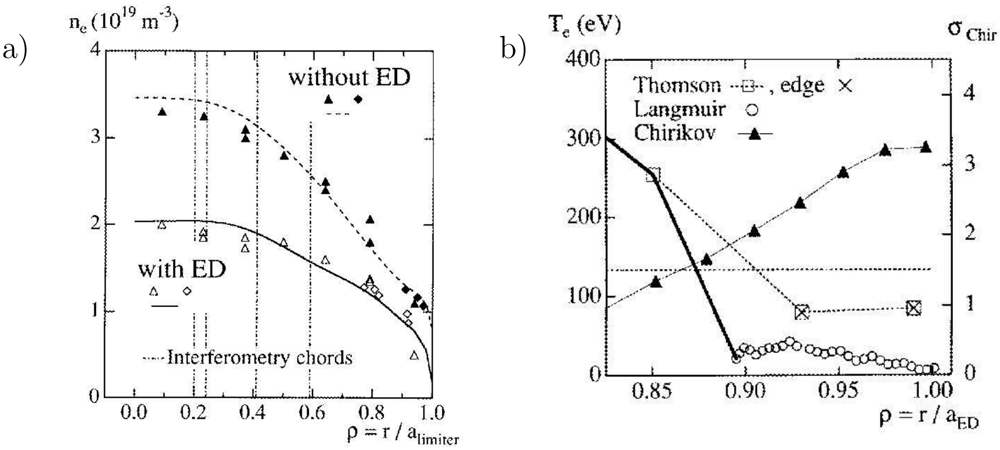

Figure 6.1: a) Electron density profiles without and with ED at Tore Supra, and b) electron temperature (left axis) with ED measured by Thomson scattering, open squares, and by reciprocating Langmuir probes, open circles. The Chirikov parameter profile is represented with full triangles (right axis). The plasma radii with limiter and with ED are both approximately equal to 80 cm. Source: figures 15 and 42 of reference [21].

rameters taken at $r = 0.87\,a$[1]. The electron density and temperature profiles are taken respectively from figure 42 and 15 of reference [21], and are reproduced in figure 6.1. From figure 6.1.a, one has $n \approx 1.3 \cdot 10^{19}\,\mathrm{m}^{-3}$, $L_n \approx 35\,\mathrm{cm}$ in the limiter case (without ED), and $n \approx 10^{19}\,\mathrm{m}^{-3}$, $L_n \approx 27\,\mathrm{cm}$ with ED. For temperature, things are a bit more delicate. Figure 6.1.b shows two temperature profiles from different diagnostics, both with ED in operation. In reference [48] temperature profiles without and with ED are compared but the Chirikov parameter is not given. By comparing the temperature profiles shown in fig. 6.1.b with the ones in figs. 2 and 3 from reference [48], one can see that the lower temperature profile (by Langmuir probes) in fig. 6.1.b corresponds to the case with stochastization, while the upper one (by Thomson scattering) is close to the temperature profile without ED. Therefore, the temperature and temperature gradient for the calculation of effective transport coefficients are taken from the upper profile of fig. 6.1.b in the limiter case, and from the bottom profile in the ED case. For the position $r = 0.87\,a$, this provides $T_e = 205\,\mathrm{eV}$, $L_{T_e} = 7\,\mathrm{cm}$ for the limiter case, and $T_e = 135\,\mathrm{eV}$, $L_{T_e} = 2.5\,\mathrm{cm}$ for the case with ED. $T_i \approx T_e$ and $L_\phi = \infty$ are assumed in the calculations. From figure 5 in reference [21] which shows the relation between the field line diffusivity and σ_{ch}, one deduces $D_{Fl} = 6.3 \cdot 10^{-6}\,\mathrm{m}$. The Kol-

[1]In figures 6.1.a and 6.1.b, the normalized minor radius, $\rho = r/a$ is defined with respect to different a, namely a_{ED} and $a_{Limiter}$. Since they are close to each other, they are assumed to be identical $a_{ED} \approx a_{Limiter} \approx a = 80\,\mathrm{cm}$.

mogorv length is calculated according to the quasi-linear approximation [21]:

$$L_K = \pi q R_0 \left(\frac{\pi \sigma_{ch}}{2}\right)^{-4/3} . \qquad (6.1)$$

Computed anomalous and effective transport coefficients are shown in figures 6.2 and 6.3 as a function of σ_{ch}. The dependence of the field line diffusivity on σ_{ch} follows from the quasi-linear scaling $D_{Fl} \sim \sigma_{ch}^4$, see section 2.2.3. For the density, the temperature and their e-folding length, the following linear dependence on σ_{ch} is assumed

$$f_j\left(\sigma_{ch}\right) = f_j^{Lim} + \left(f_j^{ED} - f_j^{Lim}\right) \frac{\sigma_{ch} - 1}{\sigma_{ch}^{ED} - 1} \qquad (6.2)$$

where f_j^{Lim} and f_f^{ED} are the values of the considered parameter f_j for $\sigma_{ch} = 1$ and $\sigma_{ch} = \sigma_{ch}^{ED}$, respectively, $\sigma_{ch} = 1$ corresponding to the limiter case (at the limit of stochastization), and $\sigma_{ch}^{ED} \approx 1.6$ being the value of σ_{ch} with ED, at $r = 0.87\,$a (see figure 6.1.b). This assumption is arbitrary, but allows a smooth transition between the perturbed and unperturbed situations.

One can see in figs. 6.2 and 6.3 that effective transport coefficients are strongly reduced under ED conditions. This in qualitative agreement with the steepening of the temperature gradient observed with ED. For density, comparisons are more difficult to make since modifications of the recycling with ED can considerably affect the density profile at the edge. From a comparison between figs. 6.2.a and 6.2.b where transport coefficients are calculated on the basis of the zeroth and the second order eigenfunctions of the dispersion relation (3.48), it is clear that the zeroth order solution largely dominates transport. There is a small difference between the effective and anomalous particle diffusivities, but no significant difference is seen between effective and anomalous heat conductivities. The influence of the term $\nu_{\|}$ in equation (3.32) has been investigated, but no noticeable change is produced by this term.

In order to determine the reason for the drop of transport coefficients, the density, the temperature and their e-folding length have been one by one kept constant by setting them to their limiter value, the other parameters being computed according to equation (6.2). This shows, see figs. 6.2 and 6.3, that a decrease of T_e or L_{T_e} leads to a decrease of transport coefficients, while a decrease of L_n results in an increase of the latter ones. The small variation of the density does not much influence transport. The decrease due to the temperature can be explained by the fact that the gyro-Bohm diffusion coefficient D_{gB} (see equation 3.56), which gives the order of magnitude of the diffusion coefficient from drift instabilities, is proportional to $T^{1.5}$. Similarly, the increase observed when the density e-folding length diminishes is

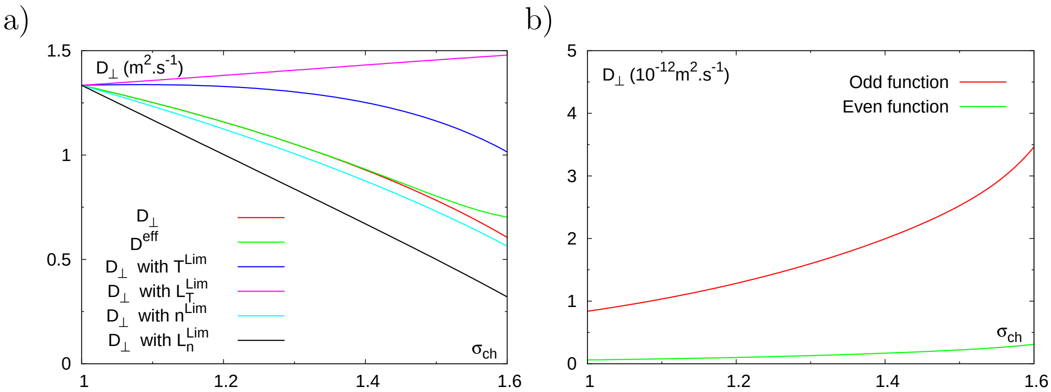

Figure 6.2: Particle diffusivities calculated on the basis of the a) zeroth and b) second order eigenfunctions of the dispersion relation (3.48) as a function of σ_{ch}. The different parameters are taken from fig. 6.1 at the position r=0.87 a. For the zeroth order, the effective and anomlous particle diffusivities are shown. Additionally, curves with all density and temperature parameters calculated according to relation (6.2), except for one of them, which is assessed to have the value under the limiter conditions, are shown: for the dark blue, the magenta, the cyan and the black curves, respectively the temperature, the temperature e-folding length, the density and the density e-folding length are set to the limiter value. For the second order, only the effective diffusivities are shown. Note the large difference of amplitude between figures a) and b).

mainly due to the inverse propotionality of D_{gB} to L_n. As to the decrease of $D_\perp$ and $\kappa_\perp$ with the decrease of L_{T_e}, it is the result of the rise of the term proportional to $\widetilde{B}_r/L_{p_e}$ in equation (3.36), which stabilizes drift-Alfvèn modes.

To sum up, comparisons of the transport models developed in chapters 2 and 3 with Tore Supra experiments, without and with DED, show a qualitative agreement with the observed temperature decrease around the position $r \approx 0.87\,a$. From the considerations of the last paragraph, the cooling of the edge, leading to a decrease of the gyro-Bohm coefficient and a reduction of the amplitude of the drift-Alfvèn modes, is proposed as an explanation for the reduction of transport observed in Tore Supra at $r \approx 0.87\,a$ with ED.

6.2 H-mode power threshold in TEXTOR

An abrupt change from a low (L-mode) to a high (H-mode) energy confinement mode has been observed in several tokamaks when the heating power exceeds a critical level [67]. A multi-machine scaling for this L-H transition was established in reference [55] by an analysis of experimental data from a series of divertor tokamaks. This scaling predicts that an L-H transition

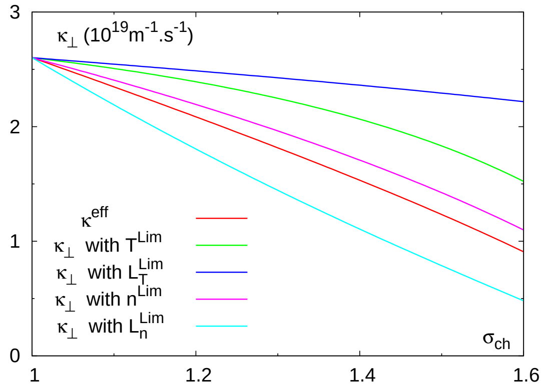

Figure 6.3: Heat conductivities calculated on the basis of the zeroth eigenfunction of the dispersion relation (3.48) as a function of σ_{ch}. The same assumptions as in fig. 6.2 are made, but in this case, there is no (visible) difference between the anomalous and effective values

takes place when the power loss, P_L, exceeds the threshold value:

$$P_{th} = 0.042 \bar{n}_e^{0.64} B^{0.78} S^{0.94} \tag{6.3}$$

where P_{th} is expressed in megawatts, $\bar{n}_e$ is the line averaged density in $10^{20}\, m^{-3}$, S is the plasma area in m^2 and B is the toroidal magnetic field in T. The power loss P_L is the sum of the ohmic and auxiliary heating powers, from which the time derivative of the plasma energy content is subtracted.

The value of the heating power necessary to obtain an H-mode is much higher in limiter tokamaks than predicted by P_{th} [30]. In order to see whether and for which conditions an H-mode could be achieved in TEXTOR, calculations were performed with RITM [36], using transport model B. The criterium used in these calculations to determine the transition from L- to H-mode is the appearance of so-called Edge Localized Modes (ELMs). These modes are characterized by repetitive huge increases of heat and particle transport towards the edge during very short times. They are destabilized by a high pressure gradient and are often observed during H-modes. In reference [46], a criterium for the appearance of the most common type of ELMs, namely type I ELMs, is established by comparison of the threshold for these modes in different tokamaks. According to this criterium, one can expect ELMs when the normalized pressure gradient $\alpha = 8\pi R q^2 \left| dp/dr \right| / B^2$ exceeds the ballooning limit, given by $\alpha_{cr} = 0.8 r \partial \ln q / \partial r$. Calculations were performed for TEXTOR plasmas with this criterium for the L-H transition, under conditions of a line averaged density of $2 \cdot 10^{19}\, m^{-3}$ and an edge safety factor of 3, for different values of the toroidal magnetic field. The obtained power thresholds for the L-H transition are shown in fig. 6.4,

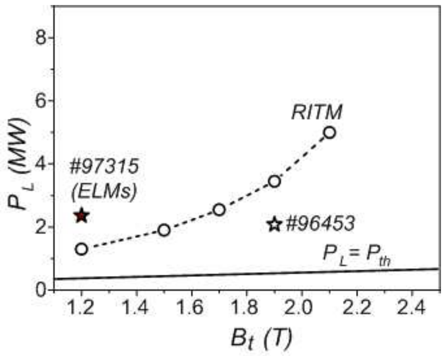

Figure 6.4: Threshold power for L-H transition computed with RITM for TEXTOR (open circles) and according to the multi-scaling law of equation (6.3) (plain curve). The two stars correspond to two TEXTOR discharges with strong auxiliary heating power, which were performed after calculation of the L-H transition power threshold.

toghether with the power threshold of equation (6.3). This shows that the threshold estimated from RITM calculations is much higher than the one from equation (6.3) and that it strongly increases with the magnetic field.

Discharges with a low toroidal magnetic field (less than 1.9 T) and strong auxiliary heating were performed later at TEXTOR with the purpose of achieving an H-mode. Among these, some discharges with a magnetic field of 1.2 T, the lowest ever used at TEXTOR, have shown typical signatures of H-modes. The points corresponding to two discharges performed with a strong auxiliary heating and a line average density of $2 \cdot 10^{19}\, m^{-3}$ are plotted in fig. 6.4. The one operated at a magnetic field of 1.2 T showed ELM signatures, while the other one, operated at 1.9 T, did not exhibit ELMs. This observation is in agreement with the H-mode power threshold calculated with RITM. Since these calculations were performed before any ELM has been observed at TEXTOR, they have predicted the H-mode power threshold for TEXTOR. Simulations for discharge 97315, for which ELMs were observed, are under progress.

6.3 Ohmic discharge in 3/1 DED configuration

The ohmic discharge 98358 at TEXTOR has been simulated [40] with RITM with transport model A, before and during the DED (3/1 mode) phase. The experimental time traces of the plasma current, the line average density, the DED current and the diamagnetic energy are shown in fig. 6.5. The value of the toroidal magnetic field was 2.25 T and remained constant during the

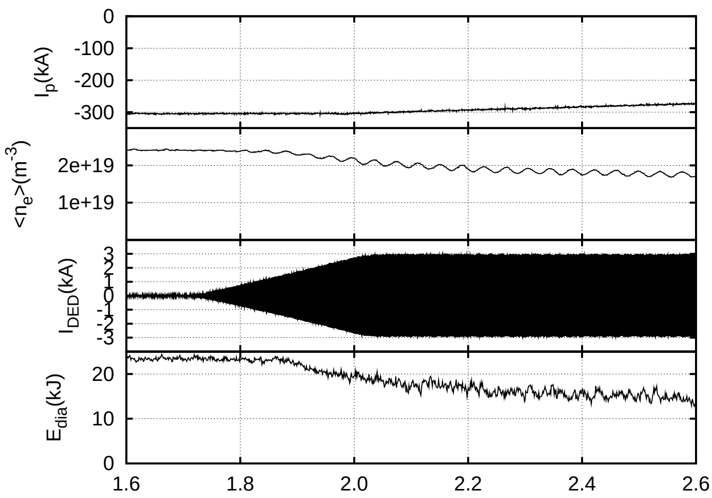

Figure 6.5: Time traces of, from the top to the bottom, the plasma current, line average density, DED current (1 kHz) and diamagnetic energy for TEXTOR discharge 98358.

whole discharge. Simulations of the plasma parameters have been performed for $t = 1.6$ s without DED and for $t = 2.05$ s with DED. The stochastization parameters required by the transport model, D_{Fl}, L_K and σ_{ch}, were taken from field line mapping and are plotted in fig. 6.6. As already mentioned, only static perturbations from the DED are taken into account in the present model, such that these parameters are computed for a static DED current of 3 kA. Since they are sensititve to the safety factor profile, which depends on the plasma current, and since the latter varies during the DED phase, the profiles shown in fig. 6.6 are valid only for the time at which they were calculated ($t = 2.05\,s$). The simulated and measured density and temperature profiles are presented in fig. 6.7. Two kinds of simulations for the DED phase are presented: one simulation where the gas puffing rate and the recycling coefficient were kept the same as withtout DED, and two where the gas puffing was adapted in order to match the measured line averaged density, the recycling coefficient being kept constant. The two latter simulations differ from each through the parameter γ_v, the ratio of the heat carrying particle velocity to the thermal velocity, see section 2.3.1. The particle diffusivities and fluxes without and with DED are presented in figs. 6.8 and 6.9. For the case with DED, they correspond to the simulation with adjusted gas puff and with $\gamma_v = 3$.

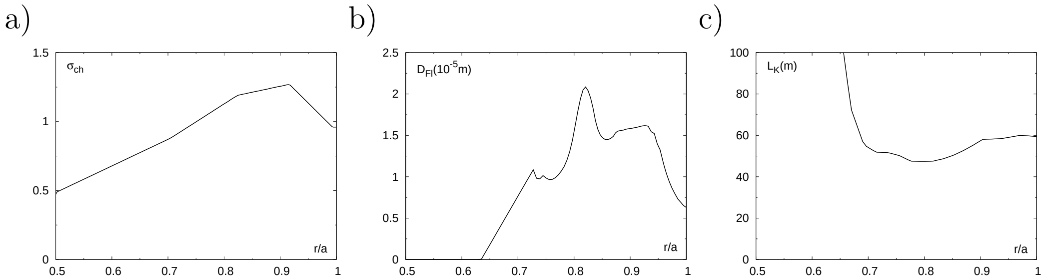

Figure 6.6: Stochastic parameters computed from field mapping for TEXTOR discharge 98358 versus the normalized radius r/a at time $t = 2.05$ s. a) shows the Chirikov parameter, b), the field field line diffusivity and c), the Kolmogorov length.

6.3.1 Phase without DED

A good reproduction of the density profile has been achieved (see fig. 6.7). For this, the free parameter α_T (eq (4.17)) is set to 0.1, and the weight f_{DA} of the DA contribution has to be adjusted by taking it equal to $1/3(r/a)^2$. This adjustement of the DA contribution is legitimate since the theory does not predict the absolute level of the anomalous transport contributions with a high accuracy. Without this factor, the DA transport is too strong in the plasma centre, what is usually not expected from DA modes, and the density profile is too flat compared with the experimental one. Such flatness may be, however, explained by the neglecting of the pinch-velocity contribution from DA modes. This contribution has not been explored up to now theoretically.

It was not possible to reproduce the experimental electron temperature profile measured by Electron Cyclotron Emission (ECE) [67] with a desired accuracy by tuning the weights of the different transport contributions in the heat conductivity in a reasonable range. This, nevertheless, does not mean definitely that the model is not good enough. There are in fact at least three possibilities to validate the heat transport model, by comparing i) the calculated profile with the profile measured by ECE, ii) the central temperatures obtained from the RITM calculations and from He-like spectra of Argon [4], or iii) the calculated and measured diamagnetic energies. From He-like spectra one gets a central electron temperature of $1.13\,keV$, against $1.28\,keV$ from ECE measurement and $0.84\,keV$ from RITM simulations. Though the ECE and He-like spectra measurements differ by 12 %, they seem to indicate that the temperature obtained from the simulation is too low. However, the diamagnetic energy obtained from the simulation (27.6 kJ) is still larger than the measured one (23.4 kJ). Note that the errors on the temperature given by ECE, by He-like spectra of Argon and by diamagnetic loops are respectively of the order of 10 %, 15 % and 20 %. For the latter, the largest error

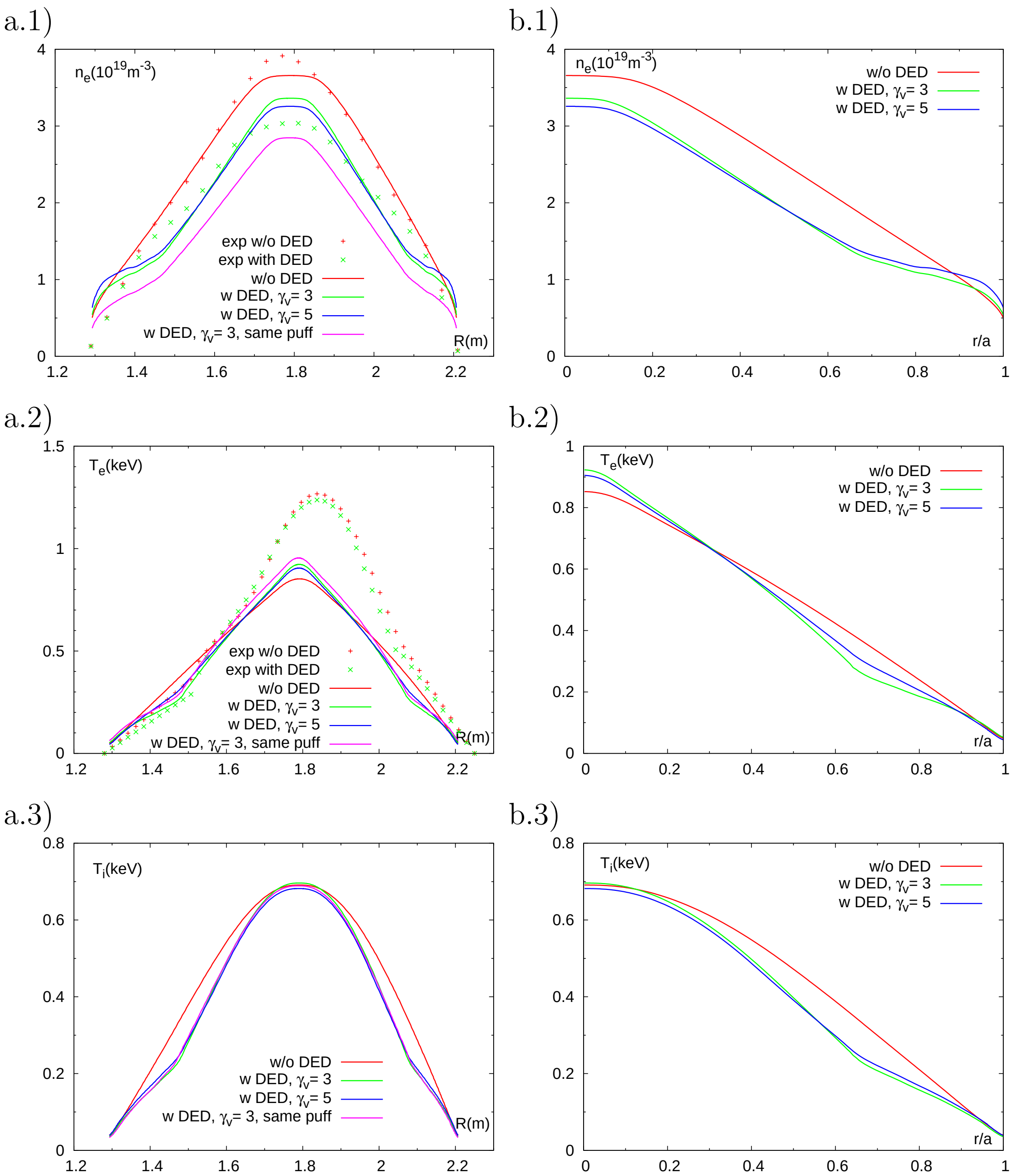

Figure 6.7: a) Profiles of different simulated (solid curves) and experimentally measured (crosses) quantities versus the tokamak major radius for discharge 98358 at TEXTOR, with and without DED: a.1) electron density, a.2) electron temperature and a.3) ion temperature. For each quantity, four profiles from simulations are shown: one for the phase before DED, one for the phase with DED with the same gas puffing rate and recycling coefficient as used in the simulation of the phase before DED, and two for the DED phase with gas puffing rate adjusted in order to match the experimental line averaged density. The latter two differ through γ_v, the ratio of heat carrying and thermal particle velocities. b) The simulated profiles plotted versus the reduced minor radius r/a.

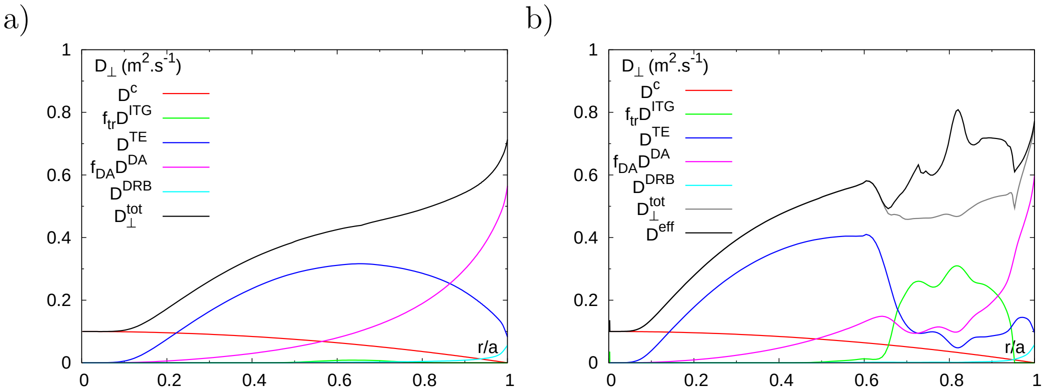

Figure 6.8: Calculated contribution to particle diffusivity from different instabilities for the ohmic discharge 98358 at TEXTOR. Fig. a) corresponds to the phase without DED and b) with DED for $\gamma_v = 3$.

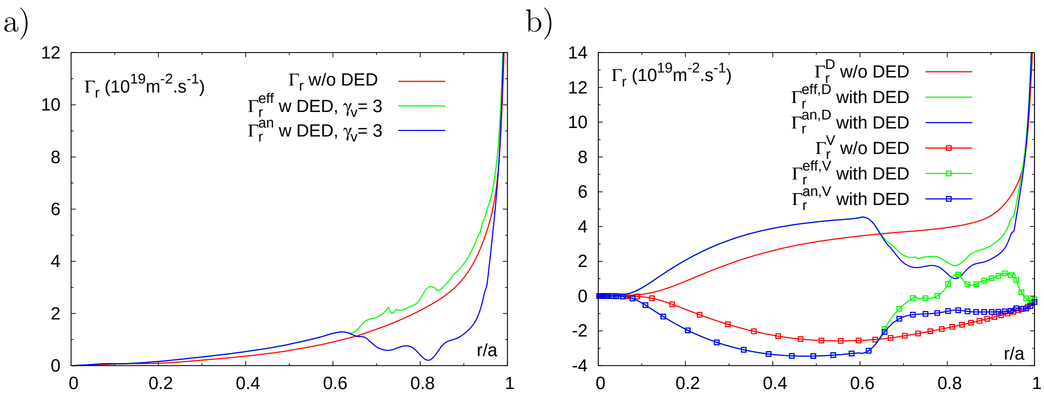

Figure 6.9: a) Simulated radial profiles of the radial anomalous and effective particle fluxes for TEXTOR discharge 98358, without and with DED. b) Repartition of these fluxes between diffusive ($\Gamma_\perp^D$) and convective ($\Gamma_\perp^V$) parts, with distinction between anomalous and effective fluxes.

is systematic and due to the cylindrical geometry assumption, and leads to an overestimation of the energy. There is thus a discrepancy between on one side diamagnetic energy measurements and on the other side electron temperature measurements form ECE and He-like spectra. In the following, it has been choosen to compare the results of calculations with the diamagnetic energy, measurements done by the author, and to use the ECE temperature measurements in order to validate the trends found in calculations.

6.3.2 Phase with DED

All the results of the simulations presented in figs. 6.7, 6.8 and 6.9 show that two regions can be distinguished in the plasma when stochastization is applied: the region with $r/a \gtrsim 0.6$, where density and temperature profiles are flatter than without stochastization, and the core region with $r/a \lesssim 0.6$, where gradients are larger or unchanged. Although the Chirikov parameter does not exceed 1 over its whole extend, the former region will henceforth be called the stochastic region because the direct effects of flows along the magnetic field are observed in this region. The flattening of the profiles in this region indicates an increase of heat and particle transport. This is in agreement with the generally accepted idea that stochastization of the magnetic field leads to an increase of radial transport. The further analysis of the transport modifications is performed separately for particles and heat.

Modification of particle transport

Simulations with adjusted gas puffing are considered first. One can see in fig. 6.7 that the modification of the density profile is smaller for $\gamma_v = 3$ than for $\gamma_v = 5$, i.e. the modification is stronger when kinetic effects tend to reduce the DED effects on the heat flow. This is very likely an indirect consequence of the temperature profile modifications, such that a further discussion of kinetic effects is postponed to the next section where heat transport modifications are discussed, and $\gamma_v = 3$ is assumed in the present section.

In the plasma core, the density gradient is approximately the same without and with stochastization, while it is reduced at the edge. This is partly due to the modification of the particle diffusion coefficients under stochastization, see fig. 6.8. This figure shows that anomalous diffusivity only slightly changes in the plasma core, while it is reduced in the stochastic region. Despite the small change in the total anomalous diffusivity, the nature of the latter is modified by the DED. Without stochastization, transport is dominated by TE and DA instabilities, except for the very center where the empirical diffusion coefficient D^c gives the main contribution. With the DED, TE and

DA contributions are drastically reduced, while ITG instabilities dominate diffusive transport on a broad region. These changes result from the modifications of the density and temperature profiles. The increase of L_n, which is relatively larger than the increase of L_{T_e} and L_{T_i}, leads to an increase of the ratio η_i (see section 3.2). As a consequence, ITG instabilities are triggered. The reduction of transport from TE modes is due to the decrease of the electron temperature, which yields an increase of the collisionality (term ν_{eff} in equation (3.14)). This modification from electron driven instabilities to ion driven instabilites is in agreement with observations performed by Reynolds stress probes [68], which show a change in the propagation of fluctuations from the electron diamagnetic drift direction without DED to the ion diamagnetic drift direction with DED. The diminution of the DA diffusivity cannot be straightforwardly seen from equation (3.16), but it is clear from this equation and from the considerations of section 6.1 that the electron pressure gradient plays a major role in this diminution. The increase of transport due to flows along field lines just brings the radial effective diffusivity at a level comparable or slightly higher than the radial diffusivity without stochastization.

It has just been seen that the diffusion coefficients is a bit larger with than without stochastization, but this alone does not mean that particle transport is higher. Particle fluxes without and with stochastization are compared in fig. 6.9. One can see that both the outward diffusive and inward convective parts of the anomalous flux are augmented in the core and reduced in the stochastic region. The result of this is a drastic reduction of the anomalous particle flux with DED in the stochastic region. This reduction of anomalous transport is compensated by flows along the magnetic field, such that the effective radial flux is a bit larger with stochastization than without. It is particularly interesting to note that flows along field lines mainly influence the convective part of the particle flux. From equation (2.31), one finds that the convective flux reads $(D^{eff} - D_\perp)/L_T$, i.e. temperature gradients play a major role in the increase of particle transport.

Some information on the modification of particle recycling can be gained from the simulation where the gas puffing and recycling coefficient were kept the same during the phases without and with DED (see fig. 6.7). In the experiment, the gas puffing was also identical during these two phases, but there is no information on the recycling coefficient. The comparison of the line averaged density variation in the simulation and in the experiment shows a larger drop of the former one with DED, i.e. an increase of the recycling coefficient is necessary in the simulation in order to recover the experimental line averaged density. This has been checked by increasing the recycling coefficient in simulations, and it was seen than an increase of 2 % was sufficient to match the experimental line averaged density. This simulation with the recycling coefficient increased by 2 % is actually equivalent to the one presented in fig. 6.7 where the gas puffing was adjusted. This comes from the fact that an adjustement of the gas puffing or of the recycling coefficient produces exactly the same result (the former one is generally adjusted for practical reasons).

Modification of heat transport

Figure 6.7 shows that both ion and electron temperature profiles are flatter in the stochastic region with DED than without, and steeper in the core. This means either that heat fluxes are reduced in the stochastic region, or that heat conductivities are increased, the opposite being true in the core region. From fig. 6.10, one can see that stochastization strongly modifies ion and electron heat conductivities, especially in the stochastic region. The modification of the ion heat conductivity is mainly due to a variation of the anomalous ion heat conductivity, while for electrons, the variation occurs predominantly through the parallel heat transport. Figure 6.10 also shows that the amplitude of kinetic effects has a large impact on the effective electron heat conductivity, and a marginal influence on the ion heat conductivity. This fact, together with the comparison of the different profiles in fig. 6.7, shows that the knowledge of the kinetic effect amplitude is important for the evaluation of stochastization effects on transport. However, kinetic simulations are beyond the scope of the present work, and the analysis is pursued with $\gamma_v = 3$.

Heat fluxes with and without stochastization are compared in fig. 6.11. This shows that the total ion heat flux is almost not modified by stochastization, while the electron flux is considerably increased. It also shows that for both ions and electrons, heat fluxes are mainly due to heat conduction, convective fluxes playing a secondary role. By combining the results shown in figs. 6.10 and 6.11, one can precise the causes of the temperature profile variations. In the case of ions, the variation results from the modification of the effective heat conductivity: it is decreased in the core and increased at the edge, leading to an increased temperature gradient in the core and a decreased gradient in the stochastic region. For electrons, effects of heat fluxes and conductivities are in competition: in the core, the increase of the heat flux dominates and leads to an increased temperature gradient, while at the edge, the increase of the heat conductivity prevails and has a reduction of the gradient as a consequence.

Finally, the diamagnetic energy is examined. In the experiment, it drops by 21 %, from 23.4 kJ to 18.5 kJ. In simulations with RITM, it drops by 27 %

in the case where $\gamma_v = 3$, from 27.4 kJ to 20 kJ. With $\gamma_v = 5$ the decrease is almost the same, namely 26 %. The decrease of the diamagnetic energy is thus reasonably reproduced. Note that since the electron temperature almost does not change (see fig. 6.7), the decrease of energy in the experiment is mainly due to the density drop.

Concluding remarks

The experimental density profile without DED has been reasonably reproduced by RITM simulations. The simulated electron temperature profile differs however much from the one measured by ECE, but it has been shown that a discrepancy actually exists between diamagnetic energy and electron temperature measurements. The energy content in simulations is larger than given by diamagnetic energy measurement, and lower than one can deduce from ECE temperature measurement. With DED, both measured and simulated density profiles are modified, the modification of the former being smaller than the one of the latter. One can also see that the profile modification occurs in a deeper region in the experiment: this is actually mainly due to the onset of a 2/1 tearing mode [16]. It is a general observation that almost no change is observed at TEXTOR with the DED before the onset of a tearing mode. However, since the effect of tearing modes cannot be described yet by the transport model in RITM, comparisons between experiment and simulations should be done with care. An attempt was done to perform a simulation at a lower DED current, before the onset of the tearing mode, but in this case the stochastization level is low and stochastization parameters obtained from field line mapping are not reliable.

The most interesting result of these simulations probably concerns heat transport. Heat conductivities from the present model and from the widely recognized model of reference [51] are compared in fig. 6.12. This shows that reference [51] predicts a heat conductivity larger than the present model by roughly one order of magnitude. RITM calculations with the heat conductivity proposed in this reference did not allow up to now to get converged solutions. Thus, although the simulations presented here show a modification of plasma profiles larger than what is observed in the experiment, the transport modification obtained with the present model is much closer to reality than that one would obtain from reference [51].

Finally, a remark concerning the results presented in reference [40] is made. At the time where they were published, the stochastization parameters used here, taken from field line mapping calculations, were not available. Therefore, the profiles of these parameters were estimated on the basis of discharges with similar experimental conditions, for which these parameters

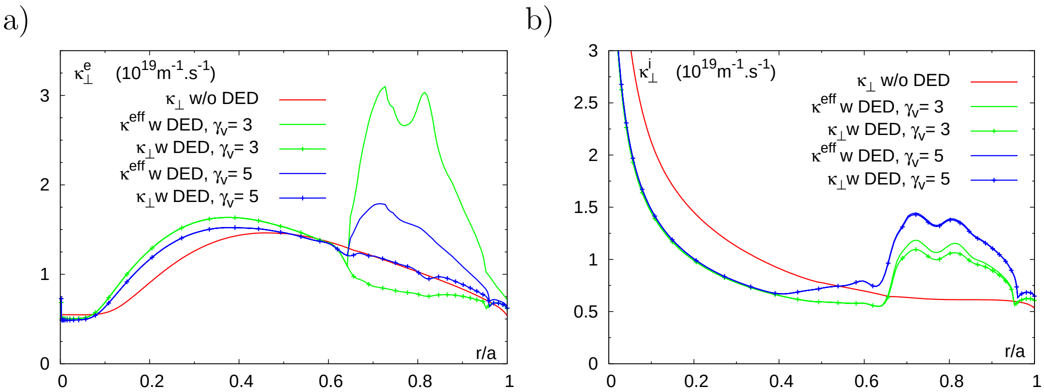

Figure 6.10: Radial profiles of effective and anomalous heat diffusivities from RITM simulations for TEXTOR discharge 98358 for a) electrons and b) ions, for different values of the parameter γ_v.

were available. A comparison of the results presented in this section and in reference [40] shows how important it is to know stochastization parameters with the best possible accuracy.

6.4 Auxiliary heated discharge in 3/1 DED configuration

TEXTOR discharge 97624 with strong auxiliary heating power from neutral beam injection has been also simulated with RITM [39]. The experimental parameters for this shot are the following: magnetic field of 2.25 T, plasma current of 300 kA, auxiliary heating power of 1.65 MW, and DC DED currents of 2.5 kA during the DED phase, with the DED operated in the 3/1 configuration. The stochastization parameters used for these simulations were taken from field line mapping and are shown in fig. 6.13. Measured and simulated density and temperature profiles are presented in fig. 6.14. As for discharge 98358, kinetic effects are investigated by varying the parameter γ_v.

6.4.1 Phase without DED

Transport model A has been used in the simulations like for ohmic discharge 98358, and a good reproduction of the experimental density profile has been achieved. However, despite numerous attempts, both discharges could not be simulated with identical values for the free parameters. In the present case, a scaling of the DA contribution by a factor $1/3(r/a)^2$ as for discharge 98358 leads to a too high ratio of heat transport to particle transport, leading to

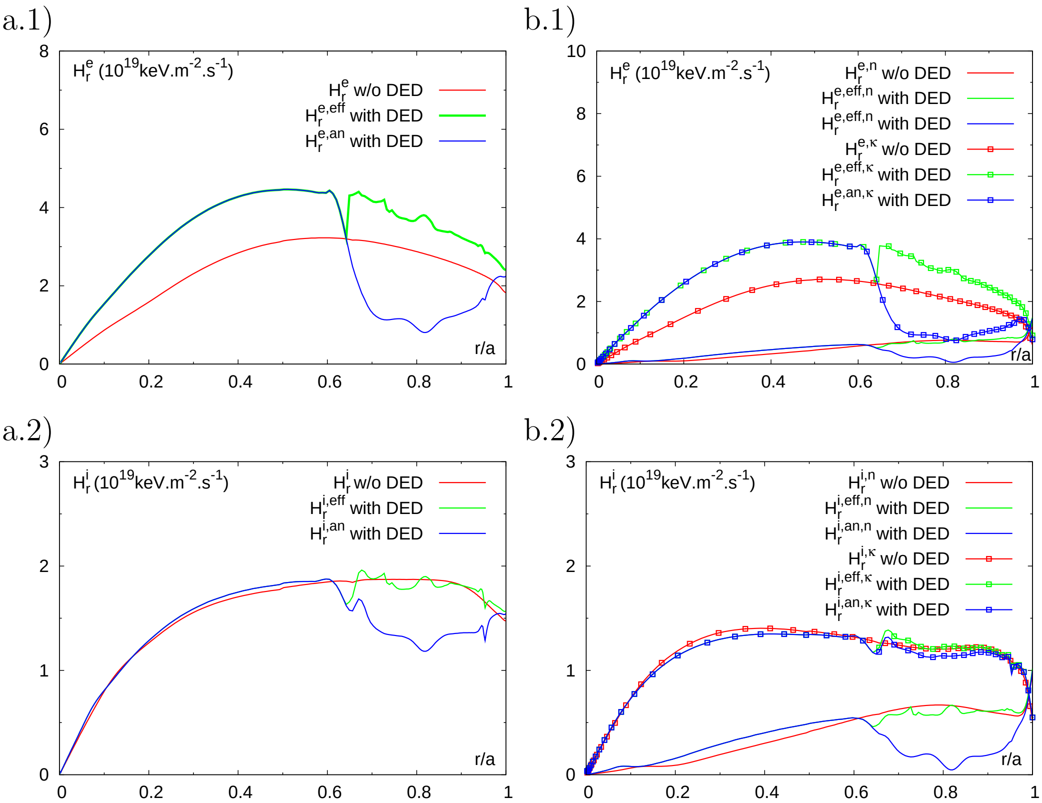

Figure 6.11: Radial profiles of the simulated a.1) electron and a.2) ion energy fluxes for discharge 98358 at TEXTOR, without and with DED, for $\gamma_v = 3$. In the case with stochastization, anomalous and effective contributions are shown separately. In figures b.1) and b.2), contributions from heat and convective fluxes to the energy flux are distinguished.

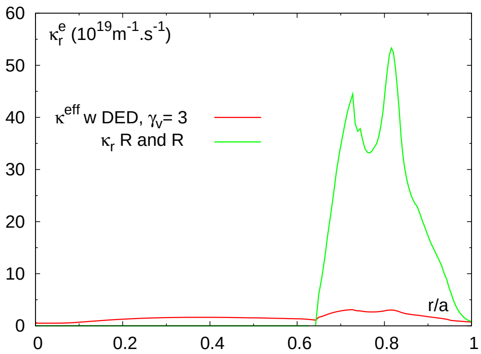

Figure 6.12: Radial profiles of the electron effective heat diffusivities calculated from RITM (κ^{eff}) and from reference [51] (κ_r R and R) for TEXTOR discharge 98358 during the DED phase. These profiles are computed on the base of profiles shown in fig. 6.7 for $\gamma_v = 3$.

much too flat temperature profile. Therefore, the parameter f_{DA} has been set to 1 for the simulation of discharge 97624, while ion and electron heat conductivities have been multiplied by 1/3. The same value as for discharge 98358 was taken for the parameter α_T, i.e. $\alpha_T = 0.1$.

Similarly to discharge 98358, a discrepancy between measurements of the electron temperature and of the diamagnetic energy is observed. The measured temperature is higher than calculated with RITM, but the diamagnetic energy is well reproduced, 40 kJ being obtained both in the experiment and in the calculation.

6.4.2 Phase with DED

During the DED phase, an increase of confinement is experimentally observed. The diamagnetic energy reaches 45 kJ, which represents an increase of 13 % with respect to the phase before DED. This modification is due to a rise of both the average density and electron temperature, as can be seen from fig. 6.14. Despite this increase, the shape of density and temperature profiles does not change.

The modification of the density profile is well reproduced in simulations, under both assumptions of moderate or strong kinetic effects. The increase of the temperature however has not been obtained, but, in agreement with the experiment, the shape of the temperature profiles is almost unaffected. It is interesting to see what happens when magnetic perturbations are increased. For this purpose, simulations have been performed with RITM for a DED current two times larger than in the experiment. The corresponding stochastization parameters are obtained by the quasi-linear scaling given in section 2.2.3 of the coefficients calculated by field mapping for the DED currents used in the experiment. These coefficients are shown in fig. 6.13. The simulated profiles for density and temperatures are compared in fig. 6.16. This shows significant decreases of both the ion and the electron temperatures, mainly in the core, while the density changes only at the edge. However, under such experiemental conditions, a 2/1 tearing mode is observed, which makes the comparison with simulations difficult.

Finally, fig. 6.15 shows the profiles of the effective heat conductivity computed for the DED phase with RITM and with the model of reference [51], both on the basis of the profiles with DED and for $\gamma_v = 3$, see fig. 6.14. Like for discharge 98358, a large difference is observed between these two profiles, the second one exceeding the first one by more than one order of magnitude. The same conclusion is thus valid for this discharge as for the ohmic discharge 98358, namely that the modification of heat transport unter stochastization calculated in the present work is much closer to the reality

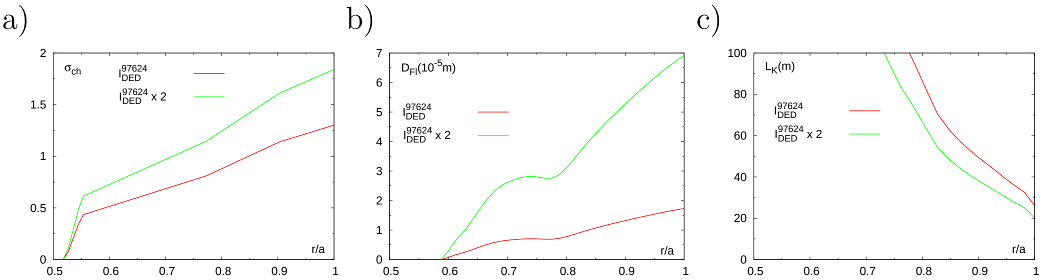

Figure 6.13: Stochastization parameters computed from field mapping for TEXTOR discharge 97624 versus the normalized radius r/a at time $t = 1.75\,\text{s}$. Stochastization parameters for a DED current twice as large as in this discharge are shown as well (green curve). They are obtained by a quasi-linear scaling of section 2.2.3 of the values obtained by field mapping. a) shows the Chirikov parameter, b) the field field line diffusivity and c) the Kolmogorov length.

than the modification that one gets with the model of reference [51].

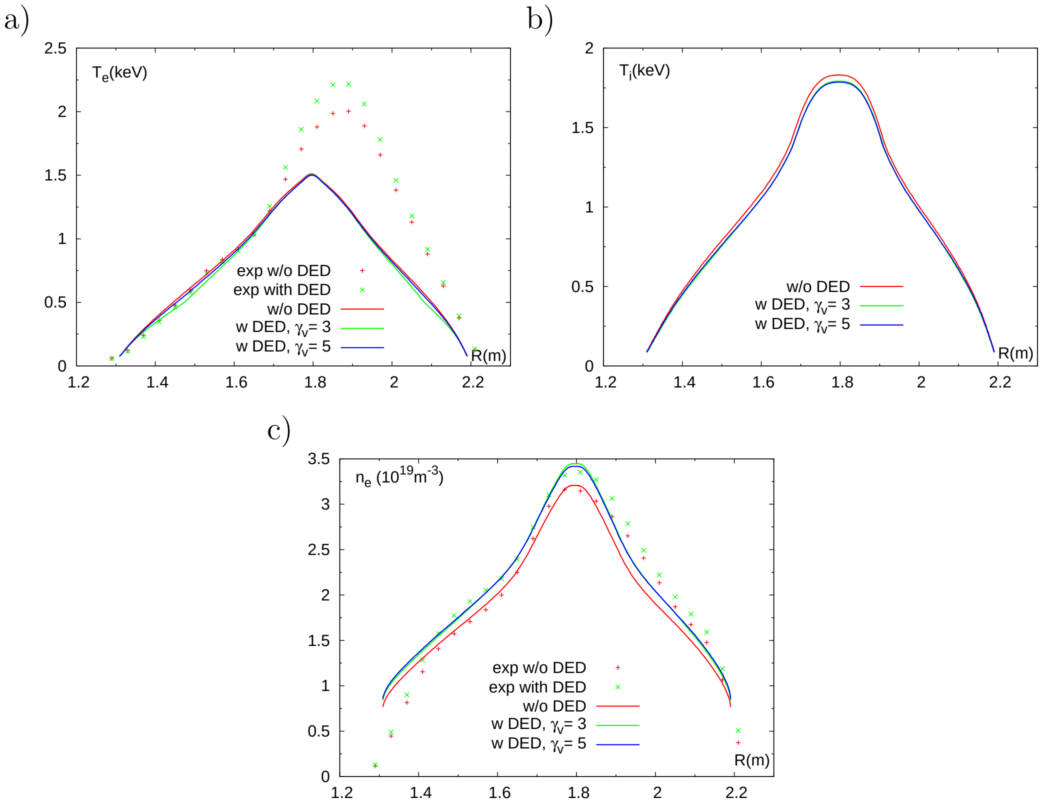

Figure 6.14: Radial profiles of density and temperatures from experiment (crosses) and from RITM simulations (solid curves) for TEXTOR discharge 97624 before and during the DED phase. For simulations with DED, profiles for two different values of the parameter γ_v are shown.

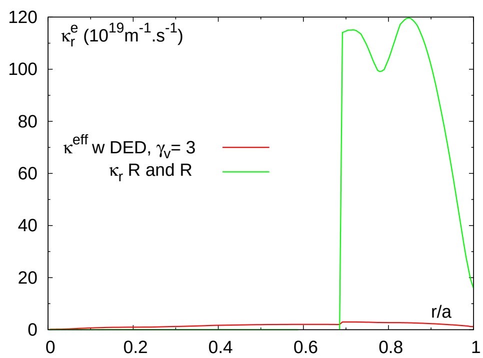

Figure 6.15: Radial profiles of the electron effective heat diffusivities calculated from RITM and from reference [51] for TEXTOR discharge 97624 during the DED phase. These profiles are computed on the base of profiles shown in fig. 6.14 for $\gamma_v = 3$.

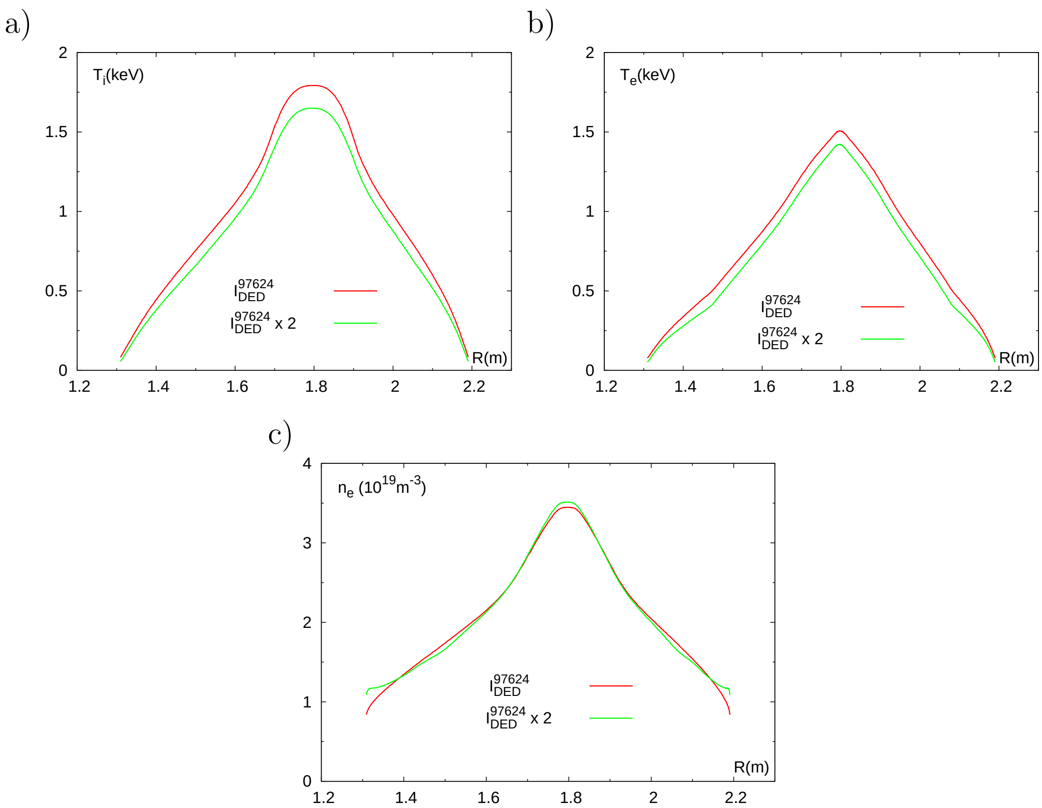

Figure 6.16: Comparison of the radial density and temperature profiles obtained from RITM simulations for TEXTOR discharge 97624 with $\gamma_v = 3$ for two different values of the DED current: in red, the value used in the experiment, and in green, a value twice as large as in the experiment.

Chapter 7

Summary and perspectives

In the present work, the influence of the DED on plasma transport properties in TEXTOR has been investigated, both theoretically and experimentally. For this purpose, different models for the modification of heat and particle transport have first been analyzed. The one from reference [61] has been chosen and further developed (see chapter 2). This approach provides effective coefficients for radial transport in the form of the product of perpendicular transport coefficients with a function accounting for transport along perturbed magnetic field lines. The perpendicular transport coefficients were determined by developing a model for anomalous perpendicular transport which takes into account the most important unstable drift modes under plasma edge conditions (see chapter 3). Then, with the purpose of performing self-consistent simulations of plasma parameter profiles in TEXTOR without and with DED, these models have been included in the 1.5D transport code RITM (see chapter 4). In addition to the anomalous transport model developed, a simpler one with characteristics taken from the literature has been included in RITM in order to get better converged solutions of transport equations. For the validation of the plasma profiles computed with RITM, measurements of the diamagnetic energy have been performed (see chapter 5).

The energy obtained with the diamagnetic loops is in agreement with multi-machine scalings, what gives confidence in this measurement. There is however a difference between the energy measured by this approach and the energy obtained by integration of density and temperature profiles over the tokamak volume, namely the latter one is always higher than the former one, sometimes by a factor as large as ≈ 1.5. The reason for this discrepancy has not been found yet and should be investigated in the future. Despite some uncertainties on the influence of the DED currents on the measurements, they confirm variations of profiles observed under DED operation, e.g. when a 2/1 tearing modes develops in the plasma [16].

The models for effective radial and anomalous perpendicular transport have been used for comparison with experimental profiles from the tokamak Tore Supra (Cadarache, France), operated with an ergodic divertor some years ago. In particular, electron temperature measurements give indications for a reduction of heat transport in the region with $r \approx 0.87a$, with a the plasma radius, when edge magnetic stochastization is produced by the ED. The calculations performed with the developed models showed a large reduction of radial transport coefficients in this region if temperature gradients are increased. This is in qualitative agreement with the steepening of the temperature profile indicated by measurements. It was also seen that the direct effects of the magnetic field stochastization included in the model for anomalous transport lead to marginal modifications of transport coefficients.

The transport model developed in chapter 3 has been used in order to determine under which conditions an H-mode could be achieved at TEXTOR and a power threshold for the L-H transition has been predicted [36]. Later, discharges with H-mode signatures were observed and the heating power necessary to achieve these is in agreement with the threshold calculated in advance. The experiment also showed that the DED could suppress these H-mode signatures, and simulation of such a discharge is in progress.

The main modification of the plasma confinement observed at TEXTOR with the DED is a decrease of the energy confinement by $10-20\,\%$ observed at the onset of a 2/1 tearing mode, the latter being triggered by the magnetic perturbations when the DED currents exceed a critical value. This critical value depends on the experimental conditions and on the DED configuration, and has not been observed in a 12/4 configuration. When no tearing mode is triggered, only moderate modifications of the energy content are seen. Note also that discharges with a significant increase of the particle confinement have been achieved recently with the DED, but these results have not been analyzed yet.

Simulations have been performed with RITM for an ohmic discharge where a drop of $20\,\%$ of the diamagnetic energy is observed with the DED, and for an auxiliary heated discharge where the DED leads to an increase of about $13\,\%$ of the energy. For phases without DED, a good agreement with the experimental density profiles has been obtained in both cases and the calculated diamagnetic energies are close to the measured ones. The calculated electron temperature profiles provide a temperature lower than the ones measured by ECE, and it has been seen that it is not possible to match the measured diamagnetic energy and temperature profile at the same time. Since the measured diamagnetic energy is reproduced, it has not been tried to match the measured electron temperature profile by artificially modifying heat transport coefficients, but this could be an interesting development of the present investigations. During the DED phase, small modifications of the density and temperature profiles and of the diamagnetic energy are observed in the experiment. For the ohmic discharge, both the modifications of the density and of the energy have been reasonably reproduced, although a 2/1 tearing mode develops in the plasma, for which no model is presently included in RITM. The small increase of the electron temperature obtained in the simulation is however not observed experimentally. For the discharge with auxiliary heating, the small modification of the density profile could be well reproduced, but not the increase of the diamagnetic energy and of the temperature. A possible explanation for this is that the assumption of a heat conductivity proportional to the diffusion coefficient, $\kappa_\perp = 3/2\, nD_\perp$, might not be valid. This should be investigated in a future development of this work.

The influence of kinetic effects on the parallel heat conductivity has been investigated for the above mentioned discharges by performing simulations with two extreme assumptions for the amplitude of kinetic effects. This showed a moderate difference between the profiles obtained with these two extreme values. A comparison with experimental profiles, however, does not allow to get precisions on the real amplitude of these effects.

The most useful conclusion of the present work probably concerns the amplitude of the heat transport increase one can expect in a tokamak as a consequence of a stochastization of the magnetic field. It was shown in chapter 6 that, although modifications of the diamagnetic energy obtained with the model of chapter 2 are not always perfectly reproduced, the smallness of these energy variations is in agreement with the experimental observations. The widely referenced model of reference [51], however, predicts a heat transport in a stochastic magnetic field at least one order of magnitude larger than the present model. This would result in a large loss of confinement, much larger than what is observed with the DED at TEXTOR. The amplitude of the heat transport increase given in chapter 2 is thus much closer to the reality than the one given in reference [51].

Finally, perspectives of development for the present work are discussed:

- In order to achieve a better reproduction in calculations of plasma parameters both in ohmic and auxiliary heated discharges, the introduction of a pinch velocity for transport from edge instabilities can be an important improvement of the model.

- An improvement of the model for anomalous prependicular heat conductivity instead of the simple proportionality relation with the particle diffusivity can lead to a better agreement between calculated and measured diamagnetic energy in discharges where a significant increase of the energy has been observed experimentally. This point could be investigated by further developing the anomalous transport model of chapter 3 by inclusion of the heat balance equations to calculate the perturbations of ion and electron temperatures, and calculation of the heat flux due to fluctuations on a similar way as it was done for particle transport.

- In order to simulate with a better accuracy discharges where a tearing mode develops, a model for these modes should be developed and included into RITM.

- A self-consistent modelling of plasma rotation, which exhibits strong modifications with TEXTOR DED, should also be included into RITM.

- The perturbations produced by the DED currents on diamagnetic measurements should be better characterized. Since two independent systems for the measurement of the diamagnetic energy are now operational, this point could be achieved by comparing the perturbations induced by the DED in the two systems of diamagnetic loops. The discrepancy between diamagnetic energy and electron temperature measurements should be investigated as well.

- Finally, in the model of chapter 2, ambipolarity is prescribed by imposing identical fluxes for electrons and ions, both along and across the magnetic field. The approach of reference [33] is different in the sense that it assumes a negligible ion parallel flux, the ambipolarity condition being satisfied by a larger perpendicular flux for ions than for electrons. A further development of these two models would be achieved by allowing the ion and electron parallel fluxes to be finite, and different from each other.

Appendix A

Temperature variation along a parallel segment of path

The temperature change along a parallel section can be obtained by integration of equation (2.13):

$$\Delta_{\parallel} T_e = \int_0^L \frac{\partial T_e}{\partial l} dl = \int_0^L \frac{-q_r - 2\kappa_{\perp} \Delta_{\parallel} T_e / (\delta_L - \delta_0)}{\kappa_{\parallel} \sin \alpha (l)} dl. \tag{A.1}$$

Since small pitch angles for the field lines are considered, such that $\sin \alpha (l)$ is approximated by $\tan \alpha (l)$, with $\tan \alpha(l) = \frac{1}{2} \frac{d\delta(l)}{dl}$.

A.1 Case $L \lesssim L_K$

For short parallel scales, thus with δ given by equation (2.9), equation (A.1) reads

$$\begin{aligned} \Delta_{\parallel} T_e &= -2 \int_0^L \frac{q_r + 2\kappa_{\perp} \Delta_{\parallel} T_e / (\delta_L - \delta_0)}{\kappa_{\parallel} \delta_0} L_K e^{-l/L_K} dl \\ &= -2 \left(-\kappa_{\perp} \frac{\Delta_{\perp} T_e}{\delta_0} + \frac{2\kappa_{\perp} \Delta_{\parallel} T_e}{\delta_0 (e^X - 1)} \right) \frac{L_K}{\kappa_{\parallel} \delta_0} \int_0^L e^{-l/L_K} dl \\ &= \frac{\Delta_{\perp} T_e \left(1 - e^{-X}\right) - 2 \Delta_{\parallel} T_e e^{-X}}{\zeta_K} \end{aligned} \tag{A.2}$$

with $X = L/L_K$, $\zeta_K = \kappa_{\parallel} \delta_0^2 / (2\kappa_{\perp} L_K^2)$ and where equation (2.12) has been used. By isolating $\Delta_{\parallel} T_e$, one obtains

$$\Delta_{\parallel} T_e = \Delta_{\perp} T_e \frac{1 - e^{-X}}{\zeta_K + 2e^{-X}}. \tag{A.3}$$

Introduction of this result into equation (2.10) gives

$$\begin{aligned}\kappa^{path} &= -\frac{q_r}{2}\frac{\delta_0\left(e^X+1\right)}{\Delta_\perp T_e + \Delta_\| T_e} \\ &= \frac{\kappa_\perp}{2}\frac{e^X+1}{1+(1-e^{-X})/(\zeta_K+2e^{-X})} \\ &= \kappa_\perp\left(1+\frac{1}{2}\frac{\zeta_K\left(e^X-1\right)}{\zeta_K+1+e^{-X}}\right). \end{aligned} \tag{A.4}$$

The mean value $\overline{|\partial \ln T_e/\partial l|}$ of $|\partial \ln T_e/\partial l|$, used in section 2.3.1, can now be computed:

$$\begin{aligned}\overline{|\partial \ln T_e/\partial l|} \approx &\frac{1}{L}\int_0^L |\partial \ln T_e/\partial l|\, dl &&= \frac{1}{L}\int_0^L \left|\frac{\nabla_r T_e}{T_e}\right| \sin\alpha(l) dl \\ =&\frac{1}{L}\frac{1}{L_{T_e}}\int_0^L \frac{1}{2}\frac{\partial \delta}{\partial l} e^{l/L_K} dl &&= \frac{1}{L}\frac{1}{L_{T_e}}\frac{\delta_0}{2}\left(e^X-1\right) \\ =&\frac{1}{L_{T_e}}\sqrt{\frac{D_{Fl}}{2L_K X}}\left(1-e^{-X}\right). \end{aligned} \tag{A.5}$$

Note that condition (2.16) was used in the last step.

A.2 Case $L \gg L_K$

For the case $L \gg L_K$, it is assumed that $\delta_0 \ll \delta_L$. With δ given by equation (2.7), equation (A.1) reads

$$\begin{aligned}\Delta_\| T_e &\approx \int_0^L \frac{-q_r - 2\kappa_\perp \Delta_\| T_e/\sqrt{2D_{Fl}L}}{\kappa_\| \sqrt{D_{Fl}}/2}\sqrt{2l} dl \\ &= 2\frac{1}{\kappa_\|}\sqrt{\frac{2}{D_{Fl}}}\left(-q_r - \frac{2\kappa_\perp \Delta_\| T_e}{\sqrt{2D_{Fl}L}}\right)\int_0^L \sqrt{l} dl \\ &= \frac{4}{3}\frac{1}{\kappa_\|}\sqrt{\frac{2}{D_{Fl}}}\left(-q_r - \frac{2\kappa_\perp \Delta_\| T_e}{\sqrt{2D_{Fl}L}}\right) L^{3/2}. \end{aligned} \tag{A.6}$$

Thus

$$\Delta_\| T_e = -\frac{q_r}{\kappa_\perp}\frac{\sqrt{2D_{Fl}L}}{2+3\kappa_\| D_{Fl}/\left(4\kappa_\perp L\right)}. \tag{A.7}$$

It is now assumed that $\Delta_\perp T_e \ll \Delta_\| T_e$, as a consequence of the assumption $\delta_0 \ll \delta_L$. Insertion of equation (A.7) into equation (2.10) yields then

$$\begin{aligned} \kappa^{path} &\approx -\frac{q_r}{2} \frac{\sqrt{2 D_{Fl} L}}{\Delta_\| T_e} \\ &= \kappa_\perp + \frac{3}{8} \kappa_\| \frac{D_{Fl}}{L}. \end{aligned} \tag{A.8}$$

Appendix B

Density variation along a parallel segment of path

Combination of equations (2.25) and (2.28) gives

$$\begin{aligned}
\frac{\partial n}{\partial l} =& -\frac{m_i n V_\parallel}{T_e + T_i}\left[\mu_\perp\left(\frac{1}{\delta^2(l)} + \frac{1}{\delta^2(L-l)}\right) + \left(\frac{D_\perp + \mu_\perp}{L_n} + V_\perp\right)\frac{1}{\delta(l)}\right] \\
& - n\frac{\partial\left(T_e + T_i\right)/\partial l}{T_e + T_i} \\
=& -\frac{1}{c_s^2 \sin\alpha}\left(\Gamma_r - nV_\perp + D_\perp \frac{2\Delta_\parallel n}{\delta_L - \delta_0}\right) \times \\
& \times \left[\mu_\perp\left(\frac{1}{\delta^2(l)} + \frac{1}{\delta^2(L-l)}\right) + \left(\frac{D_\perp + \mu_\perp}{L_n} + V_\perp\right)\frac{1}{\delta(l)}\right] \\
& - n\frac{\partial \ln\left(T_e + T_i\right)}{\partial l}
\end{aligned} \tag{B.1}$$

where $c_s = \sqrt{(T_e + T_i)/m_i}$ is the sound speed. The second term on the right-hand side can be rewritten

$$\begin{aligned}
-n\frac{\partial \ln\left(T_e + T_i\right)}{\partial l} &= -n\frac{\nabla_r\left(T_e + T_i\right)}{T_e + T_i}\sin\alpha \\
&= \frac{n}{L_T}\sin\alpha
\end{aligned} \tag{B.2}$$

with $L_T = -\nabla_r \ln\left(T_e + T_i\right)$. With the purpose of introducing it into equation (2.23), $\Delta_\parallel n = \int_0^L \frac{\partial n}{\partial l} dl$ is now computed.

B.1 Case $L \lesssim L_K$

With equation (2.9) for the expression of $\delta(l)$, and with the same assumption for $\sin\alpha$ as in appendix A, integration of equation (B.2) gives

$$\begin{aligned}\int_0^L \frac{n}{L_T} \sin\alpha\,(l)\, dl &= \frac{n}{L_T} \int_0^L \frac{1}{2}\frac{\delta_0}{L_K} e^{l/L_K} dl \\ &= \frac{n}{L_T}\frac{\delta_0}{2}\left(e^X - 1\right) \end{aligned} \tag{B.3}$$

Integration of the first term on the right-hand side of equation (B.1) leads to

$$\begin{aligned} &-\frac{2L_K}{c_s^2\delta_0}\left(\Gamma_r - nV_\perp + \frac{D_\perp}{\delta_0}\frac{2\Delta_\parallel n}{e^X - 1}\right) \times \\ &\quad \times \int_0^L e^{-l/L_K}\left[\frac{\mu_\perp}{\delta_0^2}\left(e^{-2l/L_K} + e^{2(l-L)/L_K}\right) + \left(\frac{D_\perp + \mu_\perp}{L_n} + V_\perp\right)\frac{e^{-l/L_K}}{\delta_0}\right] dl \\ &= -\frac{2\mu_\perp L_K^2}{c_s^2\delta_0^3}\left(\Gamma_r - nV_\perp + \frac{D_\perp}{\delta_0}\frac{2\Delta_\parallel n}{e^X - 1}\right) \times \\ &\quad \times \left[\frac{1 - e^{-3X}}{3} + e^{-2X}\left(e^X - 1\right) + \left(\frac{D_\perp + \mu_\perp}{L_n} + V_\perp\right)\frac{\delta_0}{\mu_\perp}\frac{1 - e^{-2X}}{2}\right] \end{aligned} \tag{B.4}$$

which yields, together with (B.3)

$$\Delta_\parallel n = -\left(\frac{\Gamma_r - nV_\perp}{D_\perp}\delta_0 + \frac{2\Delta_\parallel n}{e^X - 1}\right) j(X) + \frac{n}{L_T}\frac{\delta_0}{2}\left(e^X - 1\right) \tag{B.5}$$

or, after isolation of $\Delta_\parallel n$,

$$\Delta_\parallel n = -\frac{\left(e^X - 1\right) j(X)}{\left(e^X - 1\right) + 2j(X)}\frac{\Gamma_r - nV_\perp}{D_\perp}\delta_0 + \frac{n}{L_T}\frac{\delta_0}{2}\frac{\left(e^X - 1\right)^2}{\left(e^X - 1\right) + 2j(X)}, \tag{B.6}$$

with

$$j(X) = \frac{1}{\zeta_D}\left[\frac{1 - e^{-3X}}{3} + e^{-2X}\left(e^X - 1\right) + \frac{D_\perp + \mu_\perp}{\mu_\perp}\frac{\delta_0}{L_n}\frac{1 - e^{-2X}}{2}\right] \tag{B.7}$$

and $\zeta_D = c_s^2\delta_0^4/\left(2\mu_\perp D_\perp L_K^2\right)$. The radial density gradient is given by

$$\nabla_r n \equiv \frac{\Delta_\perp n + \Delta_\parallel n}{(\delta_L + \delta_0)/2}. \tag{B.8}$$

Combining (B.6) and (B.8) and isolating Γ_r, one gets

$$\begin{aligned}\Gamma_r = &-\frac{e^X+1}{2}\frac{(e^X-1)+2j(X)}{(e^X-1)+(e^X+1)j(X)}D_\perp \nabla_r n \\ &+\frac{(e^X-1)^2}{(e^X-1)+(e^X+1)j(X)}\frac{D_\perp}{2L_T}n + nV_\perp \end{aligned}\tag{B.9}$$

According to equation (2.23), the transport coefficients along the path are found to be

$$\begin{aligned}D^{path} &= D_\perp\left[1+\frac{1}{2}\frac{\left(e^X-1\right)^2}{(e^X-1)+(e^X+1)\,j\,(X)}\right] \\ V^{path} &= V_\perp + \frac{D^{path}-D_\perp}{L_T}.\end{aligned}\tag{B.10}$$

B.2 Case $L \gg L_K$

Integration of the second term on the right-hand side of equation (B.1) gives

$$\begin{aligned}\int_0^L \frac{n}{L_T}\sin\alpha\,(l)\,dl &= \frac{n}{L_T}\int_0^L \frac{1}{2}\frac{d\delta}{dl}dl \\ &= \frac{n}{2L_T}\sqrt{2D_{Fl}L}\end{aligned}\tag{B.11}$$

and integration of the first term yields

$$\begin{aligned}&-\int_0^L \frac{1}{c_s^2\sin\alpha}\left(\Gamma_r - nV_\perp + D_\perp\frac{2\Delta_\parallel n}{\delta_L-\delta_0}\right)\times \\ &\quad\times\left[\mu_\perp\left(\frac{1}{\delta^2(l)}+\frac{1}{\delta^2(L-l)}\right)+\left(\frac{D_\perp+\mu_\perp}{L_n}+nV_\perp\right)\frac{1}{\delta(l)}\right]dl \\ &= -\frac{2\mu_\perp}{c_s^2}\left(\Gamma_r - nV_\perp + D_\perp\frac{2\Delta_\parallel n}{\sqrt{2D_{Fl}L}}\right)\times \\ &\quad\times\int_0^L\sqrt{\frac{2l}{D_{Fl}}}\left[\left(\frac{1}{2D_{Fl}l}+\frac{1}{2D_{Fl}(L-l)}\right)+\left(\frac{D_\perp+\mu_\perp}{\mu_\perp L_n}+\frac{V_\perp}{\mu_\perp}\right)\frac{1}{\sqrt{2D_{Fl}l}}\right]dl \\ &= -\frac{2\mu_\perp}{c_s^2}\left(\Gamma_r - nV_\perp + D_\perp\frac{2\Delta_\parallel n}{\sqrt{2D_{Fl}L}}\right)\times \\ &\quad\times\int_0^L\left[\frac{1}{2D_{Fl}\sqrt{D_{Fl}}}\left(\sqrt{\frac{2}{l}}+\frac{\sqrt{2l}}{L-l}\right)+\left(\frac{D_\perp+\mu_\perp}{\mu_\perp L_n}+\frac{V_\perp}{\mu_\perp}\right)\frac{1}{D_{Fl}}\right]dl\end{aligned}$$

$$\approx -\frac{2}{c_s^2 D_{Fl}}\left(\Gamma_r - nV_\perp + D_\perp \frac{2\Delta_\parallel n}{\sqrt{2D_{Fl}L}}\right)\times$$
$$\times\left[\frac{\mu_\perp}{2\sqrt{D_{Fl}}}\left(2\sqrt{2L}+\sqrt{2L}\left(\ln\frac{2L}{\delta_0}-2\right)\right)+\left(\frac{D_\perp+\mu_\perp}{\mu_\perp L_n}+\frac{V_\perp}{\mu_\perp}\right)L\right]$$
$$= -\left(\frac{\Gamma_r - nV_\perp}{D_\perp}\sqrt{2D_{Fl}L}+2\Delta_\parallel n\right)k(L), \tag{B.12}$$

with

$$k(L) = \frac{2}{\zeta_n}\left[\ln\frac{2L}{\delta_0}+\left(\frac{D_\perp+\mu_\perp}{\mu_\perp L_n}+\frac{V_\perp}{\mu_\perp}\right)\sqrt{2D_{Fl}L}\right]$$

and $\zeta_n = 2c_s^2 D_{Fl}^2/(D_\perp \mu_\perp)$, and where $\delta_0 \ll \sqrt{2D_{Fl}L}$ was assumed. The integration of $\sqrt{2l}/(L-l)$ cannot be performed on the interval $[0, L]$, reflecting the fact that the distance between distinct field lines cannot vanish. The integral should thus be evaluated on an interval $[0, l]$, with $l \to L$. The interval $[0, L-\delta_0]$ is chosen here, but this choice is not crucial since only the qualitative behavior of $k(L)$ is of interest here. Thus

$$\begin{aligned}\int_0^{L-\delta_0}\frac{\sqrt{2l}}{L-l}dl =& 2\sqrt{2L}\int_0^{1-\delta_0/L}\frac{z^2}{1-z^2}dz\\ =&\sqrt{2L}\int_0^{1-\delta_0/L}\left(\frac{1}{1-z}+\frac{1}{1+z}-2\right)dz\\ \approx&\sqrt{2L}\left(\ln\frac{2L}{\delta_0}-2\right).\end{aligned} \tag{B.13}$$

with $z^2 = l/L$. From equations (B.11) and (B.12), the total density change along a parallel part of the path can be evaluated:

$$\Delta_\parallel n = \frac{1}{1+2k(L)}\left[-k(L)\frac{\Gamma_r - nV_\perp}{D_\perp}\sqrt{2D_{Fl}L}+\frac{n}{2L_T}\sqrt{2D_{Fl}L}\right]. \tag{B.14}$$

Insertion of this result into equation (B.8), and isolation of Γ_r leads to

$$\Gamma_r = -\frac{1+2k(L)}{2k(L)}D_\perp \nabla_r n + \frac{D_\perp}{2k(L)}\frac{n}{L_T}+nV_\perp, \tag{B.15}$$

yielding in turn, according to the definition (2.23), the following transport coefficients:

$$\begin{aligned}D^{path} &= D_\perp\left[1+\frac{\zeta_n}{4}\left[\ln\frac{2L}{\delta_0}+\left(\frac{D_\perp+\mu_\perp}{\mu_\perp L_n}+\frac{V_\perp}{\mu_\perp}\right)\sqrt{2D_{Fl}L}\right]^{-1}\right]\\ V^{path} &= V_\perp + \frac{D^{path}-D_\perp}{L_T}.\end{aligned} \tag{B.16}$$

Appendix C

Average value of $V_{\parallel}$ and $\nabla_{\parallel} V_{\parallel}$

In this appendix, $\overline{V}_{\parallel}$, the average parallel velocity along a parallel segment of path, and $\nu_{\parallel}$, the average of $\partial V_{\parallel}/\partial l$ along the same segment, are estimated. $V_{\parallel}$ is first isolated from the particle balance along the field lines, equation (2.25):

$$V_{\parallel} = \frac{\Gamma_r - V_{\perp} n + D_{\perp} \nabla_{\perp} n}{n \sin \alpha}. \tag{C.1}$$

$\overline{V}_{\parallel}$ is then evaluated by division of the integral of (C.1) along a parallel section of path, by the length of this section of path:

$$\begin{aligned}
\overline{V}_{\parallel} =& \frac{1}{L} \int_0^L \frac{\Gamma_r - V_{\perp} n + D_{\perp} \nabla_{\perp} n}{n \sin \alpha} dl \\
=& \frac{1}{nL} \left[\Gamma_r - V_{\perp} n + D_{\perp} \frac{2\Delta_{\parallel} n}{\delta_0 \left(e^X - 1\right)} \right] \int_0^L \frac{2L_K}{\delta_0} e^{-l/L_K} dl \\
=& \frac{2L_K^2}{n \delta_0 L} \left(1 - e^{-X}\right) \Bigg[\left(\Gamma_r - V_{\perp} n\right) \\
& \qquad + \frac{1}{\left(e^X - 1\right) + 2j(X)} \left(-2j(X) \left(\Gamma_r - V_{\perp} n\right) + \frac{n}{L_T} D_{\perp} \left(e^X - 1\right) \right) \Bigg] \\
=& \frac{2L_K}{n \delta_0 X} \frac{\left(1 - e^{-X}\right)\left(e^X - 1\right)}{\left(e^X - 1\right) + 2j(X)} \left[\Gamma_r - V_{\perp} n + \frac{n}{L_T} D_{\perp} \right] \\
=& X^{-3/2} \sqrt{\frac{2L_K}{D_{Fl}}} \frac{\left(e^X - 1\right)^2}{\left(e^X - 1\right) + 2j(X)} D_{\perp}^{eff} \left[\frac{1}{L_n} + \frac{1}{L_T} \right]
\end{aligned} \tag{C.2}$$

The average of the parallel derivative is then approximated by division of the average velocity by the length of the parallel section of the path: $\nu_{\parallel} \approx \overline{V}_{\parallel}/L$.

Appendix D

Divergence of the ion perturbation flux

The divergence of the ion perturbation flux is calculated here. It consists of different parts of the form

$$\boldsymbol{\nabla} \cdot \left(\widetilde{\frac{\boldsymbol{B} \times \boldsymbol{C}}{B^2}} \right) = \boldsymbol{\nabla} \cdot \left(\frac{\boldsymbol{B} \times \widetilde{\boldsymbol{C}}}{B^2} \right) + \boldsymbol{\nabla} \cdot \left(\widetilde{\left(\frac{\boldsymbol{B}}{B^2} \right)} \times \boldsymbol{C}_0 \right) \tag{D.1}$$

where $\boldsymbol{C}$ represents the gradient of different quantities. Some derivatives used later are first calculated. The first part concerns the unperturbed magnetic field:

$$\begin{aligned} \boldsymbol{\nabla} \times \boldsymbol{B} = \begin{vmatrix} \boldsymbol{e}_r & \boldsymbol{e}_\theta & \boldsymbol{e}_\varphi \\ \nabla_r & \nabla_\theta & 0 \\ 0 & B_\theta & B_\varphi \end{vmatrix} &= \frac{1}{r}\frac{\partial B_\varphi}{\partial \theta}\boldsymbol{e}_r - \frac{\partial B_\varphi}{\partial r}\boldsymbol{e}_\theta + \frac{1}{r}\frac{\partial (rB_\theta)}{\partial r}\boldsymbol{e}_\varphi \\ &\approx \frac{1}{r}\frac{\partial B_\varphi}{\partial \theta}\boldsymbol{e}_r - \frac{\partial B_\varphi}{\partial r}\boldsymbol{e}_y + \frac{1}{r}\frac{\partial (rB_\theta)}{\partial r}\boldsymbol{e}_\parallel \end{aligned} \tag{D.2}$$

where relations (3.18) have been used. Note that expression (D.2) is used for $\boldsymbol{\nabla} \times \boldsymbol{B}$ instead of Maxwell's equation as the precise repartition of the equilibrium current is not known. With the help of equation (3.19), one gets

$$\begin{aligned} \frac{\partial B_\varphi}{\partial r} &= -\frac{B_*}{R_*}\cos\theta \\ \frac{1}{r}\frac{\partial B_\varphi}{\partial \theta} &= \frac{B_*}{R_*}\sin\theta \\ \frac{1}{r}\frac{\partial (rB_\theta)}{\partial r} &= \frac{1}{r}\frac{\partial}{\partial r}\left(\frac{r^2 B_\varphi}{qR}\right) = \frac{1}{r}\frac{\partial}{\partial r}\left(\frac{r^2 B_*}{qR_*}\right) = \frac{1}{r}\frac{B_*}{R_*}\frac{\partial}{\partial r}\left(\frac{r^2}{q}\right) = \frac{B_*}{R_*}\frac{2-\hat{s}}{q} \end{aligned} \tag{D.3}$$

where $\hat{s}$ is introduced according to equation (2.3). Other quantities of interest are:

$$\begin{aligned}
\nabla_r \frac{1}{B} &= \frac{\partial}{\partial r} \frac{1 + \frac{r}{R_*}\cos\theta}{B_*} = \frac{\cos\theta}{R_* B_*} \\
\nabla_y \frac{1}{B} &= \boldsymbol{e}_y \cdot \boldsymbol{\nabla} \frac{1}{B} \approx \frac{1}{r}\frac{\partial}{\partial \theta} \frac{1 + \frac{r}{R_*}\cos\theta}{B_*} = \frac{-\sin\theta}{R_* B_*}
\end{aligned} \tag{D.4}$$

$$\begin{aligned}
\nabla_r \frac{1}{B^2} &= \frac{\partial}{\partial r} \frac{\left(1 + \frac{r}{R_*}\cos\theta\right)^2}{B_*^2} = \frac{\partial}{\partial r} \frac{1 + 2\frac{r}{R_*}\cos\theta}{B_*^2} = \frac{2\cos\theta}{R_* B_*^2} \\
\nabla_y \frac{1}{B^2} &\approx \nabla_\theta \frac{1}{B^2} = \frac{1}{r}\frac{\partial}{\partial \theta} \frac{\left(1 + \frac{r}{R_*}\cos\theta\right)^2}{B_*^2} \approx \frac{1}{r}\frac{\partial}{\partial \theta} \frac{1 + 2\frac{r}{R_*}\cos\theta}{B_*^2} = \frac{-2\sin\theta}{R_* B_*^2}
\end{aligned} \tag{D.5}$$

and

$$\begin{aligned}
\boldsymbol{B} \times \boldsymbol{\nabla} \frac{1}{B^2} &= \begin{vmatrix} \boldsymbol{e}_r & \boldsymbol{e}_\theta & \boldsymbol{e}_\varphi \\ 0 & B_\theta & B_\varphi \\ \frac{2\cos\theta}{R_* B_*^2} & -\frac{2\sin\theta}{R_* B_*^2} & 0 \end{vmatrix} \\
&= \frac{2\sin\theta}{R_* B_*^2} B_\varphi \boldsymbol{e}_r + \frac{2\cos\theta}{R_* B_*^2} B_\varphi \boldsymbol{e}_\theta - \frac{2\cos\theta}{R_* B_*^2} \frac{r B_\varphi}{q R_*} \boldsymbol{e}_\varphi \\
&\approx \frac{2\sin\theta}{R_* B_*} \boldsymbol{e}_r + \frac{2\cos\theta}{R_* B_*} \boldsymbol{e}_y
\end{aligned} \tag{D.6}$$

where the last term on the left-hand side was dropped due to the ordering. In order to estimate the second term of equation (D.1), the following quantities are calculated, where the derivatives concern $\widetilde{\boldsymbol{B}}$ only, not $\boldsymbol{B}$:

$$\boldsymbol{\nabla} \times \widetilde{\boldsymbol{B}} = \begin{vmatrix} \boldsymbol{e}_r & \boldsymbol{e}_y & \boldsymbol{e}_\parallel \\ \nabla_r & \nabla_y & \nabla_\parallel \\ \widetilde{B}_r & \widetilde{B}_y & 0 \end{vmatrix} = -\nabla_\parallel \widetilde{B}_y \boldsymbol{e}_r + \nabla_\parallel \widetilde{B}_r \boldsymbol{e}_y + \left(ik_r \widetilde{B}_y - ik_y \widetilde{B}_r\right) \boldsymbol{e}_\parallel, \tag{D.7}$$

and

$$\begin{aligned}
\nabla_r \widetilde{\left(\frac{1}{B^2}\right)} &= \nabla_r \frac{1}{B_0^2 + \widetilde{B}_r^2 + \widetilde{B}_y^2} = -\frac{\nabla_r (\widetilde{B}_r^2 + \widetilde{B}_y^2)}{(B_0^2 + \widetilde{B}_r^2 + \widetilde{B}_y^2)^2} \approx -\frac{2ik_r (\widetilde{B}_r^2 + \widetilde{B}_y^2)}{B^3} \\
\nabla_y \widetilde{\left(\frac{1}{B^2}\right)} &\approx -\frac{2ik_y (\widetilde{B}_r^2 + \widetilde{B}_y^2)}{B^3} \\
\nabla_\parallel \widetilde{\left(\frac{1}{B^2}\right)} &\approx -\frac{2\nabla_\parallel (\widetilde{B}_r^2 + \widetilde{B}_y^2)}{B^3}.
\end{aligned} \tag{D.8}$$

The first term of equation (D.1) can now be computed:

$$\begin{aligned}
\boldsymbol{\nabla}\cdot\left(\frac{\boldsymbol{B}\times\widetilde{\boldsymbol{C}}}{B^2}\right) =&\widetilde{\boldsymbol{C}}\cdot\boldsymbol{\nabla}\times\frac{\boldsymbol{B}}{B^2}-\frac{\boldsymbol{B}}{B^2}\cdot\boldsymbol{\nabla}\times\widetilde{\boldsymbol{C}}\\
=&\frac{\widetilde{\boldsymbol{C}}}{B^2}\cdot\boldsymbol{\nabla}\times\boldsymbol{B}-\widetilde{\boldsymbol{C}}\cdot\boldsymbol{B}\times\boldsymbol{\nabla}\frac{1}{B^2}-\frac{\boldsymbol{B}}{B^2}\cdot\boldsymbol{\nabla}\times\widetilde{\boldsymbol{C}}\\
\approx&\frac{\widetilde{\boldsymbol{C}}}{B^2}\cdot\left[\frac{B_*}{R_*}\sin\theta\boldsymbol{e}_r+\frac{B_*}{R_*}\cos\theta\boldsymbol{e}_y+\frac{B_*}{R_*}\frac{2-\hat{s}}{q}\boldsymbol{e}_\parallel\right]\\
&-\widetilde{\boldsymbol{C}}\cdot\left[\frac{2\sin\theta}{R_*B_*}\boldsymbol{e}_r+\frac{2\cos\theta}{R_*B_*}\boldsymbol{e}_y\right]-\frac{\boldsymbol{B}}{B^2}\cdot\boldsymbol{\nabla}\times\widetilde{\boldsymbol{C}}\\
\approx&\frac{\widetilde{\boldsymbol{C}}}{R_*B_*}\cdot\left[-\sin\theta\boldsymbol{e}_r-\cos\theta\boldsymbol{e}_y+\frac{2-\hat{s}}{q}\boldsymbol{e}_\parallel\right]-\frac{\boldsymbol{B}}{B^2}\cdot\boldsymbol{\nabla}\times\widetilde{\boldsymbol{C}}.
\end{aligned} \tag{D.9}$$

Keeping only linear terms, the second term of (D.1) yields:

$$\begin{aligned}
\boldsymbol{\nabla}\cdot\left(\widetilde{\left(\frac{\boldsymbol{B}}{B^2}\right)}\times\boldsymbol{C_0}\right) =&\boldsymbol{C_0}\cdot\boldsymbol{\nabla}\times\widetilde{\left(\frac{\boldsymbol{B}}{B^2}\right)}-\widetilde{\left(\frac{\boldsymbol{B}}{B^2}\right)}\cdot\boldsymbol{\nabla}\times\boldsymbol{C_0}\\
=&\frac{\boldsymbol{C_0}}{B^2}\cdot\boldsymbol{\nabla}\times\widetilde{\boldsymbol{B}}-\boldsymbol{C_0}\cdot\boldsymbol{B}\times\boldsymbol{\nabla}\widetilde{\left(\frac{1}{B^2}\right)}-\widetilde{\left(\frac{\boldsymbol{B}}{B^2}\right)}\cdot\boldsymbol{\nabla}\times\boldsymbol{C_0}\\
\approx&\frac{\boldsymbol{C_0}}{B^2}\cdot\left[-\nabla_\parallel\widetilde{B}_y\boldsymbol{e}_r+\nabla_\parallel\widetilde{B}_r\boldsymbol{e}_y+\left(ik_r\widetilde{B}_y-ik_y\widetilde{B}_r\right)\boldsymbol{e}_\parallel\right]\\
&-\frac{\widetilde{B}_r\boldsymbol{e}_r+\widetilde{B}_y\boldsymbol{e}_y}{B^2}\cdot\boldsymbol{\nabla}\times\boldsymbol{C_0}.
\end{aligned} \tag{D.10}$$

Divergence of the perturbation $\boldsymbol{E}\times\boldsymbol{B}$ flux

Equations (D.1) are now used in order to calculate the divergence of the ion perturbation $\boldsymbol{E}\times\boldsymbol{B}$ flux:

$$\boldsymbol{\nabla}\cdot\left(\widetilde{n\boldsymbol{V}_{E,i}}\right)=\boldsymbol{\nabla}\cdot\left(\frac{\boldsymbol{B}\times n\widetilde{\boldsymbol{\nabla}\phi}}{B^2}\right)+\boldsymbol{\nabla}\cdot\left(\frac{\widetilde{\boldsymbol{B}}}{B^2}\times n\boldsymbol{\nabla}_r\phi_0\right) \tag{D.11}$$

According to equation (D.9), the first term of equation (D.11) is

$$
\begin{aligned}
&\boldsymbol{\nabla}\cdot\left(\frac{\boldsymbol{B}\times\left(n_0\boldsymbol{\nabla}\widetilde{\phi}+\widetilde{n}\boldsymbol{\nabla}_r\phi_0\right)}{B^2}\right)\\
&\quad=\frac{n_0\boldsymbol{\nabla}\widetilde{\phi}+\widetilde{n}\boldsymbol{\nabla}_r\phi_0}{R_*B_*}\cdot\left[-\sin\theta\boldsymbol{e}_r-\cos\theta\boldsymbol{e}_y+\frac{2-\hat{s}}{q}\boldsymbol{e}_\parallel\right]\\
&\quad-\frac{\boldsymbol{B}}{B^2}\cdot\boldsymbol{\nabla}\times\left(n_0\boldsymbol{\nabla}\widetilde{\phi}+\widetilde{n}\boldsymbol{\nabla}_r\phi_0\right)\\
&\quad\approx\frac{n\widetilde{\phi}}{R_*B_*}\left(-ik_r\sin\theta-ik_y\cos\theta\right)-\frac{\widetilde{n}\nabla_r\phi_0}{R_*B_*}\sin\theta\\
&\quad-\frac{\boldsymbol{B}}{B^2}\cdot\begin{vmatrix}\boldsymbol{e}_r & \boldsymbol{e}_y & \boldsymbol{e}_\parallel\\ \nabla_r & \nabla_y & \nabla_\parallel\\ n_0\nabla_r\widetilde{\phi}+\widetilde{n}\nabla_r\phi_0 & n_0\nabla_y\widetilde{\phi} & n_0\nabla_\parallel\widetilde{\phi}\end{vmatrix}\\
&\quad=-\frac{n\widetilde{\phi}}{R_*B_*}\left(ik_r\sin\theta+ik_y\cos\theta\right)+\frac{ik_y}{B_*}\left(\widetilde{n}\frac{\partial\phi_0}{\partial r}-\frac{\partial n_0}{\partial r}\widetilde{\phi}\right)
\end{aligned}
\tag{D.12}
$$

With the help of equation (D.10), the second term gives

$$
\begin{aligned}
\boldsymbol{\nabla}\cdot\left(\frac{\widetilde{\boldsymbol{B}}}{B^2}\times n_0\boldsymbol{\nabla}_r\phi_0\right)\approx&\frac{n_0\boldsymbol{\nabla}_r\phi_0}{B^2}\cdot\left[-\nabla_\parallel\widetilde{B}_y\boldsymbol{e}_r+\nabla_\parallel\widetilde{B}_r\boldsymbol{e}_y+\left(ik_r\widetilde{B}_y-ik_y\widetilde{B}_r\right)\boldsymbol{e}_\parallel\right]\\
&-\frac{\widetilde{B}_r\boldsymbol{e}_r+\widetilde{B}_y\boldsymbol{e}_y}{B^2}\cdot\boldsymbol{\nabla}\times\left(n_0\boldsymbol{\nabla}_r\phi_0\right)\\
\approx&-\nabla_\parallel\widetilde{B}_y\frac{n_0\nabla_r\phi_0}{B^2}-\frac{\widetilde{B}_r\boldsymbol{e}_r+\widetilde{B}_y\boldsymbol{e}_y}{B^2}\cdot\begin{vmatrix}\boldsymbol{e}_r & \boldsymbol{e}_y & \boldsymbol{e}_\parallel\\ \nabla_r & \nabla_y & \nabla_\parallel\\ n_0\nabla_r\phi_0 & 0 & 0\end{vmatrix}\\
\approx&0
\end{aligned}
\tag{D.13}
$$

according to the drift ordering. The divergence of the perturbation $\boldsymbol{E}\times\boldsymbol{B}$ flux is thus:

$$
\boldsymbol{\nabla}\cdot\left(\widetilde{n\boldsymbol{V}_{E,i}}\right)\approx-\frac{n_0\widetilde{\phi}}{R_*B_*}\left(ik_r\sin\theta+ik_y\cos\theta\right)+\frac{ik_y}{B_*}\left(\widetilde{n}\frac{\partial\phi_0}{\partial r}-\frac{\partial n_0}{\partial r}\widetilde{\phi}\right)
\tag{D.14}
$$

Divergence of the perturbation diamagnetic drift

The same calculation for the divergence of the ion perturbation diamagnetic flux yields:

$$\boldsymbol{\nabla}\cdot\left(\widetilde{n\boldsymbol{V}_{*,i}}\right) = \boldsymbol{\nabla}\cdot\left(\frac{\boldsymbol{B}\times\widetilde{\boldsymbol{\nabla}p_i}}{eB^2}\right) + \boldsymbol{\nabla}\cdot\left(\frac{\widetilde{\boldsymbol{B}}}{B^2}\times\frac{\boldsymbol{\nabla}_r p_{0,i}}{e}\right) \tag{D.15}$$

for which the first term is

$$\begin{aligned}
\boldsymbol{\nabla}\cdot\left(\frac{\boldsymbol{B}\times\boldsymbol{\nabla}\widetilde{p}_i}{eB^2}\right) \approx & \frac{\widetilde{p}_i}{eR_*B_*}\left(-ik_r\sin\theta - ik_y\cos\theta\right) \\
& - \frac{\boldsymbol{B}}{B^2}\cdot\begin{vmatrix} \boldsymbol{e}_r & \boldsymbol{e}_y & \boldsymbol{e}_\parallel \\ \nabla_r & \nabla_y & \nabla_\parallel \\ \nabla_r\widetilde{p}_i & \nabla_y\widetilde{p}_i & \nabla_\parallel\widetilde{p}_i \end{vmatrix} \\
= & -\frac{\widetilde{p}_i}{eR_*B_*}\left(ik_r\sin\theta + ik_y\cos\theta\right)
\end{aligned} \tag{D.16}$$

and the second

$$\begin{aligned}
\boldsymbol{\nabla}\cdot\left(\frac{\widetilde{\boldsymbol{B}}}{B^2}\times\frac{\boldsymbol{\nabla}_r p_{0,i}}{e}\right) \approx & -\nabla_\parallel\widetilde{B}_y\frac{\nabla_r p_{0,i}}{eB^2} - \frac{\widetilde{B}_r\boldsymbol{e}_r + \widetilde{B}_y\boldsymbol{e}_y}{eB^2}\cdot\begin{vmatrix} \boldsymbol{e}_r & \boldsymbol{e}_y & \boldsymbol{e}_\parallel \\ \nabla_r & \nabla_y & \nabla_\parallel \\ \nabla_r p_{0,i} & 0 & 0 \end{vmatrix} \\
\approx & 0.
\end{aligned} \tag{D.17}$$

The divergence of the perturbed diamagnetic flux is thus:

$$\boldsymbol{\nabla}\cdot\left(\widetilde{n\boldsymbol{V}_{*,i}}\right) \approx -\frac{\widetilde{p}_i}{eR_*B_*}\left(ik_r\sin\theta + ik_y\cos\theta\right) \tag{D.18}$$

Divergence of the perturbation polarization flux

The divergence of the ion perturbation polarization drift is

$$\boldsymbol{\nabla}\cdot\left(\widetilde{nV_{p,i}}\right) = \frac{m_i}{e}\left[\boldsymbol{\nabla}\cdot\left(\frac{\boldsymbol{B}\times\widetilde{n\frac{d\boldsymbol{V}_i}{dt}}}{B^2}\right) + \boldsymbol{\nabla}\cdot\left(\frac{\widetilde{\boldsymbol{B}}}{B^2}\times n_0\frac{d\boldsymbol{V}_{0,i}}{dt}\right)\right] \tag{D.19}$$

The background drift velocity is due to the radial gradients of ϕ_0 and $p_{0,i}$:

$$\begin{aligned}
\boldsymbol{V}_{0,i} = \boldsymbol{V}_{E,0,i} + \boldsymbol{V}_{*,0,i} =& \frac{\boldsymbol{B} \times \boldsymbol{\nabla}_r \phi_0}{B^2} + \frac{\boldsymbol{B} \times \boldsymbol{\nabla}_r p_{0,i}}{e n_0 B^2} \\
=& \frac{1}{B^2} \begin{vmatrix} \boldsymbol{e}_r & \boldsymbol{e}_y & \boldsymbol{e}_\parallel \\ 0 & 0 & B \\ \nabla_r \phi_0 + \frac{1}{e n_0} \nabla_r p_{0,i} & 0 & 0 \end{vmatrix} \\
=& \frac{1}{B} \left(\frac{\partial \phi_0}{\partial r} + \frac{1}{e n_0} \frac{\partial p_{0,i}}{\partial r} \right) \boldsymbol{e}_y.
\end{aligned} \tag{D.20}$$

Thus

$$\begin{aligned}
\frac{d\boldsymbol{V}_{0,i}}{dt} &= \frac{\partial \boldsymbol{V}_{0,i}}{\partial t} + \left(\boldsymbol{V}_{0,i} \cdot \boldsymbol{\nabla} \right) \boldsymbol{V}_{0,i} \\
&= V_{0,i} \nabla_y \boldsymbol{V}_{0,i} \\
&\approx 0
\end{aligned} \tag{D.21}$$

in the drift ordering, such that the second term on the right-hand side of equation (D.19) vanishes (note the fact that $d\widetilde{\boldsymbol{V}}_0/dt$ is not exactly zero is an effect of the toroidal geometry). $\widetilde{\boldsymbol{V}}_i$ is now calculated

$$\begin{aligned}
\widetilde{\boldsymbol{V}}_i \approx& \frac{\boldsymbol{B} \times \boldsymbol{\nabla} \widetilde{\phi}}{B^2} + \frac{\boldsymbol{B} \times \boldsymbol{\nabla} \widetilde{p}_i}{e n B^2} \\
=& \frac{1}{B^2} \begin{vmatrix} \boldsymbol{e}_r & \boldsymbol{e}_y & \boldsymbol{e}_\parallel \\ 0 & 0 & B \\ \nabla_r \widetilde{\phi} + \frac{1}{en} \nabla_r \widetilde{p}_i & \nabla_y \widetilde{\phi} + \frac{1}{en} \nabla_y \widetilde{p}_i & \nabla_\parallel \widetilde{\phi} + \frac{1}{en} \nabla_\parallel \widetilde{p}_i \end{vmatrix} \\
=& \left(-\frac{i k_y}{B} \boldsymbol{e}_r + \frac{i k_r}{B} \boldsymbol{e}_y \right) \left(\widetilde{\phi} + \frac{\widetilde{p}_i}{en} \right)
\end{aligned} \tag{D.22}$$

together with its time derivative

$$\begin{aligned}
\frac{d\widetilde{\boldsymbol{V}}_i}{dt} =& \frac{\partial \widetilde{\boldsymbol{V}}_i}{\partial t} + \left(\boldsymbol{V}_{0,i} \cdot \boldsymbol{\nabla} \right) \widetilde{\boldsymbol{V}}_i + (\widetilde{\boldsymbol{V}}_i \cdot \boldsymbol{\nabla}) \boldsymbol{V}_{0,i} \\
=& - i\omega \widetilde{\boldsymbol{V}}_i + i k_y V_{0,i} \widetilde{\boldsymbol{V}}_i + \left(\widetilde{V}_{i,r} \nabla_r + \widetilde{V}_{i,y} \nabla_y \right) V_{0,i} \boldsymbol{e}_y \\
\approx& - i\omega \widetilde{\boldsymbol{V}}_i + i k_y V_{0,i} \widetilde{\boldsymbol{V}}_i.
\end{aligned} \tag{D.23}$$

The divergence of the perturbation polarization flux is then

$$
\begin{aligned}
\boldsymbol{\nabla}\cdot\left(\widetilde{nV_{p,i}}\right) \approx & \frac{m_i}{e}\boldsymbol{\nabla}\cdot\left(\frac{\boldsymbol{B}\times \widetilde{n\frac{d\boldsymbol{V}}{dt}}}{B^2}\right) \\
= & \frac{m_i}{e}\frac{n_0}{R_* B_*}\left[-\sin\theta\left(\widetilde{\frac{d\boldsymbol{V}}{dt}}\right)_r - \cos\theta\left(\widetilde{\frac{d\boldsymbol{V}}{dt}}\right)_y\right] \\
& -\frac{m_i}{e}\frac{\boldsymbol{B}}{B^2}\cdot\begin{vmatrix} \boldsymbol{e}_r & \boldsymbol{e}_y & \boldsymbol{e}_\parallel \\ \nabla_r & \nabla_y & \nabla_\parallel \\ \left(\widetilde{n\frac{d\boldsymbol{V}}{dt}}\right)_r & \left(\widetilde{n\frac{d\boldsymbol{V}}{dt}}\right)_y & 0 \end{vmatrix} \\
= & \frac{n_0}{\omega_{ci}R_*}\left[\left(-i\omega + ik_y V_0\right)\left(-\sin\theta\widetilde{V}_r - \cos\theta\widetilde{V}_y\right)\right] \\
& -\frac{1}{\omega_{ci}}\left[\nabla_r\left(\widetilde{n\frac{d\boldsymbol{V}}{dt}}\right)_y - \nabla_y\left(\widetilde{n\frac{d\boldsymbol{V}}{dt}}\right)_r\right]. \\
\approx & \frac{n_0}{\omega_{ci}R_*}\left[i\omega\left(\sin\theta\widetilde{V}_r + \cos\theta\widetilde{V}_y\right)\right] \\
& -\frac{1}{\omega_{ci}}\left[\nabla_r\left(\left(-i\omega + ik_y V_0\right) n_0\widetilde{V}_y\right) - \nabla_y\left(\left(-i\omega + ik_y V_0\right) n_0\widetilde{V}_r\right)\right] \\
\approx & i\frac{\omega}{\omega_{ci}}\frac{n_0}{R_*}\left(\sin\theta\widetilde{V}_r + \cos\theta\widetilde{V}_y\right) \\
& -\frac{1}{\omega_{ci}}\left(-i\omega + ik_y V_0\right)\left[ik_r n_0\widetilde{V}_y + \widetilde{V}_y\nabla_r n_0 - ik_y n_0\widetilde{V}_r\right] \\
\approx & \frac{1}{\omega_{ci}}\frac{n_0}{B_*}\left(k_r^2 + k_y^2\right)\left(\widetilde{\phi} + \frac{\widetilde{p}_i}{en_0}\right)\left(-i\omega + \frac{ik_y}{B}\left(\nabla_r\phi_0 + \frac{\nabla_r p_{0,i}}{en_0}\right)\right).
\end{aligned}
\tag{D.24}
$$

Divergence of the perturbation flux due to viscosity

According to ref. [5], the components of the ion gyroviscous tensor $\overleftrightarrow{\pi}$ we are interested in are:

$$
\begin{aligned}
\pi_{rr} &= -\pi_{yy} = -\frac{p_i}{2\omega_{ci}}\left(\frac{\partial V_r}{\partial y} + \frac{\partial V_y}{\partial r}\right) \\
\pi_{ry} &= \pi_{yr} = \frac{p_i}{2\omega_{ci}}\left(\frac{\partial V_r}{\partial r} - \frac{\partial V_y}{\partial y}\right)
\end{aligned}
\tag{D.25}
$$

and $\pi_{\|r}$, $\pi_{\|y}$ are of the same order as π_{ry}. The radial and y component of $\boldsymbol{\nabla}\cdot\overleftrightarrow{\pi}$ are

$$\begin{aligned}(\boldsymbol{\nabla}\cdot\overleftrightarrow{\pi})_r &= \nabla_r\pi_{rr}+\nabla_y\pi_{yr}+\nabla_\|\pi_{\|r}\approx\nabla_r\pi_{rr}+\nabla_y\pi_{yr}\\ (\boldsymbol{\nabla}\cdot\overleftrightarrow{\pi})_y &= \nabla_r\pi_{ry}+\nabla_y\pi_{yy}+\nabla_\|\pi_{\|y}\approx\nabla_r\pi_{ry}+\nabla_y\pi_{yy}.\end{aligned}\tag{D.26}$$

A full calculation of the perturbation flux due to viscosity is very tedious. Therefore, only the final result where only terms in the drift ordering presented in section 3.3.1 are kept is given here:

$$\begin{aligned}\boldsymbol{\nabla}\cdot\left(\widetilde{nV_{\pi,i}}\right) =&\boldsymbol{\nabla}\cdot\left(\frac{\boldsymbol{B}\times\widetilde{(\boldsymbol{\nabla}\cdot\overleftrightarrow{\pi}_i)}}{eB^2}\right)\\ &\approx-\frac{ik_y}{\omega_{ci}B}\frac{n_0}{B_*}\left(k_r^2+k_y^2\right)\left(\widetilde{\phi}+\frac{\widetilde{p}_i}{en_0}\right)\left(\nabla_r\phi_0+\frac{\nabla_r p_{0,i}}{en_0}\right).\end{aligned}\tag{D.27}$$

This is exactly the same as the convective part of equation (D.24) except for the sign. The convective part of the polarization flux divergence is thus cancelled by the the divergence of the flux due to viscosity. A similar result is obtained in refs. [65, 71].

The divergence of the total perturbation flux can now be written:

$$\begin{aligned}\boldsymbol{\nabla}\cdot\left(\widetilde{nV_i}\right) = \frac{ik_y}{B_*}\left(\widetilde{n}\nabla_r\phi_0-\widetilde{\phi}\nabla_r n_0\right)-i\frac{n_0}{B_*}\left(\widetilde{\phi}+\frac{\widetilde{p}_i}{en_0}\right)\times\\ \times\left[\frac{k_r\sin\theta+k_y\cos\theta}{R_*}+\omega\frac{k_r^2+k_y^2}{\omega_{ci}}\right]\end{aligned}\tag{D.28}$$

Since the different terms of (D.28) have been calculated seperately, it is usefull to check whether some terms can neglected according to the drift ordering. The first term is of order $k_\perp/L_\perp$, while the second terms contains parts of order $k_\perp/R$ ($\sin\theta$ and $\cos\theta$ terms) and parts of order $k_\perp^3/L_\perp$. Terms in $\sin\theta$ and $\cos\theta$ can thus be neglected, such that the divergence of the ion perturbation flux is

$$\boldsymbol{\nabla}\cdot\left(\widetilde{n\boldsymbol{V}_i}\right)=\frac{ik_y}{B_*}\left(\widetilde{n}\nabla_r\phi_0-\widetilde{\phi}\nabla_r n_0\right)-i\omega\frac{n_0\left(k_r^2+k_y^2\right)}{\omega_{ci}B_*}\left(\widetilde{\phi}+\frac{\widetilde{p}_i}{en_0}\right).\tag{D.29}$$

The divergence of the perpendicular current also needs to be calculated. According to equation (3.43), it is

$$\begin{aligned}\boldsymbol{\nabla}\cdot\widetilde{\boldsymbol{j}}_\perp =&\boldsymbol{\nabla}\cdot\left[en\boldsymbol{V}_{p,i}+\widetilde{en\boldsymbol{V}_{\pi,i}}+en\boldsymbol{V}_{*,i}-en\boldsymbol{V}_{*,e}\right]\\ =&-i\omega\frac{k_r^2+k_y^2}{B_*\omega_{ci}}\left(en_0\widetilde{\phi}+\widetilde{p}_i\right)-i\frac{\widetilde{p}_i+\widetilde{p}_e}{R_*B_*}\left(k_r\sin\theta+k_y\cos\theta\right),\end{aligned}\tag{D.30}$$

where the electron polarization and viscous drifts have been neglected due to the smallness of the electron mass and viscous effects compared to the ion ones. Note that this last result cannot be simplified on the base of the drift ordering. In equation (D.29), the $\boldsymbol{E} \times \boldsymbol{B}$ flux brings the largest contribution, but in equation (D.30) electron and ion $\boldsymbol{E} \times \boldsymbol{B}$ fluxes cancel out.

Appendix E

Eigen-value equation for density perturbations

From equation (3.32), the electric potential perturbation can be expressed as a function of the density perturbation:

$$\hat{\phi} = \hat{n}\frac{\alpha K_y F + \bar{\omega}\left(1 + K^2\right) + i\bar{\nu}_{\parallel}}{\alpha K_y - \alpha\bar{\omega}K^2} \tag{E.1}$$

with $F = \frac{L_n}{L_\phi}$ and $K^2 = K_r^2 + K_y^2$. By elimination of $\hat{\phi}$ between equations (E.1) and (3.45), one obtains

$$\begin{aligned}
&\frac{\alpha K_y G_n - \bar{\omega}\left[1 + (1+\alpha)\,K^2\right] - i\bar{\nu}_{\parallel}}{\alpha K_y - \alpha\bar{\omega}K^2}\nabla_{\parallel}^2\hat{n} = \\
&\qquad \frac{m_R}{\alpha L_n^2}\left[i0.51\bar{\nu}_e + (\bar{\omega} - \alpha K_y G_p)\left(1 + \frac{\beta}{m_R K^2}\right) - \alpha K_y G_n\frac{\beta}{m_R K^2}\right]\times \\
&\qquad\qquad \times\left[K^2\bar{\omega}\frac{\alpha K_y\,(1+\alpha F) + \alpha\bar{\omega} + i\alpha\bar{\nu}_{\parallel}}{\alpha K_y - \alpha\bar{\omega}K^2} + \frac{L_n}{R}\,(1+\alpha)\,f(\theta)\right]\hat{n}
\end{aligned}$$

or

$$\begin{aligned}
&\left[\alpha K_y G_n - \bar{\omega}\left[1 + (1+\alpha)\,K^2\right] - i\bar{\nu}_{\parallel}\right]\nabla_{\parallel}^2\hat{n} = \\
&\qquad \frac{m_R}{L_n^2}\left[i0.51\bar{\nu}_e + (\bar{\omega} - \alpha K_y G_p)\left(1 + \frac{\beta}{m_R K^2}\right) - \alpha K_y G_n\frac{\beta}{m_R K^2}\right]\times \\
&\qquad \times\left[\alpha K^2\bar{\omega}\left[K_y\,(1+\alpha F) + \bar{\omega} + i\bar{\nu}_{\parallel}\right] + \frac{L_n}{R}\,(1+\alpha)\,f(\theta)\left[K_y - \bar{\omega}K^2\right]\right]\hat{n}
\end{aligned} \tag{E.2}$$

with $G_p = \frac{L_n}{L_{pe}} - F$, $G_n = 1 - F$ and $f(\theta) = K_r \sin\theta + K_y \cos\theta$. By estimating the order of magnitude of the last factor on the right-hand side of equation (E.2), one sees that its first term is of the order $K_\perp^4$ while the second has a part of the order $K_\perp^2 L_n/R$ and a part of the order $K_\perp^4 L_n/R$ ($f(\theta)$ is of order $K_\perp$). The latter part can thus be neglected according to the ordering. In order to find a shorter form for equation (E.2), some functions are introduced

$$\begin{aligned}
S(\bar{\omega}, K_\perp) &= m_R \left(\frac{qR}{L_n}\right)^2 \times \\
&\qquad \times \frac{(\bar{\omega} - \alpha K_\perp G_p)\left(1 + \frac{\beta}{2m_R K_\perp^2}\right) - \alpha K_\perp G_n \frac{\beta}{2m_R K_\perp^2} + i0.51\bar{\nu}_e}{\bar{\omega}\big[1 + (1+\alpha)\, 2K_\perp^2\big] - \alpha K_\perp G_n + i\bar{\nu}_\parallel} \\
T_1(\bar{\omega}, K_\perp) &= 2\alpha K_\perp^2 \bar{\omega} \left\{K_\perp (1 + \alpha F) + \bar{\omega} + i\bar{\nu}_\parallel\right\} \\
T_3(\bar{\omega}, K_\perp) &= K_\perp \frac{L_n}{R} (1 + \alpha)
\end{aligned} \tag{E.3}$$

With the previous remark and definition (3.24), this allows to rewrite (E.2) in the form

$$\frac{\partial^2 \hat{n}}{\partial \theta^2} + S\big(T_1 + T_3 f(\theta)\big)\hat{n} = 0$$

or

$$\frac{\partial^2 N(\vartheta)}{\partial \vartheta^2} + S\big(T_1 + T_3 K_\perp \sqrt{2}\cos\vartheta\big) N(\vartheta) = 0 \tag{E.4}$$

with $\vartheta = \theta - \frac{\pi}{4}$. $N(\vartheta)$ corresponds to $N(l)$ in definition (3.21) with $\partial l = qR\partial\vartheta$ (see equation (3.24)).

Appendix F

Average perpendicular particle flux

The average radial component of the perpendicular electron flux due to unstable modes is calculated according to equation (3.50) (the ion flux is identical since ambipolarity is assumed). Neglecting electron inertia and viscosity, the electron perturbation velocity reads

$$\begin{aligned}\widetilde{V}_{e,r} \approx& \left[\frac{\boldsymbol{B} \times \left(\boldsymbol{\nabla}\widetilde{\phi} - \frac{1}{en_0}\boldsymbol{\nabla}\widetilde{p}_e\right)}{B^2}\right]_r \\ =& -\frac{ik_y}{B}\left(\widetilde{\phi} - \frac{T_e}{en_0}\widetilde{n}\right).\end{aligned} \tag{F.1}$$

Introducing (F.1) into (3.50) yields

$$\begin{aligned}\langle\Gamma_{\perp,r}\rangle =& \widetilde{n}\widetilde{V}_r^{\star} + \widetilde{n}^{\star}\widetilde{V}_r \\ =& \frac{ik_y}{B}\left[\widetilde{n}\left(\widetilde{\phi}^{\star} - \frac{T_e}{en_0}\widetilde{n}^{\star}\right) - \widetilde{n}^{\star}\left(\widetilde{\phi} - \frac{T_e}{en_0}\widetilde{n}\right)\right] \\ =& i\alpha K_y n_0 v_{th,i}\left[\hat{n}\hat{\phi}^{\star} - \hat{n}^{\star}\hat{\phi}\right].\end{aligned} \tag{F.2}$$

Using equation (E.1), $\hat{n}$ can be written as a function of $\hat{\phi}$:

$$\begin{aligned}\hat{n} =& \frac{\alpha K_{\perp}\left(1 - 2\bar{\omega}_r K_{\perp}\right) - i\alpha\bar{\gamma}2K_{\perp}^2}{\alpha K_{\perp}F + \bar{\omega}_r\left(1 + 2K_{\perp}^2\right) + i\left(\bar{\gamma}\left(1 + 2K_{\perp}^2\right) + \bar{\nu}_{\parallel}\right)}\hat{\phi} \\ =& \frac{\mathcal{A} - i\mathcal{B}}{\mathcal{D}}\hat{\phi}\end{aligned} \tag{F.3}$$

with $\bar{\omega}_r$ and $\bar{\gamma}$ the real and imaginary parts of $\bar{\omega}$ and

$$\begin{aligned}
\mathcal{A} =& \alpha K_\perp \Big[(1 - 2\bar{\omega}_r K_\perp) \left[\alpha K_\perp F + \alpha \bar{\omega}_r \left(1 + 2K_\perp^2\right)\right] \\
& \qquad\qquad - 2\bar{\gamma} K_\perp \left[\bar{\gamma}\left(1 + 2K_\perp^2\right) + \bar{\nu}_\parallel\right]\Big] \\
\mathcal{B} =& \alpha K_\perp \Big[2\bar{\gamma} K_\perp \left[\alpha K_\perp F + \bar{\omega}_r \left(1 + 2K_\perp^2\right)\right] \\
& \qquad\qquad + (1 - 2\bar{\omega}_r K_\perp) \left[\bar{\gamma}\left(1 + 2K_\perp^2\right) + \bar{\nu}_\parallel\right]\Big] \\
\mathcal{D} =& \Big[\alpha K_\perp F + \bar{\omega}_r \left(1 + 2K_\perp^2\right)\Big]^2 + \Big[\bar{\gamma}\left(1 + 2K_\perp^2\right) + \bar{\nu}_\parallel\Big]^2 .
\end{aligned} \tag{F.4}$$

The real and imaginary parts of $\hat{n}$ can be expressed as functions of $\hat{\phi}$:

$$\begin{aligned}
\mathrm{Re}\,\hat{n} =& \frac{\mathcal{A}}{\mathcal{D}} \mathrm{Re}\,\hat{\phi} + \frac{\mathcal{B}}{\mathcal{D}} \mathrm{Im}\,\hat{\phi} \\
\mathrm{Im}\,\hat{n} =& \frac{\mathcal{A}}{\mathcal{D}} \mathrm{Im}\,\hat{\phi} - \frac{\mathcal{B}}{\mathcal{D}} \mathrm{Re}\,\hat{\phi}
\end{aligned} \tag{F.5}$$

such that equation (F.2) becomes

$$\langle \Gamma_{\perp,r} \rangle = 2\alpha K_\perp n_0 v_{th,i} \frac{\mathcal{B}}{\mathcal{D}} \left|\hat{\phi}\right|^2 \tag{F.6}$$

and, assuming a purely diffusive flux, the diffusivity is given by

$$\begin{aligned}
D_\perp =& -\frac{\langle \Gamma_{\perp,r} \rangle}{\nabla_r n_0} \\
=& 2\alpha K_\perp L_n v_{th,i} \frac{\mathcal{B}}{\mathcal{D}} \left|\hat{\phi}\right|^2
\end{aligned} \tag{F.7}$$

or

$$\begin{aligned}
D_\perp =& 2\alpha K_\perp L_n v_{th,i} \frac{\mathcal{B}}{\mathcal{D}} \left|\hat{\phi}\right|^2 \\
=& \frac{2\alpha^2 K_\perp^2 L_n v_{th,i} \Big[\bar{\gamma}\Big(1 + 2K_\perp^2 \left(1 + \alpha F\right)\Big) + \left(1 - 2\bar{\omega}_r K_\perp\right)\bar{\nu}_\parallel\Big] \left|\hat{\phi}\right|^2}{\Big[\alpha K_\perp F + \bar{\omega}_r \left(1 + 2K_\perp^2\right)\Big]^2 + \Big[\bar{\gamma}\left(1 + 2K_\perp^2\right) + \bar{\nu}_\parallel\Big]^2} .
\end{aligned} \tag{F.8}$$

Appendix G

Validity of the assumption of isothermal ions and electrons

The validty of the assumption of isothermal ions and electrons, which gives $\widetilde{\boldsymbol{\nabla} p_s} \approx T_s \widetilde{\boldsymbol{\nabla} n}$, is now discussed. The scalar pressure perturbation is governed by the heat balance equation (eq. (3.8)). For electrons, by introducing $s_e = \ln(T_e^{3/2}/n)$, it can be rewritten:

$$\begin{aligned}
\widetilde{nT_e \frac{ds_e}{dt}} =& -\widetilde{\boldsymbol{\nabla} \cdot \boldsymbol{q}_{H,e}} - \pi_{jk} \frac{\partial V_{e,j}}{\partial x_k} + Q_{H,e} \\
\approx& - \nabla_\parallel \left(-\widetilde{\kappa_{\parallel,e} \nabla_\parallel T_e} \right) \\
=& \kappa_{\parallel,e} \widetilde{\nabla_\parallel^2 T_e} \\
=& \kappa_{\parallel,e} \left(\nabla_\parallel^2 \widetilde{T}_e + 2 \frac{ik_y}{B} \frac{\mu_0}{k_r^2 + k_y^2} \nabla_r T_{e,0} \nabla_\parallel \widetilde{j}_\parallel \right) \\
=& nT_e \left[\frac{\partial s_e}{\partial t} + \widetilde{(\boldsymbol{V}_e \cdot \boldsymbol{\nabla})\, s_e} \right] \\
=& nT_e \left[\frac{3}{2} \frac{1}{T_e} \frac{\partial \widetilde{T}_e}{\partial t} - \frac{1}{n} \frac{\partial \widetilde{n}}{\partial t} + V_{e,0,y} \nabla_y \widetilde{s}_e + \widetilde{V}_{e,r} \nabla_r s_{e,0} \right] \\
=& - T_e \widetilde{n} \left[-i\omega + \frac{ik_y}{eB} \left(e \nabla_r \phi_0 + \frac{T_e}{L_{P_e}} \right) \right] \\
&+ \frac{ik_y}{eB} \left(e\widetilde{\phi} - \frac{T_e \widetilde{n}}{n} \right) \left(\frac{3}{2} \frac{p_e}{L_{p_e}} - \frac{5}{2} \frac{p_e}{L_n} \right) \\
&+ \frac{3}{2} n \widetilde{T}_e \left[-i\omega + \frac{ik_y}{eB} \left(e \nabla_r \phi_0 + \frac{5}{3} \frac{T_e}{L_n} \right) \right], \qquad \text{(G.1)}
\end{aligned}$$

where it was taken into account that $\widetilde{\boldsymbol{\nabla} \cdot \boldsymbol{q}_{H,e}}$ is the dominant term on the right-hand side of equation (G.1). Thus

$$\begin{aligned}
\kappa_{\parallel,e}&\Bigg[\underbrace{\nabla_\parallel^2 \hat{T}_e}_{1} + \underbrace{2K_\perp \bar{\omega}\frac{\beta}{L_n L_{T_e}}\left(\alpha\hat{\phi}+\hat{n}\right)}_{2}\Bigg] \\
=&\omega_0 n\Bigg[\underbrace{\hat{n}\left(i\bar{\omega}+iK_\perp\left(\frac{L_n}{L_{p_e}}-\frac{L_n}{L_\phi}\right)\right)}_{3}+\underbrace{iK_\perp\left(\hat{\phi}-\hat{n}\right)\left(\frac{3}{2}\frac{L_n}{L_{p_e}}-\frac{5}{2}\right)}_{4} \\
&+\underbrace{\frac{3}{2}\hat{T}_e\left(-i\bar{\omega}+iK_\perp\left(\frac{5}{3}-\frac{L_n}{L_\phi}\right)\right)}_{5}\Bigg]. \qquad \text{(G.2)}
\end{aligned}$$

From this last equation, an approximation of the relative amplitudes of $\hat{T}_e$ and $\hat{n}$ can be estimated by comparing terms 1 and 3

$$\hat{T}_e \approx \frac{(qR)^2}{\kappa_{\parallel,e}}\omega_0 n K_\perp \hat{n}. \qquad \text{(G.3)}$$

For $T_e = 50\,eV$, $n = 5\cdot 10^{18}\,m^{-3}$ and $q = 3$, which are typical conditions at the very edge of TEXTOR, one obtains $\hat{T}_e \approx 0.13\,\hat{n}$, and this ratio diminishes with the square of the temperature. Terms 4 and 5 can be neglected with respect to term 3, respectively because $\hat{\phi} \sim \hat{n}$ and because of the small ratio $\hat{T}_e/\hat{n}$. Term 2 is neglected since $2K_\perp\bar{\omega}\beta/(L_n L_{T_e}) \ll 1/(qR)^2$. The assumption $\widetilde{\boldsymbol{\nabla} p_e} \approx T_e \widetilde{\boldsymbol{\nabla} n}$ is thus valid for $T_e \gtrsim 50\,eV$. The same reasoning can be applied for ions. It yields

$$\hat{T}_i \approx \frac{(qR)^2}{\kappa_{\parallel,i}}\omega_0 n K_\perp \hat{n}. \qquad \text{(G.4)}$$

For $T_i = 50\,eV$, $n = 5\cdot 10^{18}\,m^{-3}$ and $q = 3$, it gives $\hat{T}_i \approx 4.3\,\hat{n}$, and for the same conditions but with $T_i = 100\,eV$, it provides $\hat{T}_i \approx \hat{n}$ (the ratio $\hat{T}_i/\hat{n}$ further decreases with T_i). Consequently, the approximation $\widetilde{\boldsymbol{\nabla} p_i} \approx T_i \widetilde{\boldsymbol{\nabla} n}$ is not valid for $T_i \lesssim 100\,eV$. It is interesting to see what gives the opposite extreme, i.e. adiabatic ions. In this case, $d\widetilde{s}_i/dt = 0$ and $\boldsymbol{\nabla}\widetilde{p}_i = 5/3 T_i \boldsymbol{\nabla}\widetilde{n}$. This corresponds to the equation of state of a monoatomic gas in thermodynamics.

Appendix H

Correction of diamagnetic energy measurement perturbations due to toroidal magnetic field variations

A variation of the magnetic field produces an error on the measurement of $\Delta\phi$ as shown in fig. H.1. A corrected flux variation $\Delta\phi_{cor}$ is obtained by subtracting from $\Delta\phi_{meas}$, the measured flux difference, a quantity proportional to V_{loop1}, the voltage induced in the loop with the shortest rise time. Namely $\Delta\phi_{cor} = \Delta\phi_{meas} - K_{cor}V_{loop1}$, where K_{cor} is the correction coefficient. Figure H.2 shows the diamagnetic energy obtained for the plasma discharge of fig. H.1 without and with correction. It is clear from this figure that it is a necessary correction.

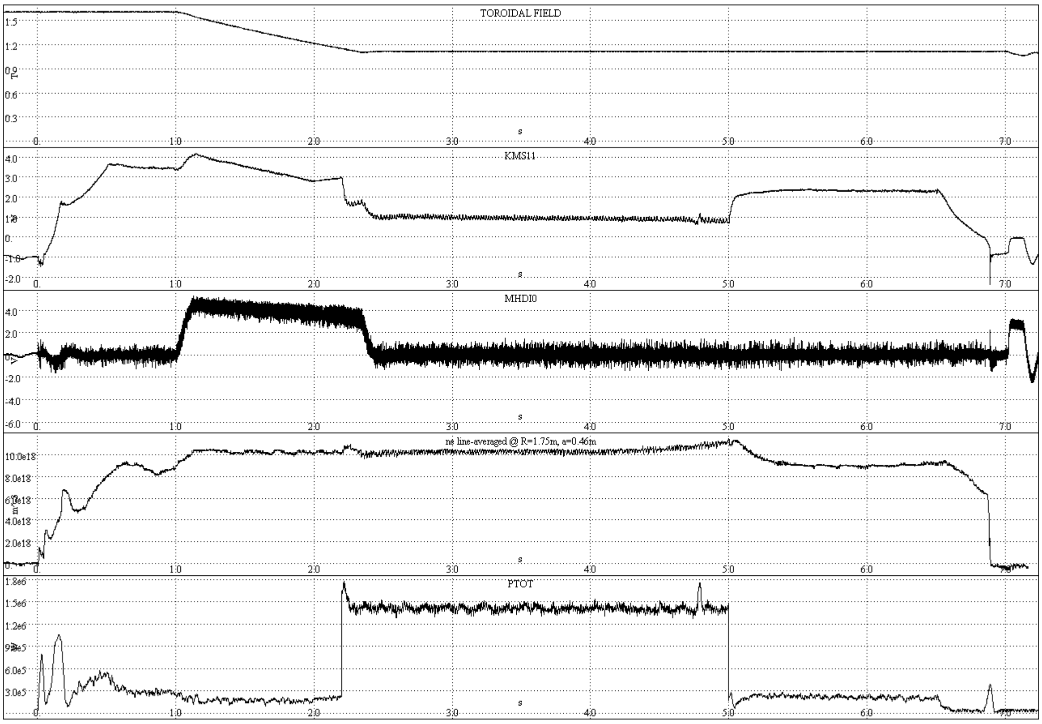

Figure H.1: From the top to the bottom: the magnetic field, the integrated difference of voltages induced in the two diamagnetic loops (signal KMS11), the voltage induced in the loop with the shortest rise time (signal MHDI0), the line averaged density and the total heating power for discharge n° 97258 at TEXTOR. A large variation of the KMS11 and MHDI0 signals is observed at times $t = 1\,s$ and $t = 2.3\,s$, corresponding to the pertubations induced in the diamagnetic measurements by a non zero second time derivative of the magnetic field.

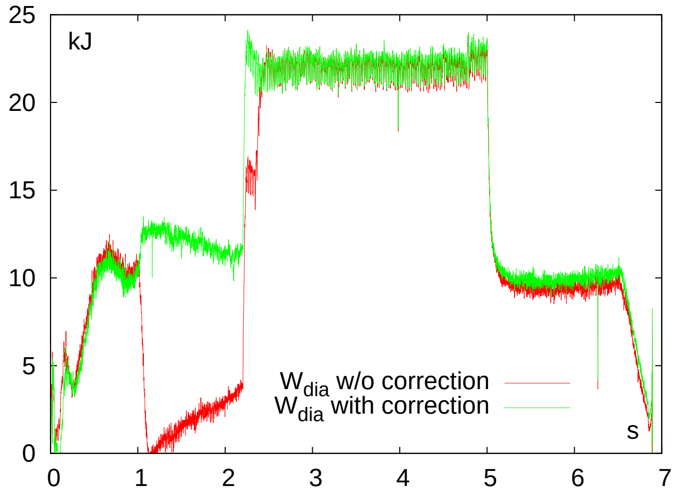

Figure H.2: Diamagnetic energy obtained wihtout and with correction for the variation of the toroidal magnetic field for shot 97258 at TEXTOR. One can see that the correction modifies significantly the diamagnetic energy from $t = 1\,s$ to $t = 2.3\,s$, i.e. during the phase where the magnetic field decreases (see fig. H.1)

Bibliography

[1] Abdullaev S.S., Finken K.H., Kaleck A. and Spatschek K.H., 1998 *Phys. Plasmas* **5** 196

[2] Abramowitz M. and Stegun I. A., 1970 *Handbook of mathematical functions* Dover Public., New York, Ninth Printing 722

[3] Baker D.R. and Rosenbluth M.N., 1998 *Phys. Plasmas* **5** 2936

[4] Bertschinger G. *et al*, 1999 *Physica Scripta* **T83** 132

[5] Braginskii S.I., 1963 *Reviews of Plasma Physics*, edited by Leontovich M. (Consultants Bureau, New York), Vol. 1, 193

[6] Capes H., Samain A., Ghendrih Ph. and Nguyen F., 1992 *Contrib. Plasma Phys.* **32** 192

[7] Lopes Cardozo N.J., 1995 *Plasma Phys. Control. Fusion* **37** 799

[8] Chen F. F., 1984 *Introduction to Plasma Physics and Controlled Fusion* (Plenum Press, New York)

[9] Chodura R., 1988 *Contrib. Plasma Phys.* **28** 303

[10] Connor J.W. and Pogutse O.P., 2001 *Plasma Phys. Control. Fusion* **43** 155

[11] Cordey J.G. *et al*, 1998 *JET Report: JET-P(98)01*

[12] Dominguez R.R., 1993 *Phys. Fluids B* **5** 1782

[13] Dupree T.H., 1967 *Phys. Fluids* **10** 1049

[14] Evans T.E., DeGrassie J.S., Jackson G.L. *et al.*, 1987 *J. Nucl. Mater.* **145-147** 812

[15] Finken K. H., Abdullaev S.S., Kaleck A. and Wolf G.H., 1999, *Nucl. Fusion* **39** 637

[16] Finken K. H., Abdullaev S. S., Biel W. *et al.*, 2004 *Plasma Phys. Control. Fusion* **46** B143

[17] Finken K. H. *et al.*, 2005 *The structure of magnetic field in the TEXTOR-DED* (Forschungszentrum Jülich GmbH) ISBN 3-89336-418-8

[18] Fundamenski W., 2005 *Plasma Phys. Control. Fusion* **47** R163-R208

[19] Garbet X. *et al.*, 2003 *Phys. Rev. Lett.* **91** 035001

[20] Ghendrih Ph., Capes H., Nguyen F. and Samain A., 1992 *Contrib. Plasma Phys.* **32** 179

[21] Ghendrih Ph., Grosman A. and Capes H., 1996 *Plasma Phys. Control. Fusion* **38** 1653

[22] Ghendrih Ph., Bécoulet M., Colas L. *et al.*, 2002 *Nucl. Fusion* **42** 1221

[23] Guzdar P.N. *et al*, 1993 *Phys. Fluids B* **5** 3712

[24] Harting D. and Reiter D., 2005 *3D Monte-Carlo-Simulation der ergodisierten Randschicht von TEXTOR-DED* (Forschungszentrum Jülich GmbH) ISSN 0944-2952

[25] Hinton F.L. and Hazeltine R.D., 1976 *Rev. Mod. Phys.* **48** 239

[26] Hintz E. and Schweer B., 1995 *Plasma Phys. Control. Fusion* **37** A87

[27] Horton W., 1985 *Plasma Phys. Control. Fusion* **27** 937

[28] Horton W., Hong B.G. and Tang W.M., 1988 *Phys. Fluids* **31** 2971

[29] Hutchinson I.H., 1987 *Principles of plasma diagnostics*, Cambridge University Press

[30] Takizuka T. for the ITPA H-mode Power Threshold Database Working Group, 2004 *Plasma Phys. Control. Fusion* **46** A227

[31] Joffrin E. and Defrasne P., 2002 *Review of Scientific Instruments* **73** 2266

[32] Kadomtsev B.B. and Pogutse O.P., 1978 *Plasma Physics and Controlled Nuclear Fusion Research, Proceedings*, 7th IAEA Conference, Innsbruck (International Atomic Energy Agency, Vienna) **1** 649

[33] Kaganovich I. and Rozhansky V., 1998 *Phys. Plasmas* **5** 3901

[34] Kalupin D., Tokar M.Z., Unterberg B., Loozen X. and Pilipenko D., 2005 *Nucl. Fusion* **45** 468

[35] Kalupin D., Tokar M.Z., Unterberg B., Loozen X., Pilipenko D., Zagorski R. and TEXTOR Contributors, 2006 *Phys. Plasmas* **13** 032504

[36] Kalupin D., Tokar M.Z., Unterberg B., Loozen X., Pilipenko D., Zagorski R. and TEXTOR Contributors, 2006 *Plasma Phys. Control. Fusion* **48** A309

[37] Kerner W., Igitkhanov Yu, Janeschitz G. and Pogutse O., 1998 *Contrib. Plasma Phys.* **38** 118

[38] Loozen X., Tokar M.Z. and Wolf R., 2004 *Deutsche Physikalische Gesellschaft Frühjahrstagung*, Kiel, P 10.21

[39] Loozen X. *et al.*, 2006 *Deutsche Physikalische Gesellschaft Frühjahrstagung*, Augsburg, P 11.1

[40] Loozen X., Kalupin D., Tokar M.Z., Marchuk O. and Jakubowski M., 2006 *Contrib. Plasma Phys.* **46** 704

[41] Luciani J.F., Mora P. and Virmont J., 1983 *Phys. Rev. Lett.* **51** 1664

[42] Manheimer W.M. and Lashmore-Davies C.N., 1989 *MHD and Microinstabilities in Confined Plasmas* (The Adam Hilger Series on Plasma Physics, Institute of Publishing)

[43] Nilsson J. and Weiland J., 1994 *Nucl. Fusion* **34** 803

[44] Nycander J. and Yankov V.V., 1995 *Phys. Plasmas* **2** 2874

[45] Ohyabu N. and DeGrassie J.S., 1987 *Nucl. Fusion* **27** 2171

[46] Onjun T., Bateman G., Kritz A.H. and Hammett G., 2002 *Phys. Plasmas* **9** 5018

[47] Ott E., 1993 *Chaos in Dynamical Systems* (Cambridge Universtity Press)

[48] Payan J., Garbet X., Chatenet J.H. *et al.*, 1995 *Nucl. Fusion* **35** 1357

[49] Reiser D. and Scott B., 2005 *Phys. Plasmas* **12** 122308

[50] Rogister A.L., 2004 *Transactions of Fusion Science and Technology*, 6th Carolus Magnus Euro-Summer School on Plasma and Fusion Energy Physics, Brussels, ISSN:1536-1055, **45** 338

[51] Rechester A.B. and Rosenbluth M.N., 1978 *Phys. Rev. Lett.* **40** 38

[52] Sagdeev R.Z., Usikov D.A., Zaslavsky G.M., 1988 *Nonlinear Physics, From the Pendulum to Turbulence and Chaos* (Harwood Academic Publishers: Chur, Switzerland)

[53] Samain A., Capes H., Ghendrih Ph. and Nguyen F., 1993 *Phys. Fluids B* **5** 471

[54] Shafranov V.D., 1971 *Plasma Phys.* **13** 757

[55] Snipes J.A. *et al.*, 2002 *Proc. 19th IAEA Int. Conf. on Fusion Energy 2002 (Lyon, France)*, `http://www.iaea.org/programmes/ripc/physics/fec2002/html/fec2002.htm`

[56] Spitzer L. and Härm R., 1953 *Phys. Rev.* **89** 977

[57] Stangeby P.C., 2000 *The Plasma Boundary of Magnetic Fusion Devices* IoP Publishing

[58] Teller E., 1981 *Fusion* **1** (Academic Press)

[59] Tokar M.Z., 1994 *Plasma Phys. Control. Fusion* **36** 1819

[60] Tokar M.Z. *et al.*, 1997 *Plasma Phys. Control. Fusion* **39** 569

[61] Tokar M.Z., 1999 *Phys. Plasmas* **6** 2808

[62] Tokar M.Z., Kelly F.A. and Loozen X., 2005 *Phys. Plasmas* **12** 052510

[63] Unterberg B., 2005 *Magnetically confined fusion plasmas with a radiating boundary and improved energy confinement* (Forschungszentrum Jülich GmbH, Jül-4158) ISSN 0944-2952

[64] Ware A.A., 1970 *Phys. Rev. Lett.* **25** 916

[65] Weiland J., 2000 *Collective Modes in Inhomogeneous Plasmas* (Institute of Physics Publishing)

[66] Weisen H. *et al.*, 2004 *Plasma Phys. Control. Fusion* **46** 751

[67] Wesson J., 2005 *Tokamaks* (Oxford University Press)

[68] Xu Y., Weynants R., Jachmich S. *et al.*, 2006 *Private communication*

[69] Yushmanov P.N. *et al.*, 1990 *Nucl. Fusion* **30** 1999

[70] Zabolotsky A., Weisen H. and TCV Team, 2003 *Plasma Phys. Control. Fusion* **45** 735

[71] Zuoyang Chang and Callen J.D., 1992 *Phys. Fluids B* **4** 1766

Forschungszentrum Jülich
in der Helmholtz-Gemeinschaft

Jül-4251
Juni 2007
ISSN 0944-2952